iScience

CellPress
OPEN ACCESS

Article

Disturbed Presynaptic Ca^{2+} Signaling in Photoreceptors in the EAE Mouse Model of Multiple Sclerosis

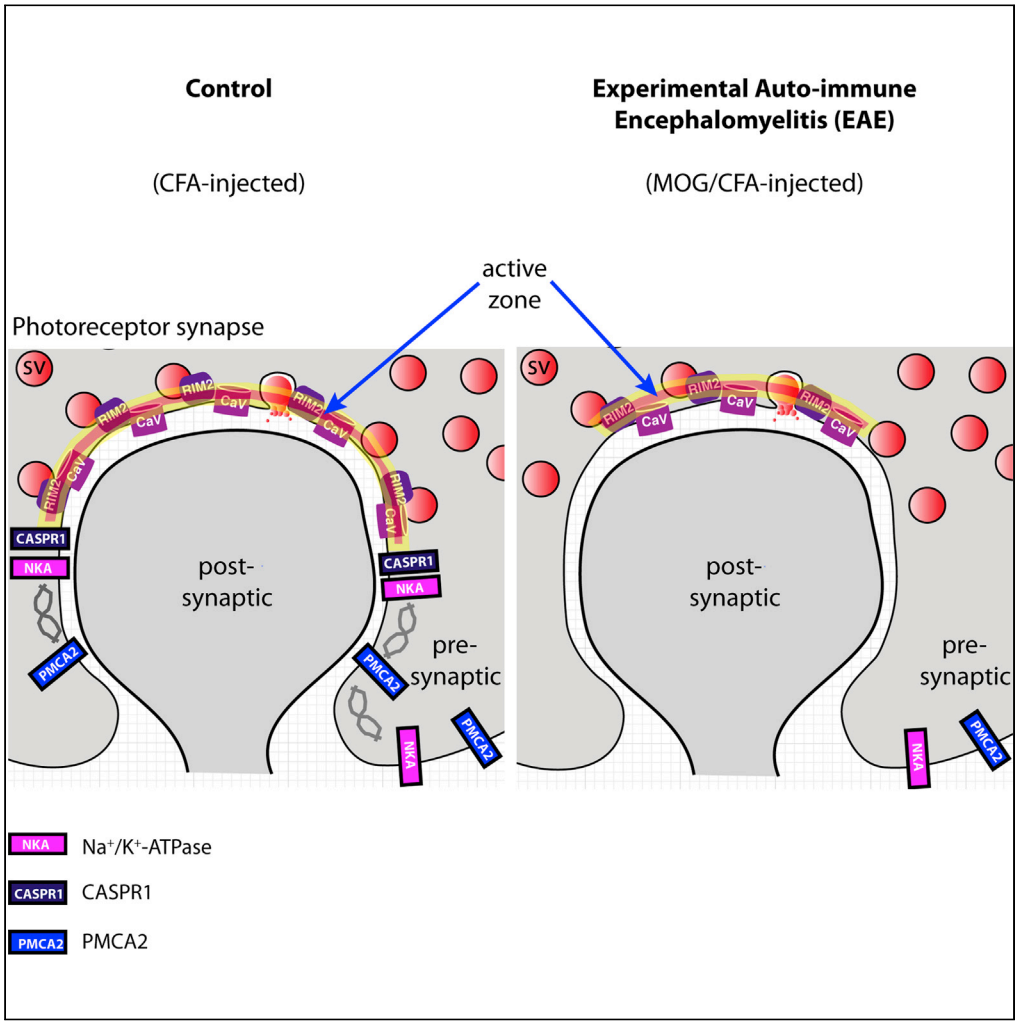

Amrita Mukherjee, Rashmi Katiyar, Ekta Dembla, ..., Veit Flockerzi, Karin Schwarz, Frank Schmitz

mukherjee.amrita85@gmail.com (A.M.)
frank.schmitz@uks.eu (F.S.)

HIGHLIGHTS

Less Cav-channels and RIM2 at the active zones of EAE photoreceptor synapses

Decreased depolarization-evoked Ca^{2+}-responses in EAE photoreceptor synapses

Elevated basal, resting Ca^{2+} levels in preclinical EAE photoreceptor terminals

Decreased expression of PMCA2 and Na^{+}/K^{+}-ATPase in EAE photoreceptor synapses

Mukherjee et al., iScience 23, 101830
December 18, 2020
https://doi.org/10.1016/j.isci.2020.101830

iScience

CellPress
OPEN ACCESS

Article

Disturbed Presynaptic Ca^{2+} Signaling in Photoreceptors in the EAE Mouse Model of Multiple Sclerosis

Amrita Mukherjee,[1,*] Rashmi Katiyar,[1] Ekta Dembla,[1] Mayur Dembla,[1,4] Praveen Kumar,[1,5] Anouar Belkacemi,[2] Martin Jung,[3] Andreas Beck,[2] Veit Flockerzi,[2] Karin Schwarz,[1] and Frank Schmitz[1,6,*]

SUMMARY

Multiple sclerosis (MS) is a demyelinating disease caused by an auto-reactive immune system. Recent studies also demonstrated synapse dysfunctions in MS patients and MS mouse models. We previously observed decreased synaptic vesicle exocytosis in photoreceptor synapses in the EAE mouse model of MS at an early, preclinical stage. In the present study, we analyzed whether synaptic defects are associated with altered presynaptic Ca^{2+} signaling. Using high-resolution immunolabeling, we found a reduced signal intensity of Cav-channels and RIM2 at active zones in early, preclinical EAE. In line with these morphological alterations, depolarization-evoked increases of presynaptic Ca^{2+} were significantly smaller. In contrast, basal presynaptic Ca^{2+} was elevated. We observed a decreased expression of Na^{+}/K^{+}-ATPase and plasma membrane Ca^{2+} ATPase 2 (PMCA2), but not PMCA1, in photoreceptor terminals of EAE mice that could contribute to elevated basal Ca^{2+}. Thus, complex Ca^{2+} signaling alterations contribute to synaptic dysfunctions in photoreceptors in early EAE.

INTRODUCTION

Multiple sclerosis (MS) is a severe and frequent demyelinating disease of the central nervous system characterized by inflammation, demyelination, and axonal degeneration in the white matter (Lassmann et al., 2007; Dendrou et al., 2015; Faissner et al., 2019). Optic neuritis is a frequent and early event in MS. The pathogenesis of MS is not completely understood. Recent studies both in MS patients (Loewe et al., 2014; Haider et al., 2014; Jürgens et al., 2016) and mouse models of MS (Habbas et al., 2015; Stampanoni Bassi et al., 2017; Rizzo et al., 2018) revealed that not only the white matter but also the gray matter is affected by the disease. In the gray matter, neurodegeneration, neuronal cell death, and synapse dysfunctions were found (Mandolesi et al., 2015; Stampanoni-Bassi et al., 2017; Schattling et al., 2019). Interestingly, gray matter alterations occur early in the disease before obvious changes in the white matter, arguing against the possibility that these changes happen as a consequence of demyelination. Recently, Dembla et al. (2018) observed synaptic dysfunctions in the retina of the experimental auto-immune encephalomyelitis (EAE) mouse model of MS. The EAE mouse model is a prevalent, frequently used and well-validated model of MS ("gold-standard animal model for MS"; Constantinescu et al., 2011; Robinson et al., 2014; Ben-Nun et al., 2014). In the retina, photoreceptor synapses, an unmyelinated tissue, were particularly strongly affected in early, pre-clinical EAE. These synapses showed morphological and functional alterations, including decreased synaptic vesicle exocytosis and impaired visually guided behavior without gross morphological alterations in the optic nerve at the light and electron microscopic level (Dembla et al., 2018).

Photoreceptor synapses are continuously active ribbon synapses (Matthews and Fuchs, 2010; Lagnado and Schmitz, 2015; Moser et al., 2020). In photoreceptor synapses, synaptic vesicle fusion occurs predominantly at the active zones where L-type voltage-gated Ca^{2+} (Cav)-channels and RIM proteins, which control Cav-channel function, are enriched. To maintain continuous transmission over long periods of time, the active zones are associated with large presynaptic specializations, the synaptic ribbons that tether additional vesicles (Moser et al., 2020). The RIBEYE protein is the central building block of synaptic ribbons (Schmitz et al., 2000; Maxeiner et al., 2016). At their basal, membrane-proximal end, the ribbons are anchored to the active zones. At the photoreceptor active zone, the L-type Ca^{2+}-channels, consisting of the Cav1.4 pore-forming α1-subunit and the auxiliary β2-and $\alpha 2\delta 4$ subunits, show little voltage- and Ca^{2+}-dependent inactivation (Wahl-Schott et al., 2006; Joiner and Lee, 2015; Pangrsic et al., 2018), thus promoting continuous synaptic

[1]Institute of Anatomy and Cell Biology, Department of Neuroanatomy, Saarland University, Medical School, 66421 Homburg, Germany

[2]Institute of Experimental and Clinical Pharmacology and Toxicology, Saarland University, Medical School, 66421 Homburg, Germany

[3]Institute of Medical Biochemistry and Molecular Biology, Saarland University, Medical School, 66421 Homburg, Germany

[4]Present: Duke University Eye Center, Durham, NC 27710, USA

[5]Present: Institute of Anatomy and Cell Biology, Department Krasteva-Christ, Saarland University, Medical School, 66421 Homburg, Germany

[6]Lead Contact

*Correspondence: mukherjee.amrita85@gmail.com (A.M.), frank.schmitz@uks.eu (F.S.)

https://doi.org/10.1016/j.isci.2020.101830

vesicle exocytosis. RIM2 is the major long RIM variant in rod photoreceptor synapses (Grabner et al., 2015; Löhner et al., 2017). CASPR1, an adhesion protein and a frequent auto-immune target (Stathopoulos et al., 2015), is also present at the synaptic ribbon complex (Dembla et al., 2018). The photoreceptor ribbon synapses were affected early on in the preclinical phase of EAE (Dembla et al., 2018). These early synaptic changes in EAE retinas are associated with a rapid and massive auto-immune response directed against retinal proteins, including auto-antibodies against CASPR1, that lead to an enhanced recruitment and activation of a local complement system at retinal synapses. This occurs in parallel with impaired synaptic vesicle exocytosis at photoreceptor synapses, altered synaptic ribbons, and altered visual behavior before the onset of optic nerve demyelination (Dembla et al., 2018).

In the present study, we analyzed molecular mechanisms that might be underlying the early synaptic alterations in photoreceptor synapses of EAE mice. We focused on presynaptic Ca^{2+} signaling because of its central role in synaptic transmission (Südhof, 2012b, 2014). Furthermore, some drugs used in MS therapy target Ca^{2+}-dependent pathway and Ca^{2+}-homeostasis (Schampel et al., 2017; Ingwersen et al., 2018; Hundehege et al., 2018; Criscuolo et al., 2019; Faissner et al., 2019), emphasizing an important role of Ca^{2+} in MS. Therefore, we analyzed whether key components of presynaptic Ca^{2+} signaling at the active zone of photoreceptor synapses might be morphologically altered in early preclinical EAE. Intracellular Ca^{2+} changes were measured to determine basal synaptic Ca^{2+} levels under resting conditions and depolarization-evoked Ca^{2+} responses during stimulation. Using these approaches we found morphological and functional evidence for altered Ca^{2+} signaling at photoreceptor synapses in early EAE.

RESULTS

In the present study, we tested for possible alterations of Ca^{2+} homeostasis in the EAE mouse model of MS. In this prevalent, well-validated model (for review, see Constantinescu et al., 2011; Robinson et al., 2014; Ben-Nun et al., 2014), MS-like symptoms are induced by injection of encephalitogenic MOG_{35-55} peptide from myelin oligodendrocyte glycoprotein (MOG) emulsified with complete Freund's adjuvant (CFA) (and additional pertussis toxin (PTX) injection) (see also Transparent Methods). This MOG_{35-55}-EAE C57BL/6 model is considered as a "gold-standard" animal model for MS (Ben-Nun et al., 2014).

Cav1.4 Is less Enriched at the Active Zone of Photoreceptor Synapses in EAE Mice

We first analyzed the distribution of voltage-gated Ca^{2+} (Cav) channels in rod photoreceptor synapses of MOG/CFA-injected mice in comparison to CFA-injected control mice (Figures 1, S1, and S2). Rod photoreceptor synapses are located in the outer plexiform layer (OPL) of the retina and can be clearly identified by the presence of a single large horseshoe-shaped synaptic ribbon (Schmitz et al., 2000; Moser et al., 2020). For immunolabeling of Cav-channels, we made use of three different, knockout-verified antibodies against Cav1.4 (Dembla et al., 2020) (Figures 1, S1, and S2). The morphological analyses were performed on retina sections obtained from mice 9 days after injection with MOG/CFA (experimental condition) or CFA alone (control condition). At this time point, the optic nerve appears morphologically unaffected and does not show obvious demyelination and signs of optic neuritis (Fairless et al., 2012; Dembla et al., 2018). This early preclinical time window was chosen to exclude changes in the retina that are secondary to demyelination and axon loss in the optic nerve.

The typical horseshoe-shaped pattern of immunolabeled synaptic ribbons and Cav1.4-labeled active zones were readily evident in the OPL of CFA-injected control retinas, as demonstrated by double-immunolabeling with Cav1.4- and RIBEYE antibodies (Figures 1, S1, and S2). Confocal microscopy of control retinas demonstrated that both proteins co-localized at the active zone of photoreceptor synapses (Figures 1A–1C, S1A–S1C, and S2A–S2C). All three Cav1.4 antibodies demonstrated that Cav1.4 was still present at the photoreceptor active zone of MOG/CFA-injected EAE mice (Figures 1D–1F, S1D–S1F, and S2D–S2F). But quantitative analyses of the intensity of Cav1.4 immunosignals revealed that the intensity was significantly reduced in photoreceptor active zones of MOG/CFA-injected EAE mice in comparison to CFA-injected control mice (Figures 1G, 1H, S1G, S1H, S2G, and S2H). This reduction in Cav1.4 immunolabeling intensity was consistently observed with all three different Cav1.4 antibodies (Figures 1, S1, and S2). Remarkably, the number of Cav1.4 puncta in the OPL was unchanged between CFA-injected control mice and MOG/CFA-injected EAE mice (Figures 1I, 1J, S1I, S1J, S2I, and S2J). This indicates that the number of photoreceptor synapses and active zones is identical in CFA control and MOG/CFA-injected mice 9 days after injection. These results were consistently observed with the three different Cav1.4 antibodies, Cav1.4 Cterm (Figure 1), Cav1.4 Nterm (Figure S1), and Cav1.4 [16D9] (Figure S2), raised against different regions

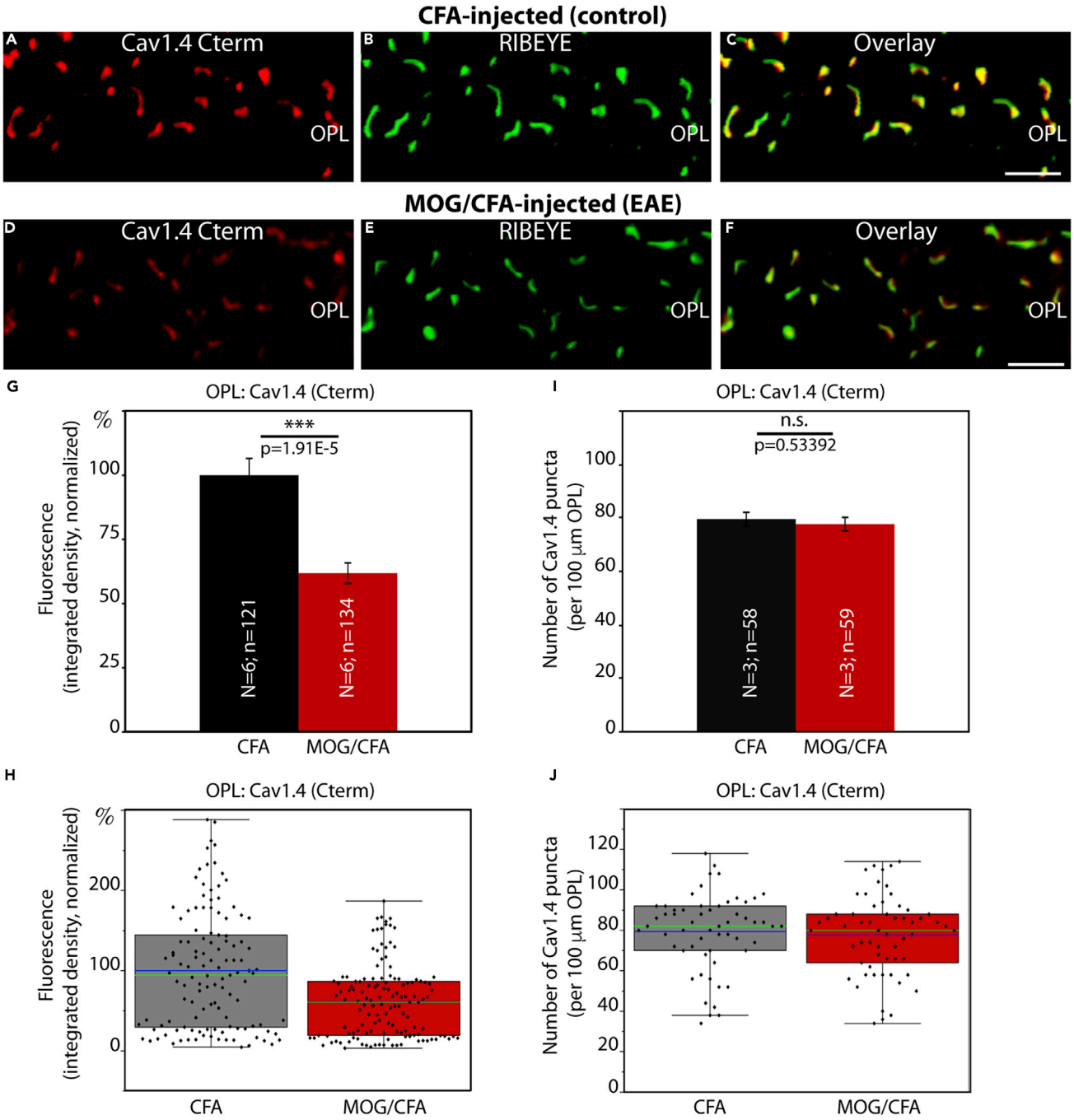

Figure 1. Cav1.4 Is Less Enriched at the Active Zone of Photoreceptor Synapses in EAE Mice

(A–F) Retina sections (0.5 µm in thickness) from CFA- and MOG/CFA-injected mice processed 9 days after injection. Confocal analyses of rod photoreceptor synapses in the OPL immunolabeled with rabbit polyclonal antibody against Cav1.4 (Cav1.4 Cterm) and mouse monoclonal antibody (2D9) against RIBEYE. The intensity of the Cav1.4 immunosignals is quantified as integrated density in (G and H). The number of Cav1.4 puncta is quantified in (I and J). Values are means ± S.E.M. (G and I). In the box-and-whiskers plots of the data in (H and J) mean values are labeled by blue horizontal bars and median values by green horizontal bars. Boxes represent 25th–75th percentiles of values, and whiskers are equal to 1.5 times of the interquartile range (IQR). Statistical significance was determined with Mann-Whitney U-test. Abbreviations: OPL, outer plexiform layer; S.E.M., standard error of the mean; N = number of mice; n = number of images analyzed from retinal sections. Scale bars: 2 µm.

of Cav1.4. Retinal sections were co-stained with anti-RIBEYE in these experiments to label synaptic ribbon as a reference (Figures 1B, 1E, S1B, S1E, S2B, and S2E). The fluorescence intensity of photoreceptor synaptic ribbons is also reduced in MOG/CFA-injected animals in comparison to CFA-injected control mice (Dembla et al., 2018).

Cav1.4 [16D9] and Cav1.4 Cterm have been previously verified on Cav1.4 knockout tissue (Dembla et al., 2020). The specificity of Cav1.4 Nterm for Cav1.4 is demonstrated in Figure S1K–S1P. The Cav1.4 Nterm generated a strong signal in the OPL of control retina (Figures S1K–S1P), similar to previously published data (Dembla et al., 2020). This Cav1.4 signal in the OPL was completely absent in the Cav1.4 knockout retina (Figure S1N), demonstrating the specificity of the antibody for Cav1.4. Retinal sections were also co-stained with anti-RIBEYE (Figures S1L and S1O). Synaptic ribbons in the OPL are altered in size and distribution in Cav1.4 knockout tissue, as was previously described (for review, see Joiner and Lee, 2015; Pangrsic et al., 2018). All Cav1.4 immunosignals were contained within the PSD95-immunolabeled photoreceptor presynaptic terminals (Figure S3). We did not observe any Cav1.4 immunosignal outside of the photoreceptor terminals (Figures S3N and S3P), similar to as previously described (Dembla et al., 2020).

The Length of Cav1.4 Protein Clusters at the Active Zone of Photoreceptor Synapses Is Decreased in EAE Mice

To better understand the underlying mechanism of the reduced Cav1.4 immunosignal strength in rod photoreceptor synapses of MOG/CFA-injected EAE mice in comparison to littermate control mice, we performed super-resolution structured-illumination-microscopy (SR-SIM) to analyze the size of the Cav1.4-immunolabeled active zone in greater detail. SR-SIM experiments demonstrated that the mean contour length of the Cav1.4 immunosignals in rod photoreceptor synapses of MOG/CFA-injected EAE mice was considerably shorter than in CFA-injected littermate control mice (Figure 2). Thus, the shorter contour length of the Cav1.4 immunosignals appears to be the main reason behind the observed reduced intensity of Cav1.4 immunosignals at rod photoreceptor synapses in EAE mice.

The Auxiliary β2-Subunit of Cav-Channels Is Also less Enriched at the Active Zone of Photoreceptor Synapses in EAE Mice

To further corroborate these findings, we also tested for the distribution of the auxiliary β2-subunit of the Cav-channels in rod photoreceptor synapses. For this purpose, we used two different, previously characterized antibodies against Cavβ2 (Meissner et al., 2011; Katiyar et al., 2015). Both Cavβ2 antibodies produced similar immunolabeling results (Figures 3A–3C, 3D–3F, S4A–S4C, and S4D–S4F), showing reduced Cavβ2 immunosignal strength in the OPL of MOG/CFA-injected mice in comparison to CFA-injected control mice (Figures 3G, 3H, S4G, and S4H). This reduction in the Cavβ2 immunosignal intensity was similar to the observed decreased intensity of the Cav1.4 α-subunit (Figures 1, S1, and S2). Again, similar to Cav1.4, the number of immunoreactive Cavβ2 puncta in the OPL remained unchanged (Figures 3I, 3J, S4I, and S4J). We also performed SR-SIM analyses with Cavβ2-immunolabeled retinas and found, similar to what we had previously observed for Cav1.4, a reduction in the contour length of the Cavβ2 immunosignals at rod photoreceptor synapses in the OPL of MOG/CFA-injected mice with respect to CFA-injected control littermate mice (Figure 4).

Validation of RIM2 Antibodies

Next we checked for RIM proteins. RIM proteins are essential components of the active zone and important for controlling central aspects of Cav-channel function (Kaeser et al., 2011, Han et al., 2011; Deng et al., 2011; Eggermann et al., 2011; Südhof, 2012a, 2012b; Hallermann and Silver, 2013; Kim et al., 2013; Nanou and Catterall, 2018). At rod photoreceptor synapses RIM2 is the major long RIM isoform (Grabner et al., 2015; Löhner et al., 2017). Based on its central function for Ca^{2+} homeostasis, we analyzed the distribution of RIM2 in rod photoreceptor synapses using a mouse monoclonal antibody against RIM2, clone 4C6.

The specificity of the 4C6 monoclonal RIM antibody was verified on photoreceptor-specific RIM1/2 double knockout retina in comparison to control retinas (Figure S5). The RIM2 monoclonal antibody 4C6 generated a strong immunosignal in the OPL of wild-type retinas (Figures S5A–S5C) but not in the OPL of the photoreceptor-specific RIM1/2 double-knockout (DKO) retina (Figures S5D–S5F). In the OPL of photoreceptor-specific RIM1/2 DKO retinas, the RIM2 immunosignals were completely abolished, (Figure S5D) whereas RIBEYE immunosignals (Figure S5E) were qualitatively unaffected. These experiments show that the 4C6 monoclonal antibody specifically detects RIM2 in the murine retina. The specificity of the RIM2 monoclonal

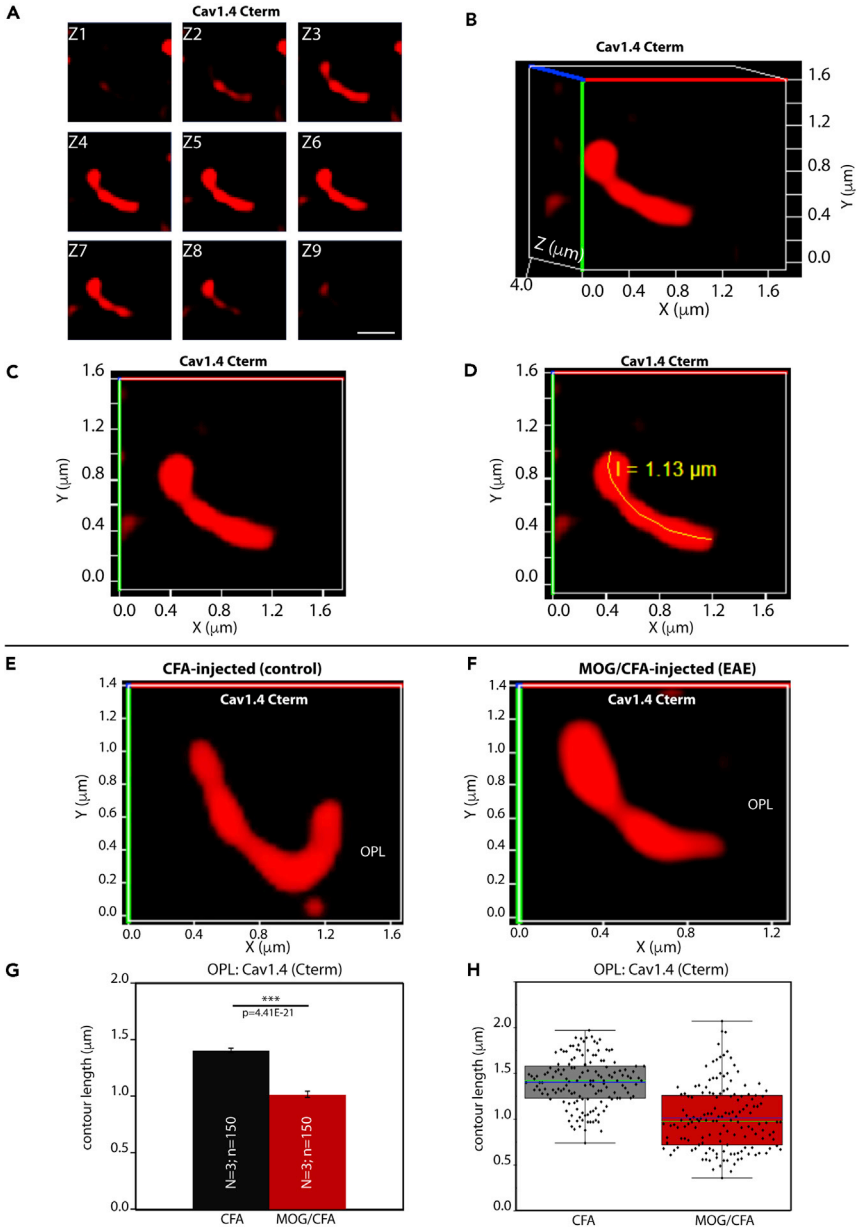

Figure 2. The Length of Cav1.4 Protein Clusters at the Active Zone Of Photoreceptor Synapses Is Decreased in EAE Mice

3D SR-SIM analyses of individual active zones of rod photoreceptor synapses from CFA-injected control mice and MOG/CFA-injected experimental mice immunolabeled with polyclonal antibody against Cav1.4 Cterm.

(A–D) demonstrate how contour length of individual active zones was determined by 3D SR-SIM. (A) Individual z stack obtained with 3D SR-SIM; (B) the spatial 3D view; (C) the 2D projection of the 3D view with the active zone being rotated parallel to the X, Y-plane; (D) the measurement of the contour length of the presented active zone.

(E and F) Exemplary SR-SIM images from CFA-injected control mice (E) and MOG/CFA-injected EAE mice (F).

(G and H) Quantitative analyses of the active zone contour length (mean ± S.E.M.) (G) obtained from SR-SIM measurements. In the box-and-whiskers plots in (H), mean values are indicated by blue horizontal bars and median values by green horizontal bars. Boxes represent 25th–75th percentiles of values and whiskers are equal to 1.5 times of the IQR. Statistical significance was determined with Mann-Whitney U-test. Abbreviations: S.E.M., standard error of the mean; N = number of mice; n = number of analyzed immunolabelled active zones; OPL, outer plexiform layer. Scale bar: 0.5µm (A).

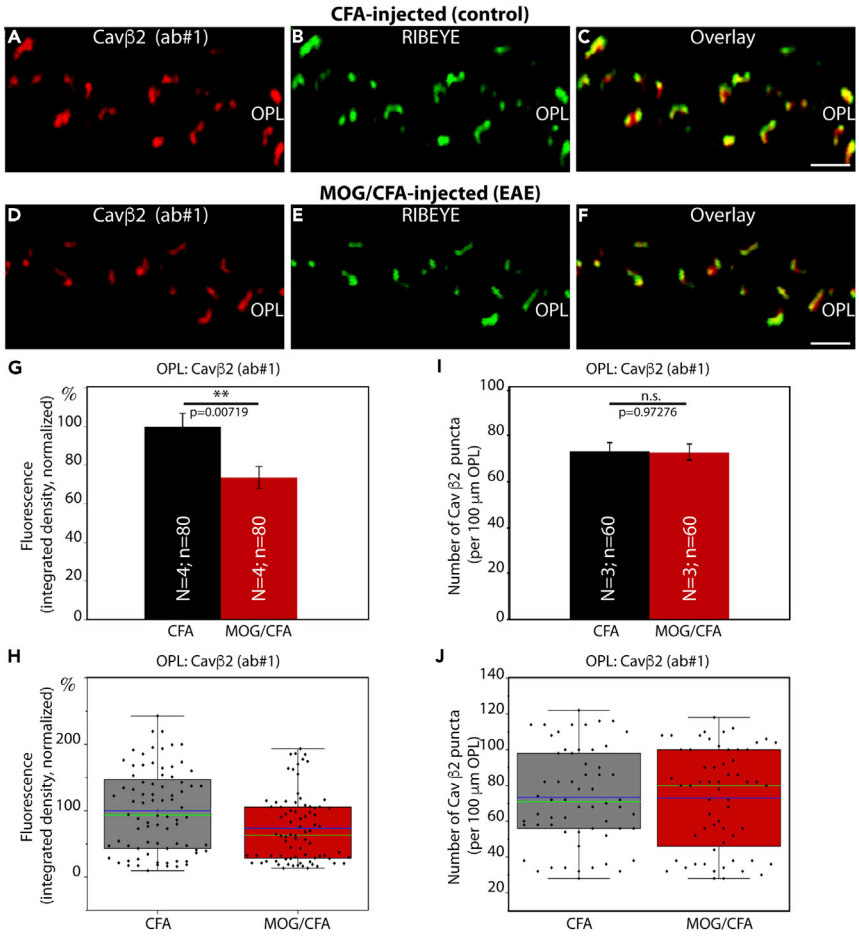

Figure 3. The Auxiliary β2-Subunit of Cav Channels Is Also Less Enriched at the Active Zone of Photoreceptor Synapses in EAE Mice

(A–F) Retina sections (0.5 µm in thickness) from CFA- and MOG/CFA-injected mice processed 9 days after injection. Confocal analyses of rod photoreceptor synapses in the OPL immunolabeled with rabbit polyclonal antibody against Cavβ2 (ab#1) and mouse monoclonal antibody (2D9) against RIBEYE. The intensity of the Cavβ2 immunosignals is quantified as integrated density in (G and H). The number of Cavβ2 puncta is quantified in (I and J). Values are means ± S.E.M. (G and I). In the box-and-whiskers plots of the data in (H and J) mean values are labeled by blue horizontal bars and median values by green horizontal bars. Boxes represent 25th–75th percentiles of values and whiskers are equal to 1.5 times of the IQR. Statistical significance was determined with Mann-Whitney U-test. Abbreviations: OPL, outer plexiform layer; S.E.M., standard error of the mean; N = number of mice; n = number of images analyzed from retinal sections. Scale bars: 2 µm.

antibody 4C6 for the RIM2 peptide was also verified by pre-absorption experiments. The 4C6 monoclonal antibody was pre-absorbed either with the RIM2 peptide against which the antibody was raised (Figure S5J) or with an unrelated control peptide (Figure S5G). Pre-absorption with the RIM2 peptide completely abolished binding of the 4C6 RIM2 antibody to its target in the OPL (Figure S5J), whereas blocking with unrelated peptide had no effect (Figure S5G). Blocking with either peptide had no influence on RIBEYE labeling (Figures S5H, S5I, S5K, and S5L).

RIM2 Is Less Enriched at the Active Zones of Photoreceptor Synapses in EAE Mice

The immunolabeling results obtained with the monoclonal RIM2 antibody 4C6 demonstrated that the RIM2 immunosignals were severely reduced in the active zone of photoreceptor synapses from MOG/CFA-injected mice (Figure 5D) in comparison to CFA-injected control mice (Figure 5A) (for quantification of immunosignal strengths, see Figures 5G and 5H). Similar to Cav1.4 and Cavβ2, the number of immunoreactive RIM2 puncta in the OPL of MOG/CFA-injected mice were unchanged in comparison to CFA-injected

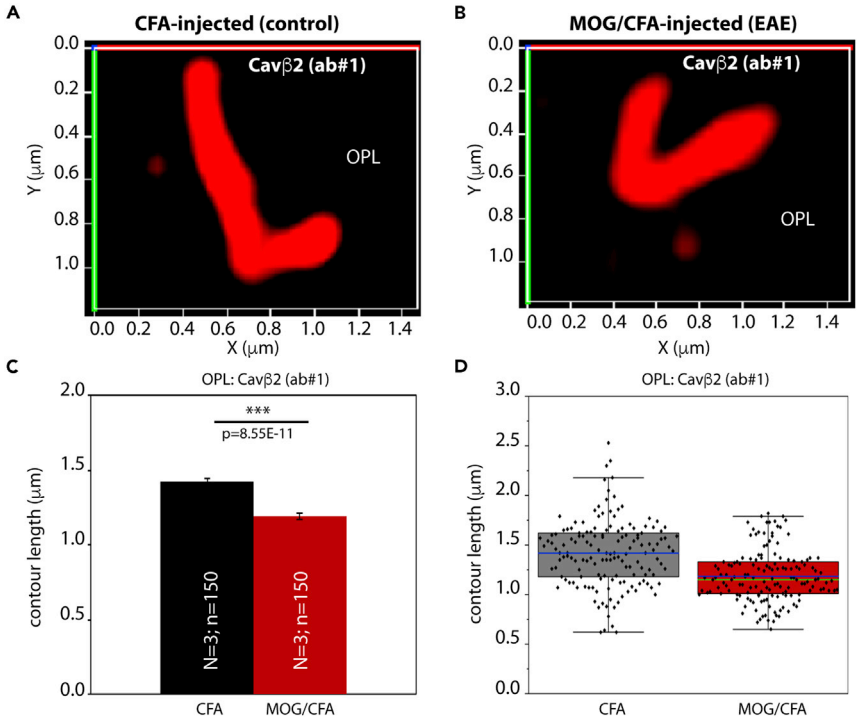

Figure 4. The Length of Auxiliary Cav Channel β2-Subunit Protein Clusters at the Active Zone of Photoreceptor Synapses Is Decreased in EAE Mice

3D SR-SIM analyses of individual active zones of rod photoreceptor synapses from CFA-injected control mice and MOG-CFA-injected experimental mice immunolabeled with polyclonal antibody against Cavβ2 (ab #1), (A–D) Exemplary SR-SIM images from CFA-injected control mice (A) and MOG/CFA-injected EAE mice (B).

(C and D) quantitative analyses of the active zone contour length (mean ± S.E.M.) (C) obtained from SR-SIM measurements. In the box-and-whiskers plots of the data in (D), mean values are indicated by blue horizontal bars and median values by green horizontal bars. Boxes represent 25th–75th percentiles of values and whiskers are equal to 1.5 times of the IQR. Statistical significance was determined with Mann-Whitney U-test. Abbreviations: S.E.M., standard error of the mean; N = number of mice; n = number of analyzed immunolabeled active zones; OPL, outer plexiform layer.

littermate control mice (Figures 5I and 5J). Very similar immunolabeling and quantification results were obtained with another RIM2 monoclonal antibody (4F7 RIM2 monoclonal antibody; Figure S6). Fluorescence intensity measurements with the 4F7 RIM2 antibody were performed on CFA and MOG/CFA sections double-immunolabeled with PSD95 (Figures S6A–S6H). Counting of RIM2 puncta with the 4F7 RIM2 antibody was done on sections double-immunolabeled with anti-RIBEYE antibody (for better reference to the active zone [figure not shown]; for quantification see Figures S6I and S6J). We did not perform SR-SIM analyses with the 4C6 or 4F7 monoclonal RIM2 antibodies because the RIM2 immunosignals were too weak in the OPL of MOG/CFA-injected samples and thus difficult to discriminate from background signals after processing for SR-SIM.

Thus, in conclusion two central components of the active zones (Cav1.4 channels and RIM2 proteins) were consistently less enriched at the active zone of rod photoreceptor synapses of MOG/CFA-injected EAE mice, whereas the number of active zones remained unchanged. This decreased protein enrichment in EAE photoreceptor synapses appeared to be selective for active zone proteins because other proteins of the presynaptic rod photoreceptor terminal, e.g. PSD-95, PMCA1 (the most abundant PMCA protein in the murine retina), were not altered in signal strength in EAE photoreceptor synapses (Figures 8H, 8K, 8M, 8N, 9D, 9G, 9H, S9D, S9G, and S9H) if compared against photoreceptor synapses of CFA-injected control mice (Figures 8B, 8E, 8M, 8N, 9A, 9G, 9H, S9A, S9G, and S9H).

Fura2 Ca^{2+} Imaging of Photoreceptor Synapses in the Outer Plexiform Layer of the Retina

Next, we asked whether the observed morphological changes of active zone proteins also lead to functional alterations. For this purpose, we performed Fura2 Ca^{2+} imaging and monitored high

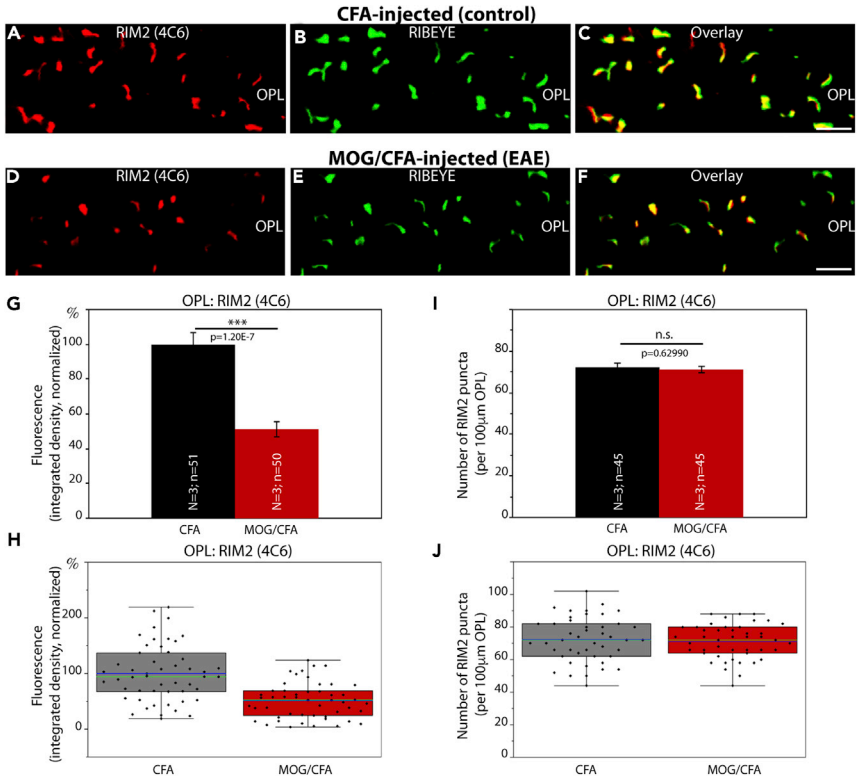

Figure 5. RIM2 Is Less Enriched at the Active Zones of Photoreceptor Synapses in EAE Mice

(A–F) Retinal sections (0.5 µm in thickness) from CFA- and MOG/CFA-injected mice processed 9 days after injection. Confocal analyses of rod photoreceptor synapses in the OPL immunolabeled with mouse monoclonal antibody against RIM2 (4C6) and rabbit polyclonal antibody against RIBEYE (U2656, Schmitz et al., 2000). The intensity of the RIM2 immunosignals were quantified as integrated density in (G and H). The number of RIM2 puncta are quantified in (I and J). Values are means ± S.E.M. (G and I). In the box-and-whiskers plots of the data in (H and J), mean values are indicated by blue horizontal bars and median values by green horizontal bars. Boxes represent 25th–75th percentiles of values and whiskers are equal to 1.5 times of the IQR. Statistical significance was determined with two-sample unpaired Student's t test. Abbreviations: OPL, outer plexiform layer; S.E.M., standard error of the mean; N = number of mice; n = number of images analyzed from the retinal sections. Scale bars: 2 µm.

K^+-depolarization-induced Ca^{2+} entry in the OPL of retinal slices of mice that were injected with either MOG/CFA (EAE experimental group) or with CFA (control group). Fura2 recordings were performed at 7 days (Figure 6A), 8 days (Figures 6B), and 9 days (Figure 6C) after injection. Regions of interest (ROIs) for analyses were placed at the OPL between the ONL and INL, as identified by phase contrast microscopy, F380 epifluorescence, and F340/F380 fluorescence signals. To further confirm proper localization of the ROIs, we also analyzed RIBEYE-FP-transgenic mice in which synaptic ribbons are fluorescently labeled (Okawa et al., 2019). These controls confirmed that the ROIs were properly placed and further suggested that the strongest K^+-depolarization-evoked responses were observed at the presynaptic photoreceptor terminals in the OPL (Figure S7), in agreement with previous findings (for review, see Van Hook et al., 2019).

Decreased High K^+-Depolarization-Evoked Ca^{2+} Responses and Elevated Basal, Resting Ca^{2+} Levels in Photoreceptor Synapses of EAE Mice

With Fura2 Ca^{2+} imaging, we observed severe alterations in presynaptic Ca^{2+} in photoreceptor synapses of MOG/CFA-injected mice in comparison to CFA-injected control mice (Figures 6 and 7). The Ca^{2+} baseline levels were consistently higher (more than ≈100nM) in photoreceptor synapses of EAE mice in comparison to control synapses from CFA-injected mice (Figures 6A–6C; quantification in 6D, and 6E). In contrast, the high K^+-depolarization-induced increases of presynaptic Ca^{2+} concentration were smaller in MOG/CFA-injected mice in comparison to CFA-injected control mice (Figures 6A–6C and 7). In order to better analyze the evoked Ca^{2+} responses independent of the different resting values, we normalized the evoked

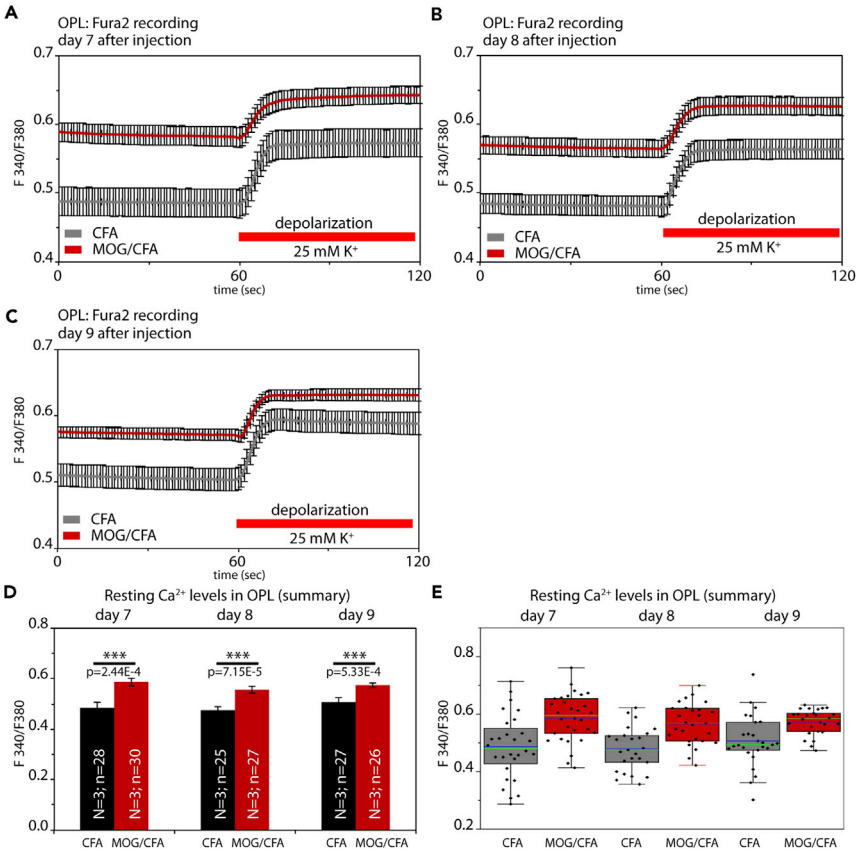

Figure 6. Altered presynaptic Ca^{2+} signaling at photoreceptor synapses in EAE mice

(A–C) Mean Fura2 ratiometric Ca^{2+} signals (±S.E.M.) measured in the OPL of CFA-injected control mice and MOG/CFA-injected EAE mice. Intracellular Ca^{2+} signals were measured at the indicated days after injection (day 7, day 8, or day 9 after injection). After 1min incubation in RS to obtain stable baseline signals, slices were depolarized by the addition of a K^+-rich depolarization solution, as indicated by the red bar. Mean calibrated Ca^{2+} concentration before and after addition of high potassium are indicated for each analyzed day after injection. In (D), the mean baseline Fura2 responses were plotted from MOG/CFA-injected EAE mice and CFA-injected control mice. Values are shown as means ± S.E.M. (D). In (E), the data summarized in (D) were plotted as box-and-whiskers plots to show their individual distribution. Mean values are indicated by blue horizontal bars and median values by green horizontal bars (E). Boxes represent 25^{th}–75^{th} percentiles of values and whiskers are equal to 1.5 times of the IQR. Statistical significance was determined with two-sample unpaired Student's t test (data of day 7, day 8) and with Mann-Whitney U-test (data of day 9). Using the calibration described in Materials and Methods, the following Ca^{2+} concentrations were determined for Fura2 baseline values at resting conditions on day 7: 173 nM Ca^{2+} (for CFA), 319 nM Ca^{2+} (for MOG/CFA); on day 8: 169 nM Ca^{2+} (for CFA), 284 nM Ca^{2+} (for MOG/CFA); and on day 9: 198 nM Ca^{2+} (for CFA), 295 nM Ca^{2+} (for MOG/CFA). For the high K^+-depolarization-evoked responses, the following Ca^{2+} concentrations were determined for day 7: 300 nM Ca^{2+} (for CFA), 439 nM Ca^{2+} (for MOG/CFA); on day 8: 283 nM Ca^{2+} (for CFA), 381 nM Ca^{2+} (for MOG/CFA); and on day 9: 316 nM Ca^{2+} (for CFA), 386 nM Ca^{2+} (for MOG/CFA). Abbreviations: OPL, outer plexiform layer; S.E.M., standard error of the mean; N = number of mice; n = number of retinal slices.

responses to identical baseline levels (Figures 7A–7F). Normalization to identical starting baseline levels clearly revealed the decrease in high K^+-evoked Ca^{2+} responses in the MOG/CFA-injected animals in comparison to the littermate controls. K^+-depolarization-induced responses were reduced on all days analyzed, as early as on day 7 after injection (Figures 7A and 7B). The high K^+-depolarization-evoked Ca^{2+} responses could be best fitted by a single exponential curve (Figures 7B, 7D, and 7F). From the respective mono-exponential curve fits we extracted the response amplitudes (Figures 7G and 7H). In all cases, the amplitudes of depolarization-evoked responses were significantly smaller in EAE mice (Figures 7G and 7H). The decreased evoked responses are most likely caused by the alterations of the active zone described above. The high K^+-depolarization-evoked Ca^{2+} responses in the OPL were due to Ca^{2+} influx

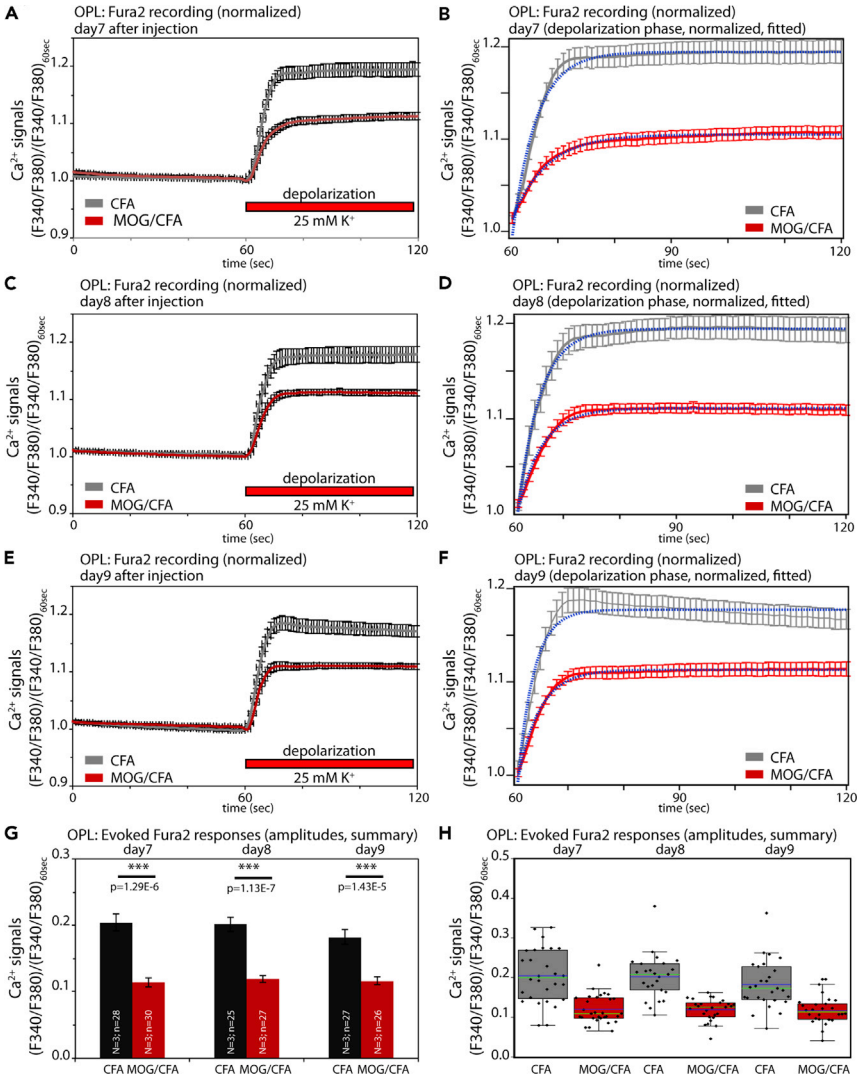

Figure 7. Decreased High K^+-Depolarization-Evoked Ca^{2+} Responses in Photoreceptor Synapses of EAE Mice

Analyses of depolarization-evoked Fura2 ratiometric Ca^{2+} signals at photoreceptor synapses of MOG/CFA-injected EAE mice and CFA-injected control mice at the indicated days after injection (day 7, day 8, and day 9 after injection). Curves shown in (A, C, E) represent the Fura2 F340/F380 ratiometric signals (from Figure 6), normalized to the resting Fura2 signals before high potassium application for better display of the Fura2 signals that result from depolarization-evoked increase of presynaptic Ca^{2+}. In (B, D, F), only the normalized signals after high potassium application are depicted together with the respective curve fits. Statistical analyses of the normalized, high potassium-induced depolarization Fura2 signals are shown in (G, H). Values are shown as means ± S.E.M. (A–G). In the box-and-whiskers plot of the individual data points in (H), mean values are indicated by blue horizontal bars and median values by green horizontal bars. Boxes represent 25^{th}–75^{th} percentiles of values and whiskers are equal to 1.5 times of the IQR. Statistical significance was determined with Mann-Whitney U-test (data of day 7) and with two-sample unpaired Student's t test (data of day 8, day 9). Abbreviations: OPL, outer plexiform layer; S.E.M., standard error of the mean; N = number of mice; n = number of retinal slices.

through voltage-gated Ca^{2+} (Cav) channels as shown by control experiments with Co^{2+} (Figures S7J and S7K).

As shown in Figure 6, presynaptic basal Ca^{2+} in MOG/CFA-injected EAE mice under resting conditions was higher in comparison to control mice. It is well known that cytoplasmic Ca^{2+} is increased by inhibition of the Na^+/K^+-ATPase (Schatzmann, 1953; Repke and Portius, 1963; Repke, 1964; Skou, 1998; Ravens and Himmel, 1999; Katz and Lorell, 2000; Aizman et al., 2001; Kaplan, 2002; Wasserstrom and Aistrup, 2005; Bay et al.,

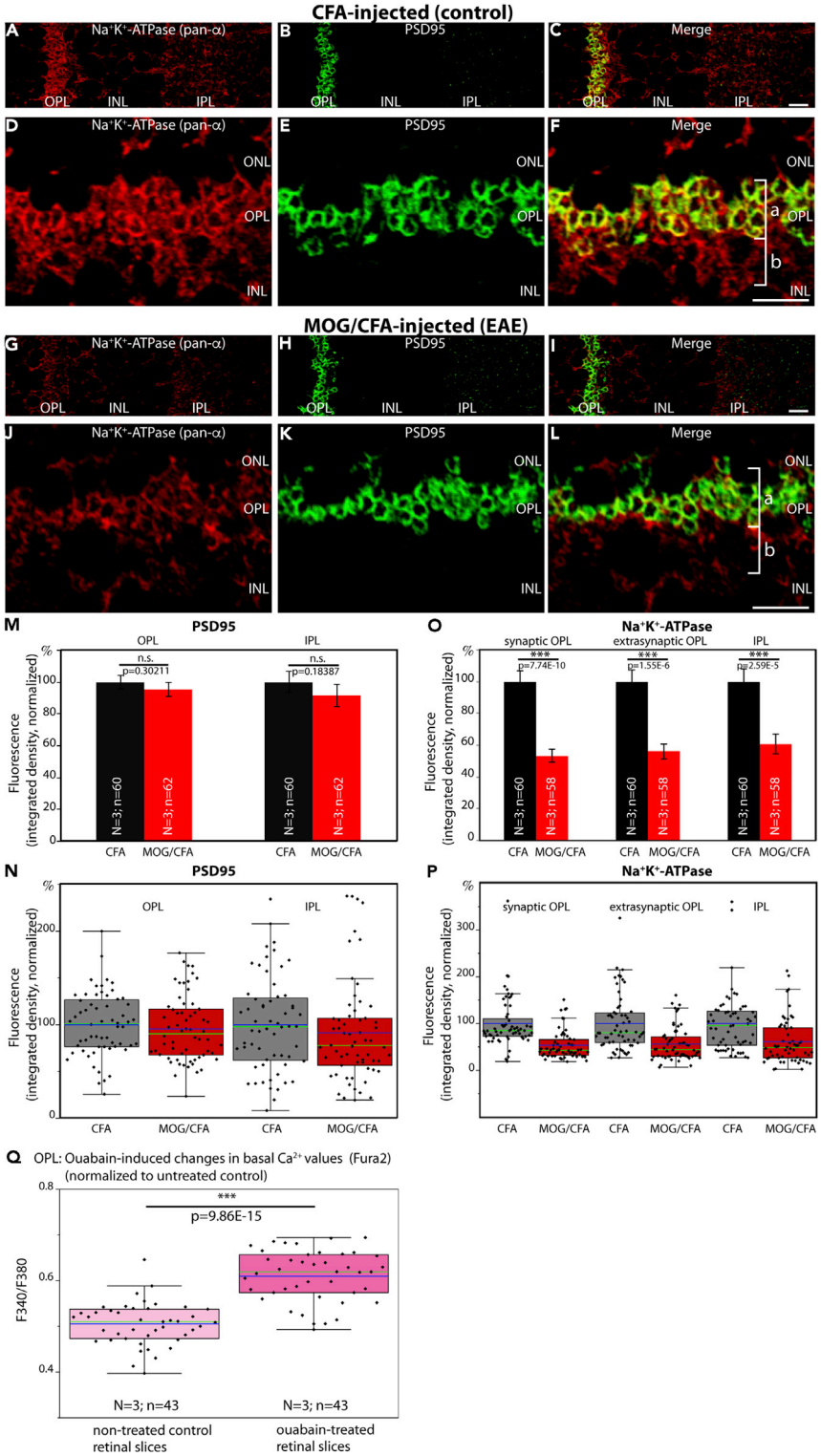

Figure 8. Decreased Expression of Na^+/K^+-ATPase in Photoreceptor Synapses of EAE Mice

Distribution of Na^+/K^+-ATPase in the OPL of CFA-injected control mice (A–F) and in MOG/CFA-injected EAE mice (G–L) processed 9 days after injection. Retinal sections (0.5 μm in thickness) were double-immunolabeled with a mouse monoclonal pan α-subunit Na^+/K^+-ATPase antibody and a rabbit polyclonal antibody against PSD95. PSD95 denotes the extension of presynaptic photoreceptor terminals. Quantification of immunolabeling signals is shown in (M–P). Statistical

Figure 8. *Continued*
significance in (M–P) was determined with Mann-Whitney U-test. In (Q), Fura2 ratiometric signals of basal Ca^{2+} levels in the OPL of control retinal slices from wild-type mice and retinal slices treated with the Na^+/K^+-ATPase inhibitor ouabain were plotted (N = 3 mice; n = 43 slices [ouabain]; N = 3 mice; n = 43 slices [untreated controls]). Statistical significance in (Q) was performed with Student t test. Values are depicted as mean ± S.E.M. (M and O). In the box-and-whiskers plots of the individual data points (N, P, and Q), mean values are indicated by blue horizontal bars and median values by green horizontal bars. Boxes represent 25^{th}–75^{th} percentiles of values and whiskers are equal to 1.5 times of the IQR. Abbreviations: ONL, outer nuclear layer; OPL, outer plexiform layer; INL, inner nuclear layer; IPL, inner plexiform layer; bracket a, synaptic portion of the OPL; bracket b, extra-synaptic, neuropil portion of the OPL; S.E.M., standard error of the mean; N = number of mice; n = number of total images analyzed from retinal sections. Scale bars: 5 μm (A–L).

2013; Blaustein 2018; Blaustein and Hamlyn, 2020). Interestingly, Na^+/K^+-ATPase can interact with CASPR1 (Zhang et al., 2019). At photoreceptor synapses, CASPR1 is altered early on in preclinical EAE (Dembla et al., 2018). Therefore, we studied whether the phenotype of increased basal Ca^{2+} might be caused by a change of Na^+/K^+-ATPase expression levels in the retina of MOG/CFA-injected mice compared with CFA-injected controls.

Decreased Expression of Na^+/K^+-ATPase in Photoreceptor Synapses of EAE Mice

In CFA-injected control mice, we found a strong expression of the Na^+/K^+-ATPase in the synaptic layers of the retina, similar to what was previously described (McGrail and Sweadner, 1986; Wetzel et al., 1999). In the OPL, a large portion of the Na^+/K^+-ATPase was localized to photoreceptor synapses as demonstrated by co-labeling with anti-PSD95 (Figure 8). PSD95, a component of the presynaptic cytoskeleton of the plasma membrane in photoreceptor terminals, delineates the presynaptic terminals (Koulen et al., 1998). Part of the Na^+/K^+-ATPase immunosignals was also present in the extra-synaptic, neuropil sub-layer of the OPL (Figures 8F and 8L). In the OPL of MOG/CFA-injected mice the immunolabeling intensity of Na^+/K^+ATPase was strongly reduced, both in the synaptic as well as in the extra-synaptic sublayer of the OPL (Figures 8G and 8J; for quantification see Figures 8O and 8P). In contrast, the intensity of PSD95 immunosignals was unchanged in MOG/CFA-injected mice compared with CFA-injected control mice (Figures 8M and 8N). The decreased Na^+/K^+-ATPase expression in the OPL of MOG/CFA-injected mice in comparison to CFA-injected control mice went in parallel to a decreased expression of CASPR1 in the OPL (Figure S8), similar to as previously described (Dembla et al., 2018).

In order to estimate the relevance of the observed decreased levels of Na^+/K^+-ATPase for the elevated presynaptic basal Ca^{2+} levels in photoreceptor synapses of MOG/CFA-injected mice, we incubated acute retinal slices from untreated wildtype mice in the presence or absence of the cardiotonic steroid ouabain, a well-characterized inhibitor of the Na^+/K^+-ATPase pump (Schatzmann, 1953; Repke, 1964; Hansen, 1984). In agreement with previous findings (Repke, 1964; Blaustein 1993; Zucker, 1993; Amaral et al., 2009; Milla et al., 2011), we observed an increase in presynaptic Ca^{2+} after treatment with ouabain (Figure 8Q). This finding suggests that the decreased expression of Na^+/K^+-ATPase in photoreceptor synapses in early EAE observed in the present study can contribute to the elevated basal Ca^{2+} levels in photoreceptor synapses of MOG/CFA-injected mice.

Decreased Expression of Plasma Membrane Ca^{2+} ATPase 2 (PMCA2), but Not of PMCA1, in Photoreceptor Synapses of EAE Mice

PMCAs are major Ca^{2+} extruding proteins in the retina (Krizaj et al., 2002). Therefore, we also analyzed the plasma membrane calcium ATPase (PMCA) proteins for potential alterations. PMCAs are key proteins of Ca^{2+} extrusion at the plasma membrane that are also expressed in photoreceptor terminals (Brini and Carafoli, 2011; Križaj, 2012; Cali et al., 2017; Stafford et al., 2017). Furthermore, a proteome study has found a portion of PMCA to be part of an active zone - associated protein network (Müller et al., 2010).

Similar to Na^+/K^+-ATPase (Figure 8), PMCA immunosignals were found both in the extra-synaptic neuropil portion as well as in the synaptic portion of the OPL, with the latter being demarcated by PSD95 immunolabeling (Figures 9, 10, S9, and S10).

Antibodies against PMCA1, the most abundant PMCA isoform, revealed no change in expression at the OPL in early EAE, both in the synaptic as well as in the extra-synaptic sub-layer (Figures 9 and S9). PMCA1 expression in the IPL was also unaffected (Figures 9 and S9). In contrast, antibodies against

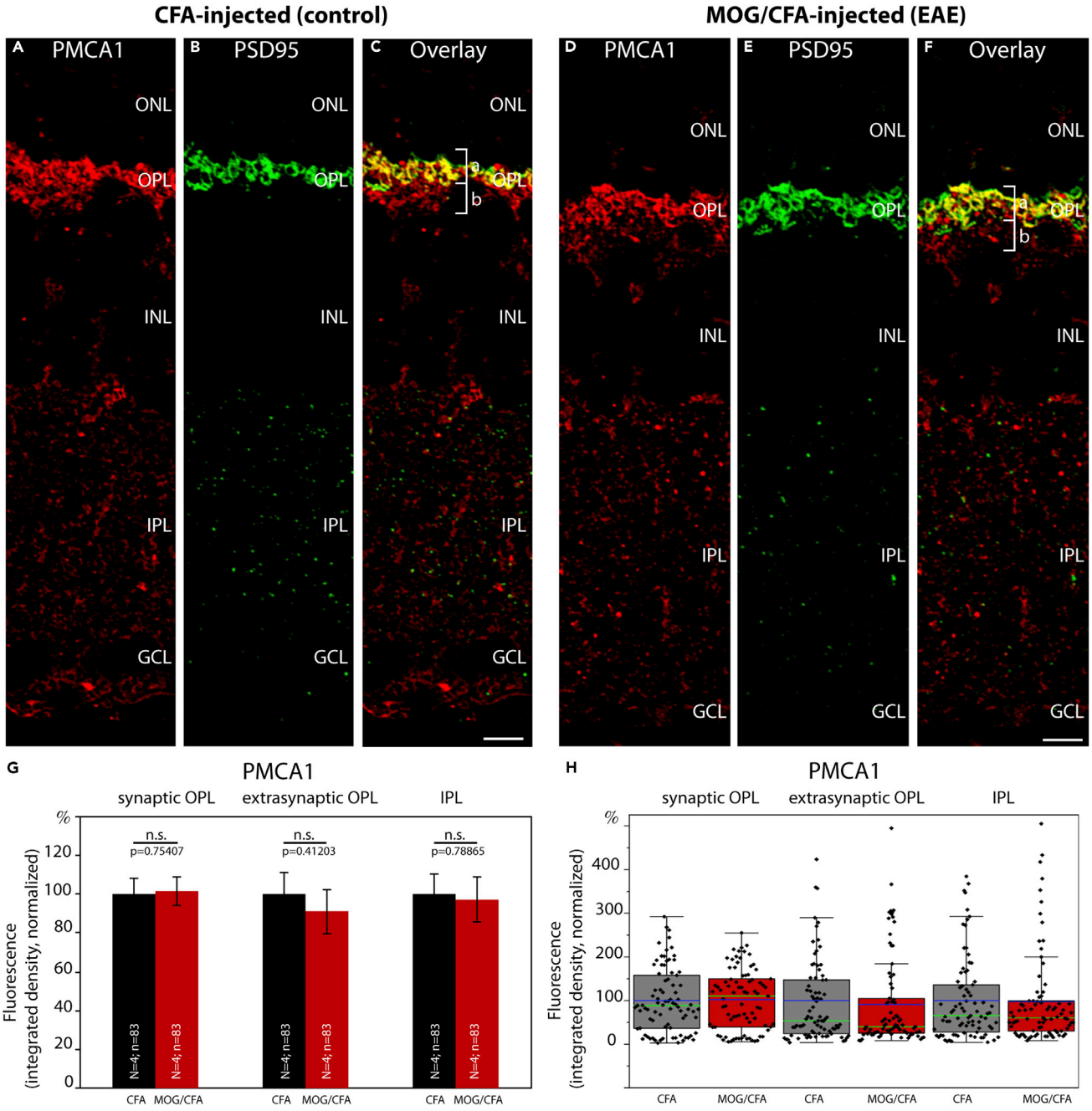

Figure 9. Expression of Plasma Membrane Ca^{2+} ATPase 1 (PMCA1) Is Unchanged in Photoreceptor Synapses of EAE Mice

(A–F) Retina sections (0.5 μm in thickness) from CFA- and MOG/CFA-injected mice processed 9 days after injection. Confocal analyses of rod photoreceptor synapses in the OPL immunolabeled with rabbit polyclonal antibody against PMCA1 and rabbit polyclonal antibody against PSD95 using the Fab method. The intensity of the PMCA1 immunosignals is quantified as integrated density in (G and H). Values are means ± S.E.M. (G). In the box-and-whiskers plots of the data in (H), mean values are labeled by blue horizontal bars and median values by green horizontal bars. Boxes represent 25^{th}–75^{th} percentiles of values, and whiskers are equal to 1.5 times of the interquartile range (IQR). Statistical significance was determined with Mann-Whitney U-test. Abbreviations: ONL, outer nuclear layer; OPL, outer plexiform layer; INL, inner nuclear layer; IPL, inner plexiform layer; GCL, ganglion cell layer; bracket a, synaptic sub-layer of the OPL; bracket b, extra-synaptic, neuropil sub-layer of the OPL; S.E.M., standard error of the mean; N = number of mice; n = number of images analyzed from retinal sections. Scale bars: 5 μm.

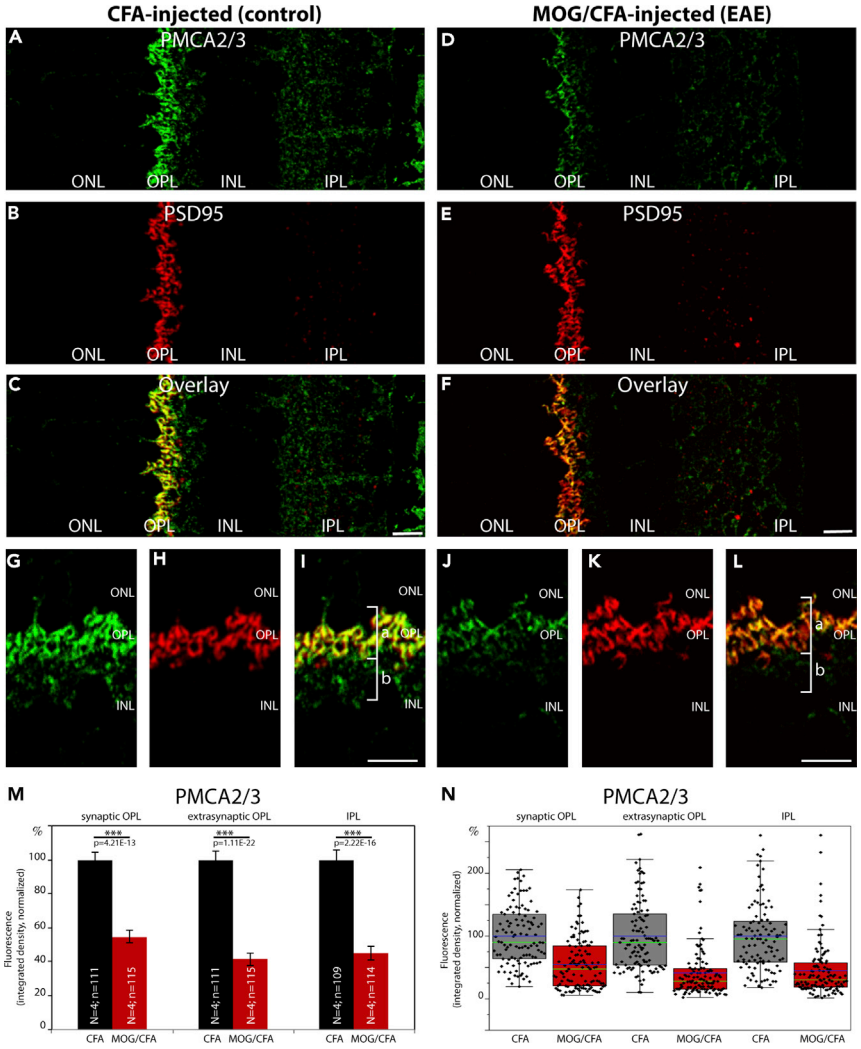

Figure 10. Decreased Expression of Plasma Membrane Ca^{2+} ATPase 2 (PMCA2) in Photoreceptor Synapses of EAE Mice

(A–L) Retina sections (0.5 μm in thickness) from CFA- and MOG/CFA-injected mice processed 9 days after injection. Confocal analyses of rod photoreceptor synapses in the OPL immunolabeled with mouse monoclonal antibody against PMCA2/3 and rabbit polyclonal antibody against PSD95. The intensity of the PMCA2/3 immunosignals is quantified as integrated density in (M and N). Values are means ± S.E.M. (M). In the box-and-whiskers plots of the data in (N), mean values are labeled by blue horizontal bars and median values by green horizontal bars. Boxes represent 25^{th}–75^{th} percentiles of values and whiskers are equal to 1.5 times of the interquartile range (IQR). Statistical significance was determined with Mann-Whitney U-test. Abbreviations: ONL, outer nuclear layer; OPL, outer plexiform layer; INL, inner nuclear layer; IPL, inner plexiform layer; bracket a, synaptic sub-layer of the OPL; bracket b, extra-synaptic, neuropil sub-layer of the OPL; S.E.M., standard error of the mean; N = number of mice; n = number of images analyzed from retinal sections. Scale bars: 5 μm.

PMCA2/3 revealed a significantly reduced signal intensity in the OPL of EAE mice in comparison to control mice, both in the synaptic as well as in the extra-synaptic sub-layer of the OPL (Figure 10). PMCA2/3 expression was also reduced in the IPL (Figure 10). A further independent antibody raised against PMCA2 also confirmed a strong reduction in signal intensity in the OPL of MOG/CFA-injected mice in comparison to CFA-injected control mice (Figure S10). These latter two antibodies propose that PMCA2 expression is reduced in the OPL of MOG/CFA-injected EAE mice in comparison to CFA-injected control mice. We did not further analyze PMCA3 because PMCA3 was previously reported to be not expressed in presynaptic photoreceptor terminals (Krizaj et al., 2002).

Western Blot Analyses

We also performed western blot analyses to check whether the global expression of the mentioned proteins was altered (Figure 11; for quantification, see Figures S11 and S12). From all the proteins only PMCA2/3 was found to be altered at a global level. Thus, decreased immunosignals of all the other proteins were based on de-enrichment/de-clustering but not due to a reduction in the global levels of protein expression.

DISCUSSION

In the current study, we observed that the clustering of active zone proteins at photoreceptor synapses is altered in the EAE mouse model of MS very early on in a preclinical stage. We found that central protein components of the Ca^{2+}-signaling machinery of photoreceptor active zones (Cav1.4, Cavβ2, and RIM2) were significantly less enriched at the active zone of photoreceptor synapse in MOG/CFA-injected mice in comparison to CFA-injected control mice. This was shown by immunolabeling of retinas obtained at the early, preclinical stage of EAE, at day 9 after injection. At this time point, no signs of demyelination were observed in the optic nerve (Dembla et al., 2018), arguing that these alterations are not secondary changes, e.g. due to optic nerve demyelination. Other proteins of the presynaptic terminal, such as PSD95 and PMCA1, were not affected, demonstrating that the changes at the active zone are specific and not resulting from global alterations of protein composition. The decreased enrichment of active zone proteins was not due to loss of synapses because the number of active zone puncta remained unchanged between EAE and control mice (Figures 1I, 1J, S1I, S1J, S2I, S2J, 3I, 3J, S4I, S4J; Figures 5I, 5J, S6I, and S6J). Instead, the length of the respective protein clusters at the active zone, as determined by SR-SIM measurements of immunolabeled active zone protein clusters (Cav1.4; Cavβ2), was found to be decreased (Figures 2 and 4). The decrease in the size of the Cav1.4/Cavβ2 protein clusters at the active zone was not due to a reduction of global expression of these proteins, as shown by western blot analyses (Figures 11A, 11C, 11E, and S11) but most likely result from an altered recruitment of these proteins to the active zone. Recently, it has been shown that the active zone of photoreceptor synapses can be modulated in size and that this dynamics occurs within a relatively short time frame (in ≈20 min; Dembla et al., 2020). A similar mechanism, i.e. loss of protein components from the active zone, could also be engaged in mediating the early synaptic changes in EAE.

In line with the morphological defects at the active zone, we also observed alterations of Ca^{2+} signaling in the presynaptic terminal. The amplitudes of high K^+-depolarization-evoked Ca^{2+} responses were significantly decreased in MOG/CFA-injected mice in comparison to CFA-injected control mice (Figure 7). The Fura2 responses were recorded at the OPL of retinal slices. In the OPL, photoreceptor synapses are highly enriched in a very organized fashion (see also Figure S7A) and harbor all the Cav1.4 voltage-gated Cav-channels that are expressed (Figure S3; see also Dembla et al., 2020). The strongest Fura2 responses were observed in the sub-layer of the OPL in which the photoreceptor terminals are located, as also verified by co-recording in RIBEYE-FP mice (Figure S7). Therefore, we think that the recorded depolarization-evoked responses are largely occurring at photoreceptor synapses although we cannot exclude some contribution from horizontal cells (for review, see Van Hook et al., 2019). The smaller amplitudes of depolarization-evoked Ca^{2+} responses in EAE are in line with the observed decreased enrichment of Cav-channel components and RIM2 protein at the active zone of EAE mice. The decreased enrichment of these active zone proteins in photoreceptor synapses and the decreased depolarization-evoked Ca^{2+} responses could contribute also to the previously observed reduced synaptic vesicle exocytosis in early EAE (Dembla et al., 2018) because vesicle exocytosis depends on Ca^{2+}. Recently, it has been proposed that the synaptic ribbon is involved in the delivery of active zone material to the active zone and for regulating the size of the active zone (Dembla et al., 2020). The synaptic ribbon complex itself is strongly affected in early EAE (Dembla et al., 2018), raising the possibility that disturbed trafficking at the ribbon complex might be involved in the decreased enrichment of active zone proteins at photoreceptor synapses in EAE. Clearly, further investigations will be required to reveal the molecular mechanisms. Additional proteins of the active zone (tom Dieck et al., 2012; Kiyonaka et al., 2012; Hagiwara et al., 2018) could also play an important role in the reorganization of the active zone in early, pre-clinical EAE. The reasons for the increased basal Ca^{2+} levels in photoreceptor synapses of EAE mice most likely involve additional pathways (see below).

Except for Cav1.4 α1 subunit, the analyzed proteins (RIM2, Cavβ2) are cytoplasmic proteins of the active zone. How could an auto-reactive immune system, activated in EAE, target the presynaptic active zone? The protein CASPR1 could play an important role. CASPR1 is an auto-antigen frequently targeted in MS

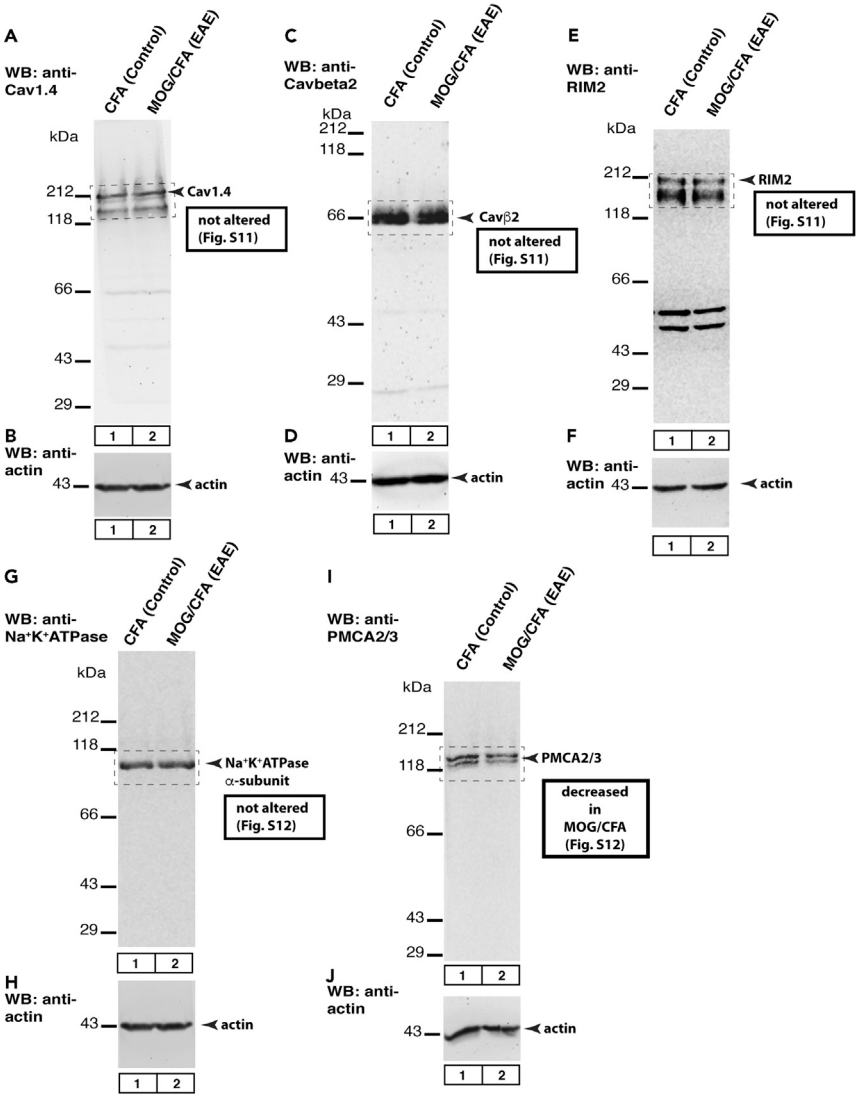

Figure 11. Western Blot Analyses

Western blot (WB) testing of global protein expression in retinal lysates obtained from MOG/CFA- and CFA-injected control retinas, isolated 9 days after injection. 40 μg of protein was loaded in each lane. In A, C, E, G, and I, the samples were probed with the indicated experimental antibodies. In B, D, F, H, and J, the same lanes were incubated with anti-actin antibody to verify equal protein loading of the MOG/CFA and CFA lanes. The boxed areas were quantified in Figures S11 and S12. Figure A–J show representative images from WB experiments repeated 7 times; for quantification of all WB results, see Figure S11 and S12.

(Stathopoulos et al., 2015). In the retina, CASPR1 is found in a protein complex with RIBEYE, the main component of synaptic ribbons (Dembla et al., 2018). In agreement with these biochemical data, ultrastructural analyses also show localization of CASPR1 in close proximity to the synaptic ribbon (Dembla et al., 2018). CASPR1 is also present at the paranodal region of the node of Ranvier (Gordon et al., 2014; Stathopoulos et al., 2015), on the luminal surface of brain microvascular endothelial cells (Zhang et al., 2019) as well as on dendritic processes of secondary neurons (Dembla et al., 2018). In the endothelium, CASPR1 can even serve as a receptor for pathogenic bacterial proteins that promote entry of the bacteria into the CNS (Zhao et al., 2018a, 2018b). CASPR1 also directly interacts with the β3-subunit of Na^+/K^+-ATPase in brain endothelial cells and this interaction is important for the activity, stabilization, and surface expression of Na^+/K^+-ATPase (Zhang et al., 2019). Interestingly, the β3-subunit of Na^+/K^+-ATPase is also present in photoreceptor synapses (McGrail and Sweadner, 1986; Blanco and Mercer, 1998; Wetzel et al., 1999) and

thus available to form complexes with CASPR1. In early EAE, auto-antibodies against CASPR1 lead to a decrease of CASPR1 expression at photoreceptor synapses (Dembla et al., 2018). Because CASPR1 is known to stabilize Na^+/K^+-ATPase, the observed decreased expression of Na^+/K^+-ATPase (Figures 8 and S8) could result from the decreased expression of CASPR1 in photoreceptor synapses in early EAE as observed by Dembla et al. (2018). Na^+/K^+-ATPase is also reduced in the extra-synaptic portion of the OPL, which might be due to a reduction of CASPR1 also at extra-synaptic sites or by further, independent mechanisms.

Decreased expression of Na^+/K^+-ATPase in photoreceptor terminals will lead to a diminished extrusion of Na^+ and an increase of intracellular Na^+. This increase of intracellular Na^+ could subsequently result in a secondary increase of intracellular Ca^{2+}, in analogy to well-characterized processes in the heart. In the heart, inhibition of Na^+/K^+-ATPase (e.g. by ouabain or other foxglove glycosides) leads to an increase of intracellular Na^+ that drives the Na^+/Ca^{2+}-exchanger (NCX) into the "reverse mode" with a concomitant increase of intracellular Ca^{2+} (e.g. Katz and Lorell, 2000; Hirota et al., 2007; Sibarov et al., 2012; Verkhratsky et al., 2018). Such a mechanism could principally also be responsible for the elevated resting cytosolic Ca^{2+} in retinal photoreceptor synapses, as it was also shown to be relevant in other synapses (e.g. Zucker, 1993). NCX is expressed in photoreceptor synapses although at low levels (Morgans et al., 1998) and predominantly in cone photoreceptor synapses that represent only a minor fraction of all photoreceptor synapses in the mouse retina (Johnson et al., 2007). Rod photoreceptors also possess a $Na^+/Ca^{2+}K^+$-exchanger (NCKX) (Schnetkamp, 1986; Cook and Kaupp, 1988; Reiländer et al., 1992). But NCKX expression in photoreceptors is restricted to the plasma membrane of the outer segments (Reid et al., 1990; Schnetkamp, 2013; Vinberg et al., 2015; Hassan and Lytton, 2020; Jalloul et al., 2020). In some systems, inhibition of the Na^+/K^+-ATPase by ouabain leads to an increase of cytosolic Ca^{2+} that is in part also mediated by increased Ca^{2+} release from the endoplasmic reticulum (ER)(Amaral et al., 2009; Stafford et al., 2017). The decreased expression of Na^+/K^+-ATPase that we observed in early EAE could lead to elevated resting Ca^{2+} concentrations by a similar mechanism in photoreceptor synapses. Interestingly, recently it was shown that the β-subunit of Cav-channels inhibits Ca^{2+} release from the ER(Belkacemi et al., 2018). This was demonstrated for the β3-subunit of voltage-gated Cav channels (Belkacemi et al., 2018). Rod photoreceptor synapses, the predominant type of photoreceptor synapses in the mouse retina, express the Cavβ2-subunit instead (Ball et al., 2002; Katiyar et al., 2015). Possibly, the β2-subunit of Cav-channels at photoreceptor synapses might play a similar role in inhibiting Ca^{2+} release from the ER in photoreceptor synapses. These ER-related mechanisms could also be linked to the Na^+/K^+-ATPase. The Na^+/K^+-ATPase appears to represent a central signaling hub that regulates—beyond its pump activity—various events relevant for presynaptic Ca^{2+} including the control of intracellular Ca^{2+} stores (Yuan et al., 2005; Pierre and Xie, 2006; Aperia, 2007; Liang et al., 2007; Liu et al., 2007; Nguyen et al., 2011; Sibarov et al., 2012; Luan et al., 2014; Shi et al., 2019).

Besides Na^+/K^+-ATPase, decreased clearance of Ca^{2+} by plasma membrane Ca^{2+} ATPases (PMCAs) could also contribute to elevated basal Ca^{2+} in the OPL of early EAE mice. PMCAs are known to be strongly expressed in photoreceptor synapses and other parts of the retina (Morgans et al., 1998; Johnson et al., 2007; Stafford et al., 2017). Using a monoclonal antibody against PMCA2/3, we found PMCA2/3 to be less enriched at photoreceptor synapse in MOG/CFA-injected animals (in comparison to CFA-injected control animals, Figure 10). This effect was observed to be specific for PMCA2/3 because the major PMCA isoform, PMCA1, was found to be unaffected (Figures 9 and S9). Also, an antibody specific for PMCA2 showed a similar reduction in staining intensity (Figure S10), as the antibody against PMCA2/3. PMCA3 is not expressed in detectable amounts at photoreceptor terminals (Krizaj et al., 2002). Therefore, we also assume that the decreased immunosignal in the OPL of MOG/CFA-injected mice obtained with the anti-PMCA2/3 antibody is mainly caused by a decrease in the synaptic expression of PMCA2. Of particular interest, PMCA2 was previously found to be altered in the spinal cord in the EAE mouse model of MS and responsible for early neuronal dysfunction (Nicot et al., 2003, 2005; Kurnellas et al., 2007; Mirabelli et al., 2019). Furthermore, PMCA2/3 was the only protein that we found to be reduced in western blot analyses (Figures 11, S11, and S12), indicating that PMCA2 could play a prominent role in the synaptic pathology in early EAE.

Also further other mechanisms could contribute to the increased basal Ca^{2+}, e.g. decreased Ca^{2+} clearance from the presynaptic terminals, e.g. via altered NCX/NCKX activity, mitochondrial Ca^{2+} clearance, SERCA pump activity, calcium-induced calcium release (CICR), or activities of plasma membrane ion channels as well as altered coupling between plasma membrane ion channels and calcium stores (Morgans et al.,

1998; Zenisek and Matthews, 2000; Amaral et al., 2009; Szikra et al., 2009; Wan et al., 2012; Križaj, 2012; Sibarov et al., 2012; Feske et al., 2015; Stafford et al., 2017; Ben-Kasus-Nissim et al., 2017; Verkhratsky et al., 2018; Shi et al., 2019). CICR is a well-known phenomenon at photoreceptor synapses (Cadetti et al., 2006; Szikra et al., 2009; Babai et al., 2010; Chen et al., 2015). In photoreceptor synapses, mitochondria are placed close to the synaptic ribbons (Johnson et al., 2007; Stone et al., 2008; Linton et al., 2010; Perkins et al., 2012; Graffe et al., 2015; Li et al., 2016) and possess a strong impact on Ca^{2+} regulation in retinal ribbon synapses (Zenisek and Matthews, 2000; Wan et al., 2012; Wong et al., 2019). Also, the cation chloride co-transporter NKCC1 is enriched in photoreceptor synapses (Shen et al., 2013) that can affect presynaptic Ca^{2+} (Thoreson et al., 2000, 2002, 2003). Future studies have to clarify which of these pathways also contribute to the observed elevated resting cytosolic Ca^{2+} levels in photoreceptor synapses in early EAE.

Our study demonstrated that the situation of Ca^{2+} homeostasis is already complex on day 9 of early preclinical EAE. Two key components relevant for determining baseline Ca^{2+} levels in photoreceptor synapses, Na^{+}/K^{+}−ATPase and PMCA2, were already altered at day 9. Based on these results, future studies might target even earlier time points. Our Fura2 imaging revealed dysfunctions of Ca^{2+} homeostasis as early as on day 7 of preclinical EAE.

In conclusion, we showed that the active zone of photoreceptor synapses is strongly affected in the early stages of EAE. These alterations of the active zone can contribute to the recently described changes in synaptic vesicle exocytosis present in photoreceptor synapses of EAE mice (Dembla et al., 2018). Constantly elevated basal levels of Ca^{2+} could lead to synapse dysfunctions, neurodegeneration, and neuronal cell death (Sancho-Pelluz et al., 2008; Gadjanski et al., 2009; Fairless et al., 2014; Rodriguez-Muela et al., 2015; Schaefer et al., 2016; Wong et al., 2019). Finally, MS patients also show some alterations in ERG that are compatible with altered photoreceptor synapse function, e.g. increased peak delay time of the b-wave/b-wave implicit time and some alterations in b-wave amplitude (Forooghian et al., 2006; Gundogan et al., 2007; Saidha et al., 2011; You et al., 2018; Filgueiras et al., 2019).

Limitations of the Study

The present study was performed on the experimental auto-immune encephalomyelitis (EAE) mouse model of MS. The EAE model is a very well-validated and frequently used mouse model of MS. Future investigations on MS patients should also provide further insights into retinal synaptic pathology in humans.

Resource Availability

Lead Contact

Further information and requests for resources and reagents should be directed to and will be fulfilled by the Lead Contact, Frank Schmitz (frank.schmitz@uks.eu).

Materials Availability

Available from the corresponding authors upon request.

Data and Code Availability

All data are included in the published article and the Supplemental Information, and any additional information will be available from the corresponding authors upon request.

METHODS

All methods can be found in the accompanying Transparent Methods supplemental file.

SUPPLEMENTAL INFORMATION

Supplemental Information can be found online at https://doi.org/10.1016/j.isci.2020.101830.

ACKNOWLEDGMENTS

The excellent technical assistance of Gabi Kiefer, Sylvia Brundaler, and Sabine Schmidt is gratefully acknowledged. We thank PD Dr. Elmar Krause/Prof. Dr. Jens Rettig for access to the SR-SIM microscope; Prof. Dr. Thomas C. Südhof for the kind gift of the PSD95 antibody, and Prof. Dr. Martin Biel for Cav1.4

knockout tissue. Work of the authors was supported by research grants from the German Research Community/DFG (FOR2289) to VF, KS, and FS and by a research grant from the Dr. Rolf M. Schwiete Foundation and Saarländische Staatskanzlei to FS. We acknowledge the funding programme Open Access Publishing of the Saarland University.

AUTHOR CONTRIBUTIONS

AM conducted embeddings, confocal and SR-SIM imaging experiments, Fura2 Ca^{2+} imaging, western blots, analyzed data, and developed the study together with FS. AM wrote the manuscript together with FS. RK contributed in establishing Fura2 Ca^{2+} imaging protocols along with AM. ED conducted embedding and imaging (Figures S1K–S1P). MD conducted embeddings and contributed materials (Figures S5A–S5F). PK generated fusion protein for generating Cav Nterm antibody. AB1 characterized Cavβ2 antibodies along with AM. MJ generated Cav Nterm, Cav Cterm antibodies, and synthesized peptides. AB2 provided guidance and insights into the Fura2 imaging experiments. VF initiated project parts and provided valuable materials and inputs at various stages of this work. KS wrote the relevant animal proposal, conducted mice injections and embeddings, and supported analyses. FS designed and supervised the study and wrote the article along with AM. All authors revised the manuscript.

DECLARATION OF INTERESTS

The authors declare no competing interests.

Received: June 10, 2020
Revised: October 10, 2020
Accepted: November 16, 2020
Published: December 18, 2020

REFERENCES

Aizman, O., Uhlen, P., Lal, M., Brismar, H., and Aperia, A. (2001). Ouabain, a steroid hormone that signals with slow calcium oscillations. Proc. Natl. Acad. Sci. U S A *98*, 13420–13424.

Amaral, E., Leite, L.F., Gomez, M.V., Prado, M.A.M., and Guatimosim, C. (2009). Ouabain evokes exocytosis dependent on ryanodine and mitochondrial calcium stores that is not followed by compensatory endocytosis at the neuromuscular junction. Neurochem. Int. *55*, 406–413.

Aperia, A. (2007). New roles for an old enzyme: Na,K-ATPase emerges as an interesting drug target. J. Intern. Med. *261*, 44–52.

Babai, N., Morgans, C.W., and Thoreson, W.B. (2010). Calcium-induced calcium release contributes to synaptic release from mouse rod photoreceptors. Neuroscience *165*, 1447–1456.

Ball, S.L., Powers, P.A., Shin, H.S., Morgans, C.W., Peachey, N.S., and Gregg, R.G. (2002). Role of the beta2 subunit of voltage-gated channels in the retinal outer plexiform layer. Invest. Ophthalmol. Vis. Sci. *43*, 1595–1603.

Bay, Y., Morgan, E.E., Giovannucci, D.R., Pierre, S.V., Philipson, K.D., Askari, A., and Liu, L. (2013). Different roles of the cardiac Na^+/Ca^{2+}-exchanger in ouabain-induced inotropy, cell signaling, and hypertrophy. Am. J. Physiol. Heart Circ. Physiol. *304*, H427–H435.

Belkacemi, A., Hui, X., Wardas, B., Laschke, M.W., Wissenbach, U., Menger, M.D., Lipp, P., Beck, A., and Flockerzi, V. (2018). IP3 receptor-dependent cytoplasmic Ca^{2+} signals are tightly controlled by Cavβ3. Cell Rep. *22*, 1339–1349.

Ben-Kasus Nissim, T., Zhang, X., Elazar, A., Roy, S., Stolwijk, J.A., Zhou, Y., Motiani, R.K., Gueguinou, M., Hempel, N., Hershfinkel, M., et al. (2017). Mitochondria control store-operated Ca^{2+} entry through Na^+ and redox signals. EMBO J. *36*, 797–815.

Ben-Nun, A., Kaushansky, N., Kawakami, N., Krishnamoorthy, G., Berer, K., Liblau, R., Hohlfeld, R., and Wekerle, H. (2014). From classic to spontaneous and humanized models of multiple sclerosis: impact on understanding pathogenesis and drug development. J. Autoimmun. *54*, 33–50.

Blanco, G., and Mercer, R.W. (1998). Isozymes of the Na-K-ATPase: heterogeneity in structure, diversity in function. Am. J. Physiol. *275*, 633–650.

Blaustein, M.P. (1993). Physiological effects of endogenous ouabain: control of intracellular stores and cell responses. Am. J. Physiol. Cell Physiol. *264*, C1367–C1387.

Blaustein, M.P. (2018). The pump, the exchanger, and the holy spirit: origins and 40-year evolution of ideas about the ouabain-Na^+ pump endocrine system. Am. J. Physiol. Cell Physiol. *314*, C3–C26.

Blaustein, M.P., and Hamlyn, J.M. (2020). Ouabain, endogenous ouabain and ouabain-like factors: the Na^+ pump, ouabain receptor, its linkage to NCX and its myriad functions. Cell Calcium *86*, 102159.

Brini, M., and Carafoli, E. (2011). The plasma membrane Ca^{2+} ATPase and the plasma membrane sodium calcium exchanger cooperate in the regulation of cell calcium. Cold Spring Harb. Perspect. Biol. *3*, a004168.

Cadetti, L., Bryson, E.J., Ciccone, C.A., Rabl, K., and Thoreson, W.B. (2006). Calcium-induced calcium release in rod photoreceptor terminals boosts synaptic transmission during maintained depolarization. Eur. J. Neurosci. *23*, 2983–3990.

Cali, T., Brini, M., and Carafoli, E. (2017). Regulation of cell calcium and role of plasma membrane calcium ATPases. Int. Rev. Cell Mol. Biol. *332*, 259–296.

Chen, M., van Hook, M.J., and Thoreson, W.B. (2015). Ca^{2+} diffusion through endoplasmic reticulum supports elevated intraterminal Ca^{2+} levels needed to sustain synaptic release from rods in darkness. J. Neurosci. *35*, 11364–11373.

Constantinescu, C.S., Farooqi, N., O'Brien, K., and Gran, B. (2011). Experimental autoimmune encephalomyelitis (EAE) as a model system for multiple sclerosis (MS). Br. J. Pharmacol. *164*, 1079–1106.

Cook, N.J., and Kaupp, U.B. (1988). Solubilization, purification, and reconstitution of the sodium-calcium exchanger from bovine retinal rod outer segments. J. Biol. Chem. *263*, 11382–11388.

Criscuolo, C., Cianflone, A., Lanzillo, R., Carrella, A., Napolitano, F., de Cegli, R., de Candia, P., La Rocca, C., Petrozziello, T., Matarese, G., et al. (2019). Glatiramer acetate modulates ion channel expression and calcium homeostasis in B cells of patients with relapsing-remitting multiple sclerosis. Sci. Rep. *9*, 4208.

Dembla, E., Dembla, M., Maxeiner, S., and Schmitz, F. (2020). Synaptic ribbons foster active zone stability and illumination-dependent active zone enrichment of RIM2 and Cav1.4 in

photoreceptor synapses. Sci. Rep. *10*, 5957, https://doi.org/10.1038/s41598-020-62734-0.

Dembla, M., Kesharwani, A., Natarajan, S., Fecher-Trost, C., Fairless, R., Williams, S.K., Flockerzi, V., Diem, R., Schwarz, K., and Schmitz, F. (2018). Early auto-immune targeting of photoreceptor ribbon synapses in mouse models of multiple sclerosis. EMBO Mol. Med. *10*, e8926.

Dendrou, C.A., Fugger, L., and Friese, M.A. (2015). Immunopathology of multiple sclerosis. Nat. Rev. Immunol. *15*, 545–558.

Deng, L., Kaeser, P.S., Xu, W., and Südhof, T.C. (2011). RIM proteins activate vesicle priming by reversing homodimerization of Munc13. Neuron *69*, 317–331.

Eggermann, E., Bucurenciu, I., Goswami, S.P., and Jonas, P. (2011). Nanodomain coupling between Ca^{2+} channels and sensors of exocytosis at fast mammalian synapses. Nat. Rev. Neurosci. *13*, 7–21.

Fairless, R., Williams, S.K., Hoffmann, D.B., Stojic, A., Hochmeister, S., Schmitz, F., Storch, M.K., and Diem, R. (2012). Preclinical neurodegeneration in a mouse model of multiple sclerosis. J. Neurosci. *32*, 5585–5597.

Fairless, R., Williams, S.K., and Diem, R. (2014). Dysfunction of neuronal calcium signaling in neuroinflammation and neurodegeneration. Cell Tiss. Res. *357*, 455–462.

Faissner, S., Plemel, J.R., Gold, R., and Yong, W. (2019). Progressive multiple sclerosis: from pathophysiology to therapeutic strategies. Nat. Rev. Drug Discov. *18*, 905–922.

Feske, S., Wulff, H., and Skolnik, E.Y. (2015). Ion channels in innate and adaptive immunity. Annu. Rev. Immunol. *33*, 291–353.

Filgueiras, T.G., Oyamada, M.K., Preti, R.C., Apostolos-Pereira, S., Callegaro, D., and Monteiro, M.L.R. (2019). Outer retinal dysfunction on multifocal electroretinography may help differentiating multiple sclerosis from neuromyelitis optica spectrum disorders. Front. Neurol. *10*, 928.

Forooghian, F., Sproule, M., Westall, C., Gordon, L., Jirawuthiworavong, G., Shimazaki, K., and O'Connor, P. (2006). Electroretinographic abnormalities in multiple sclerosis: possible role for retinal autoantibodies. Doc. Ophthalmol. *113*, 123–132.

Gadjanski, I., Boretius, S., Williams, S.K., Lingor, P., Knöfele, J., Sättler, M.B., Fairless, R., Hochmeister, S., Sühs, K.W., Michaelis, T., et al. (2009). Role of N-type voltage-dependent calcium channels in autoimmune optic neuritis. Ann. Neurol. *66*, 81–93.

Gordon, A., Adamsky, K., Vainshtein, A., Frechter, S., Dupree, J.L., Rosenbluth, J., and Peles, E. (2014). Caspr and Caspr2 are required for both radial and longitudinal organization of myelinated axons. J. Neurosci. *34*, 14820–14826.

Grabner, C.P., Gandini, M.A., Rehak, R., Le, Y., Zamponi, G.W., and Schmitz, F. (2015). RIM1/2-mediated facilitation of Cav1.4 channel opening is required for Ca^{2+}-stimulated release in mouse photoreceptors. J. Neurosci. *35*, 13133–13147.

Graffe, M., Zenisek, D., and Taraska, J.W. (2015). A marginal band of microtubules transports and organizes mitochondria in retinal bipolar synaptic terminals. J. Gen. Physiol. *146*, 109–117.

Gundogan, F.C., Demirkaya, S., and Sobaci, G. (2007). Is optical coherence tomography really a new biomarker candidate in multiple sclerosis ? – a new structural and functional evaluation. Invest. Ophthalmol. Vis. Sci. *48*, 5773–5781.

Habbas, S., Santello, M., Becker, D., Stubbe, H., Zappia, G., Liaudet, N., Klaus, F.R., Kollias, G., Fontana, A., Pryce, C.R., et al. (2015). Neuroinflammatory TNFα impairs memory via astrocyte signaling. Cell *163*, 1730–1741.

Hagiwara, A., Kitahara, Y., Grabner, C.P., Vogl, C., Abe, M., Kitta, R., Ohta, K., Nakamura, K., Sakimura, K., Moser, T., et al. (2018). Cytomatrix proteins CAST and ELKS regulate retinal photoreceptor development and maintenance. J. Cell Biol. *217*, 3993–4006.

Haider, L., Simeonidou, C., Steinberger, G., Harmetner, S., Grigoiadis, N., Deretzki, G., Kovacs, C.G., Kitzelnigg, A., Lassmann, H., and Frischer, J.M. (2014). Multiple sclerosis deep grey matter: the relation between demyelination, neurodegeneration, inflammation and iron. J. Neurol. Neurosurg. Psychol. *85*, 1386–1399.

Hallermann, S., and Silver, R.A. (2013). Sustained rapid vesicular release at active zones: potential roles for vesicle tethering. Trends Neurosci. *36*, 185–194.

Han, Y., Kaeser, P.S., Südhof, T.C., and Schneggenburger, R. (2011). RIM determines Ca^{2+}-channel density and vesicle docking at the presynaptic active zone. Neuron *69*, 304–310.

Hansen, O. (1984). Interaction of cardiac glycosides with Na^+K^+-activated ATPase. A biochemical link to digitalis-induced inotropy. Pharmacol. Rev. *36*, 143–163.

Hassan, M.T., and Lytton, J. (2020). Potassium-dependent sodium-calcium exchanger (NCKX) isoforms and neuronal function. Cell Calcium *86*, 102135, https://doi.org/10.1016/j.ceca.2019.102135.

Hirota, S., Pertens, E., and Janssen, L.J. (2007). A reverse mode of the Na^+/Ca^{2+} exchanger provides a source of Ca^{2+} for store refilling following agonist-induced Ca^{2+} mobilization. Am. J. Physiol. Lung Cell Mol. Physiol. *292*, L438–L447.

Hundehege, P., Fernandez-Orth, J., Römer, P., Ruck, T., Müntefering, T., Eichler, S., Cerina, M., Epping, L., Albrecht, S., Mehke, A.F., et al. (2018). Targeting voltage-dependent calcium channels with prepabaline exerts a direct neuroprotective effect in an animal model of multiple sclerosis. Neurosignals *26*, 77–93.

Ingwersen, J., De Santi, L., Wingerath, B., Graf, J., Koop, B., Schneider, R., Hecker, C., Schröter, F., Bayer, M., Engelke, A.D., et al. (2018). Nimodipine confers clinical improvement in two models of experimental autoimmune encephalomyelitis. J. Neurochem. https://doi.org/10.1111/jnc.14324.

Jalloul, A.H., Szerencsei, R.T., Rogasevskaia, T.P., and Schnetkamp, P.P.M. (2020). Structure-function relationships of K^+-dependent Na^+/Ca^{2+} exchangers (NCKX). Cell Calcium *86*, 102153, https://doi.org/10.1016/j.ceca.2019.102153.

Johnson, J.E., Jr., Perkins, G.A., Giddabasappa, A., Chaney, S., Xiao, W., White, A.D., Brown, J.M., Waggoner, J., Ellisman, M.H., and Fox, D.A. (2007). Spatiotemporal regulation of ATP and Ca^{2+} dynamics in vertebrate rod and cone ribbon synapses. Mol. Vis. *13*, 887–919.

Joiner, M.L., and Lee, A. (2015). Voltage-gated Cav1 channels in disorders of vision and hearing. Curr. Mol. Pharmacol. *8*, 143–148.

Jürgens, T., Jafari, M., Kreutzfeld, M., Bahn, E., Brück, W., Kerschensteiner, M., and Merkler, D. (2016). Reconstruction of single cortical projection neurons reveals primary spine loss in multiple sclerosis. Brain *139*, 39–46.

Kaeser, P.S., Deng, L., Wang, Y., Dulubova, I., Liu, X., Rizo, J., and Südhof, T.C. (2011). RIM proteins tether Ca^{2+}-channels to presynaptic active zones via a direct PDZ-domain interaction. Cell *144*, 282–295.

Kaplan, J.K. (2002). Biochemistry of Na,K-ATPase. Annu. Rev. Biochem. *71*, 511–535.

Katiyar, R., Weissgerber, P., Roth, E., Dörr, J., Sothilingam, V., Garcia Garrido, M., Beck, S.C., Seeliger, M., Beck, A., Schmitz, F., and Flockerzi, V. (2015). Influence of the β2-subunit of L-type voltage-gated Cav channels on the structural and functional development of photoreceptor ribbon synapses. Invest. Ophthalmol. Vis. Sci. *56*, 2312–2324.

Katz, A.M., and Lorell, B.H. (2000). Regulation of cardiac contraction and relaxation. Circulation *102*, 74.

Kim, M.H., Li, G.L., and von Gersdorff, H. (2013). Single Ca^{2+} channels and exocytosis at sensory synapses. J. Physiol. *13*, 3167–3178.

Kiyonaka, S., Nakajima, H., Takada, Y., Hida, Y., Yoshioka, T., Hagiwara, A., Kitajima, I., Mori, Y., and Ohtsuka, T. (2012). Physical and functional interaction of the active zone protein CAST/ARC2 and the β-subunit of the voltage-dependent Ca^{2+}-channel. J. Biochem. *152*, 149–159.

Koulen, P., Fletcher, E.L., Craven, S.E., Bredt, D.S., and Wässle, H. (1998). Immunocytochemical localization of the postsynaptic density protein PSD-95 in the mammalian retina. J. Neurosci. *18*, 10136–10149.

Krizaj, D., Demarco, S.J., Johnson, J., Strehler, E.E., and Copenhagen, D.R. (2002). Cell-specific expression of plasma membrane calcium ATPase isoforms in retinal neurons. J. Comp. Neurol. *451*, 1–21.

Križaj, D. (2012). Calcium stores in vertebrate photoreceptors. Adv. Exp. Med. Biol. *740*, 873–889.

Kurnellas, M.P., Donahue, K.C., and Elkabes, S. (2007). Mechanisms of neuronal damage in multiple sclerosis and its animal models: role of calcium pumps and exchangers. Biochem. Soc. Trans. *35*, 923–926.

Lagnado, L., and Schmitz, F. (2015). Ribbon synapses and visual processing in the retina. Annu. Rev. Vis. Sci. *1*, 235–262.

Lassmann, H., Bruck, W., and Lucchinetti, C.F. (2007). The immunopathology of multiple sclerosis: an overview. Brain Pathol. *17*, 210–218.

Li, S., Mitchell, J., Briggs, D.J., Young, J.K., Long, S.S., and Fuerst, P.G. (2016). Morphological diversity of the rod spherule: a study of serially reconstructed electron micrographs. PLoS One *11*, e0150024, https://doi.org/10.1371/journal.pone.0150024.

Liang, M., Tian, J., Liu, L., Pierre, S., Liu, J., Shapiro, J., and Xie, Z.J. (2007). Identification of a pool of non-pumping Na/K-ATPase. J. Biol. Chem. *282*, 10585–10593.

Linton, J.D., Holzhausen, L.C., Babai, N., Song, H., Miyagishima, K.J., Stearns, G.W., Lindsay, K., Wei, J., Chertov, A.O., Peters, T.A., et al. (2010). Flow of energy in the outer retina in darkness and in light. Proc. Natl. Acad. Sci. U S A *107*, 8599–8604.

Liu, L., Zhao, X., Pierre, S.V., and Askari, A. (2007). Association of PI3K-Akt signaling pathwy with digitalisinduced hypertrophy of cardiac myocytes. Am. J. Physiol. Cell Physiol. *293*, C1489–C1497.

Loewe, M.J., Koenig, K.A., Beall, E.B., Sakaie, K.A., Stone, L., Bermel, R., and Phillips, M.D. (2014). Anatomic connectivity assessed using pathway radial diffusivity is related to functional connectivity in monosynaptic pathways. Brain Connect. *4*, 558–565.

Löhner, M., Babai, N., Müller, T., Gierke, K., Atorf, J., Joachimsthaler, A., Peukert, A., Martens, H., Feigenspan, A., Kremers, J., et al. (2017). Analysis of RIM expression and function at mouse photoreceptor ribbon synapses. J. Neurosci. *37*, 7848–7863.

Luan, Z., Reddig, K., and Li, H.S. (2014). Loss of Na^+/K^+-ATPase in Drosophila photoreceptors leads to blindness and age-dependent neurodegeneration. Exp. Neurol. *261*, 791–801.

Mandolesi, G., Gentile, A., Musella, A., Fresegna, D., De Vito, F., Bullitta, S., Sepman, H., Marfia, G.A., and Centonze, D. (2015). Synaptopathy connects inflammation and neurodegeneration in multiple sclerosis. Nat. Rev. Neurol. *11*, 711–724.

Matthews, G., and Fuchs, P. (2010). The diverse roles of ribbon synapses in sensory neurotransmission. Nat. Rev. Neurosci. *11*, 812–822.

Maxeiner, S., Luo, F., Tan, A., Schmitz, F., and Südhof, T.C. (2016). How to make a synaptic ribbon: RIBEYE deletion abolishes ribbons in retinal synapses and disrupts neurotransmitter release. EMBO J. *35*, 1098–1114.

McGrail, K.M., and Sweadner, K.J. (1986). Immunofluorescent localization of two different Na,K-ATPase in the rat retina and in identified dissociated retinal cells. J. Neurosci. *6*, 1272–1283.

Meissner, M., Weissgerber, P., Londono, J.E., Prenen, J., Link, S., Ruppenthal, S., Molkentin, J.D., Lipp, P., Nilius, B., Freichel, M., and Flockerzi, V. (2011). Moderate calcium channel dysfunction in adult mice with inducible cardiomyocyte-specific excision of the cacnb2 gene. J. Biol. Chem. *286*, 15875–15882.

Milla, J., Montesinos, M.S., Machado, J.D., Borges, R., Alonso, E., Moreno-Ortega, A.J., Cano-Abad, M.F., Garcia, A.G., and Ruiz-Nuno, A. (2011). Ouabain enhances exocytosis through the regulation of calcium handling by the endoplasmic reticulum of chromaffin cells. Cell Calcium *50*, 332–342.

Mirabelli, E., Ni, L., Li, L., Acioglu, C., Heary, R.F., and Elkabes, S. (2019). Pathological pain processing in mouse models of multiple sclerosis and spinal cord injury: contribution of plasma membrane calcium ATPase 2 (PMCA2). J. Neuroinflammation *16*, 207.

Morgans, C.W., El Far, O., Berntson, A., Wässle, H., and Taylor, W.R. (1998). Calcium extrusion from mammalian photoreceptor terminals. J. Neurosci. *18*, 2467–2474.

Moser, T., Grabner, C.P., and Schmitz, F. (2020). Sensory processing at ribbon synapses in the retina and cochlea. Physiol. Rev. *100*, 103–144.

Müller, C.S., Haupt, A., Bildl, W., Schindler, J., Knaus, H.G., Meissner, M., Ramner, B., Striessnig, J., Flockerzi, V., Fakler, B., and Schulte, U. (2010). Quantitative proteomics of the Cav2 channel nano-environments in the mammalian brain. Proc. Natl. Acad. Sci. U S A *107*, 14950–14957.

Nanou, E., and Catterall, W.A. (2018). Calcium channels, synaptic plasticity and neuropsychiatric disease. Neuron *98*, 466–481.

Nicot, A., Ratnakar, P.V., Ron, Y., Chen, C.C., and Elkabes, S. (2003). Regulation of gene expression in experimental autoimmune encephalomyelitis indicates early neuronal dysfunction. Brain *126*, 398–412.

Nicot, A., Kurnellas, M., and Elkabes, S. (2005). Temporal pattern of plasma membrane calcium ATPase 2 expression in the spinal cord correlates with the course of clinical symptoms in two rodent models of autoimmune encephalomyelitis. Eur. J. Neurosci. *21*, 2660–2670.

Nguyen, A.N.T., Jansson, K., Sanchez, G., Sharma, M., Reif, G.A., Wallace, D.P., and Blanco, G. (2011). Ouabain activates the Na-K-ATPase signalosome to induce autosomal dominant polycystic kidney disease cell proliferation. Am. J. Physiol. Ren. Physiol. *301*, F897–F906.

Okawa, H., Yu, W.Q., Matti, U., Schwarz, K., Odermatt, B., Zhong, H., Tsukamoto, Y., Lagnado, L., Rieke, F., Schmitz, F., and Wong, R.O. (2019). Dynamic assembly of ribbon synapses and circuit maintenance in a vertebrate sensory system. Nat. Commun. *10*, 2167.

Pangrsic, T., Singer, J.H., and Koschak, A. (2018). Voltage-gated calcium channels: key players in sensory coding in the retina and inner ear. Physiol. Rev. *98*, 2063–2096.

Perkins, G.A., Scott, R., Perez, A., Ellisman, M.H., Johnson, J.E., and Fox, D.A. (2012). Bcl-xL-mediated remodeling of rod and cone synaptic mitochondria adter postnatal lead exposure: electron microscop, tomography and oxygen consumption. Mol. Vis. *18*, 3029–3048.

Pierre, S.V., and Xie, Z. (2006). The Na,K-ATPase receptor complex: its organization and membership. Cell Biochem. Biophys. *46*, 303–316.

Ravens, U., and Himmel, H.M. (1999). Drugs preventing Na^+ and Ca^{2+} overload. Pharmacol. Res. *39*, 167–174.

Reid, D.M., Friedel, U., Molday, R.S., and Cook, N.J. (1990). Identification of the sodium-calcium exchanger as the major ricin-binding glycoprotein of bovine rod outer segments and its localization to the plasma membrane. Biochemistry *29*, 1601–1607.

Reiländer, H., Achilles, A., Friedel, U., Maul, G., Lottspeich, F., and Cook, N.J. (1992). Primary structure and funtional expression of the Na/Ca, K-exchanger from bovine rod photoreceptors. EMBO J. *11*, 1689–1695.

Repke, K., and Portius, H.J. (1963). On the identity of the ion-pumping ATPase in the cell membrane of the myocardium with a digitalis receptor enzyme. Experientia *19*, 452–458.

Repke, K. (1964). Über den biochemischen Wirkungsmechanismus von Digitalis. Klin. Wochenschr. *42*, 157–165.

Rizzo, F.R., Musella, A., De Vito, F., Fresegna, D., Bullita, S., Vanni, V., Guadalupi, L., Stampanoni Bassi, M., Buttari, F., Mandolesi, G., et al. (2018). Tumor necrosis factor and interleukin-1β modulate synaptic plasticity during neuroinflammation. Neural Plast. *2018*, 8430123.

Robinson, A.P., Harp, C.T., Noronha, A., and Miller, S.D. (2014). The experimental autoimmune encephalomyelitis (EAE) model of MS: utility for understanding disease pathophysiology and treatment. Handb. Clin. Neurol. *122*, 173–189.

Rodriguez-Muela, N., Hernandez-Pinto, A.M., Serrano-Puebla, A., Garcia-Ledo, L., Latorre, S.H., de la Rosa, E.J., and Boya, P. (2015). Lysosomal membrane permeabilization and autophagy blockade contribute to photoreceptor cell death in a mouse model of retinitis pigmentosa. Cell Death Differ. *22*, 476–487.

Saidha, S., Syc, S.B., Ibrahim, M.A., Eckstein, C., Warner, C.V., Farrell, S.K., Oakley, J.D., Durbin, M.K., Meyer, S.A., Balcer, L.J., et al. (2011). Primary retinal pathology in multiple sclerosis as detected by optical coherence tomography. Brain *134*, 518–533.

Sancho-Pelluz, J., Arango-Gonzalez, B., Kustermann, S., Romero, F.J., Van Veen, T., Zrenner, E., Ekström, P., and Paquet-Durand, F. (2008). Photoreceptor cell death mechanisms in inherited retinal degeneration. Mol. Neurobiol. *38*, 253–269.

Schaefer, K.A., Toral, M.A., Velez, G., Cox, A.J., Baker, S.A., Borcherding, N.C., Colgan, D.F., Bondada, V., Mashburn, C.B., Yu, C.G., et al. (2016). Calpain-5 expression in the retina localizes to photoreceptor synapses. Invest. Ophthalmol. Vis. Sci. *57*, 2509–2521.

Schampel, A., Volovitch, O., Koeniger, T., Scholz, C.J., Jörg, S., Linker, R.A., Wischmeyer, E., Wunsch, M., Hell, J.W., Ergün, S., and Kuerten, S. (2017). Nimodipine fosters remyelination in a mouse model of multiple sclerosis and induces microglia-specific apoptosis. Proc. Natl. Acad. Sci. U S A *114*, E3295–E3304.

Schattling, B., Engler, J.B., Volkmann, C., Rothammer, N., Woo, M.S., Petersen, M., Winkler, I., Kaufmann, M., Rosenkranz, S.C.,

Fejtova, A., et al. (2019). Bassoon proteinopathy drives neurodegeneration in multiple sclerosis. Nat. Neurosci. *22*, 887–896.

Schatzmann, H.J. (1953). Cardiac glycosides as inhibitors of active potassium and sodium transport by erythrocyte membrane. Helv. Physiol. Pharmacol. Acta *11*, 346–354.

Schmitz, F., Königstorfer, A., and Südhof, T.C. (2000). RIBEYE, a component of synaptic ribbons: a protein's journey through evolution provides insight into synaptic ribbon function. Neuron *28*, 857–872.

Schnetkamp, P.P. (1986). Sodium-calcium exchange in the outer segments of bovine rod photoreceptors. J. Physiol. *373*, 25–45.

Schnetkamp, P.P.M. (2013). The Slc24 gene family of Na^+/Ca^{2+}-K^+-exchangers: from sight and smell to memory consolidation and skin pigmentation. Mol. Asp. Med. *34*, 455–464.

Shen, W., Purpura, L.A., Li, B., Nan, C., Chang, I.J., and Ripps, H. (2013). Regulation of synaptic transmission at the photoreceptor terminal: a novel role for the cation-chloride co-transporter NKCC1. J. Physiol. *591*, 133–147.

Shi, M., Cao, L., Cao, X., Zhu, M., Zhang, X., Wu, Z., Xiong, S., Xie, Z., Yang, Y., Chen, J., et al. (2019). DR-region of Na+/K+ ATPase is a target to treat excitotoxicity and strok. Cell Death Dis. *10*, 6, https://doi.org/10.1038/s41419-018-1230-5.

Sibarov, D.A., Bolshakov, A.E., Abushik, P.A., Krivoi, I.I., and Antonov, S. (2012). Na^+,K^+-ATPase functionally interacts with the plasma membrane Na^+, Ca^{2+}-exchanger to prevent Ca^{2+} overload and neuronal apoptosis in excitotoxic stress. J. Pharmacol. Exp. Ther. *343*, 596–607.

Skou, J.C. (1998). Nobel Lecture. The identification of the sodium pump. Biosci. Rep. *18*, 155–169.

Stafford, N., Wilson, C., Oceandy, D., Neyses, L., and Cartwright, E.J. (2017). The plasma membrane calcium ATPases and their role as major new players in human disease. Physiol. Rev. *97*, 1089–1125.

Stampanoni Bassi, M., Mori, F., Buttari, F., Marfia, G.A., Sancesario, A., Centonze, D., and Iezzi, E. (2017). Neurophysiology of synaptic functioning in multiple sclerosis. Clin. Neurophysiol. *128*, 1148–1157.

Stathopoulos, P., Alexopoulos, H., and Dalakas, M.C. (2015). Autoimmune antigenic targets at the node of Ranvier in demyelinating disorders. Nat. Rev. Neurol. *11*, 143–156.

Stone, J., van Driel, D., Valter, K., Rees, S., and Provis, J. (2008). The location of mitochondria in mammalian photoreceptors: relation to retinal vasculature. Brain Res. *1189*, 58–69.

Südhof, T.C. (2012a). The presynaptic active zone. Neuron *75*, 11–25.

Südhof, T.C. (2012b). Calcium control of neurotransmitter release. Cold Spring Harb. Perspect. Biol. *4*, a011353.

Südhof, T.C. (2014). The molecular machinery of neurotransmitter release (Nobel lecture). Angew. Chem. Int. Ed. *53*, 12696–12717.

Szikra, T., Barabas, P., Bartoletti, T.M., Huang, W., Akopian, A., Thoreson, W.B., and Krizaj, D. (2009). Calcium homeostasis and cone signaling are regulated by interactions between calcium stores and plasma membrane ion channels. PLoS One *4*, e6723, https://doi.org/10.1371/journal.pone.0006723.

Thoreson, W.B., Nitzan, R., and Miller, R.F. (2000). Chloride efflux inhibits single calcium channel open probability in vertebrate photoreceptors: chloride imaging and cell-attached patch-clamp recordings. Vis. Neurosci. *17*, 197–206.

Thoreson, W.B., Stella, S.L., Jr., Bryson, E.J., Clements, J., and Witkovsky, P. (2002). D2-like dopamine receptors promote interactions between calcium and chloride channels that diminish rod synaptic transfer in the salamander retina. Vis. Neurosci. *19*, 235–247.

Thoreson, W.B., Bryson, E.J., and Rabl, K. (2003). Reciprocal interactions between calcium and chloride in rod photoreceptors. J. Neurophysiol. *90*, 1747–1753.

tom Dieck, S., Specht, D., Strenzke, N., Hida, Y., Krishnamoorthy, V., Schmidt, K.F., Inoue, E., Ishizaki, H., Tanaka-Okamoto, M., Miyoshi, J., et al. (2012). Deletion of the presynaptic scaffold CAST reduces active zone size in photoreceptors and impairs visual processing. J. Neurosci. *32*, 12192–12203.

Van Hook, M., Nawy, S., and Thoreson, W.B. (2019). Voltage- and calcium-gated ion channels of neurons in the vertebrate retina. Prog. Ret. Eye Res. *72*, 100760.

Verkhratsky, A., Trebak, M., Perocchi, F., Khananshvili, D., and Sekler, I. (2018). Crosslink between calcium and sodium signalling. Exp. Physiol. *103*, 157–169.

Vinberg, F., Wang, T., Molday, R.S., Chen, J., and Kefalov, V.J. (2015). A new mouse model for stationary night blindness with mutant slc24a1 explains the pathophysiology of the associated human disease. Hum. Mol. Genet. *24*, 5915–5929.

Wahl-Schott, C., Baumann, L., Cuny, H., Eckert, C., Griessmeier, C., and Biel, M. (2006). Switching off calcium-dependent inactivation in L-type calcium channels by an autoinhibitory domain. Proc. Natl. Acad. Sci. U S A *103*, 15657–15662.

Wan, Q.F., Nixon, E., and Heidelberger, R. (2012). Regulation of presynaptic calcium in a mammalian synaptic terminal. J. Neurophysiol. *108*, 3059–3067.

Wasserstrom, J.A., and Aistrup, G.L. (2005). Digitalis: new actions for an old drug. Am. J. Physiol. Heart Circ. Physiol. *289*, H1781–H1793.

Wetzel, R.K., Arystarkhova, E., and Sweadner, K.J. (1999). Cellular and subcellular specification of Na,K-ATPase alpha and beta isoforms in the postnatal development of mouse retina. J. Neurosci. *19*, 9878–9889.

Wong, H.C., Zhang, Q., Beirl, A.J., Petralia, R.S., Wang, Y.X., and Kindt, K. (2019). Synaptic mitochondria regulate hair-cell synapse size and function. Elife *14*, 8, https://doi.org/10.7554/eLife48914.

You, Y., Graham, E.C., Shen, T., Yiannikas, C., Parratt, J., Gupta, V., Barton, J., Dwyer, M., Barnett, M.H., Fraser, C.L., and Klistorner, A. (2018). Progressive inner nuclear layer dysfunction in non-optic neuritis eyes in MS. Neurol. Neuroimmunol. Neuroinflamm. *5*, e427.

Yuan, Z., Cai, T., Tian, J., Ivanov, A.V., Giovannucci, D.R., and Xie, Z. (2005). Na/K-ATPase tethers phospholipase C and IP3 receptor into a calcium-regulatory complex. Mol. Biol. Cell *16*, 4034–4045.

Zenisek, D., and Matthews, G. (2000). The role of mitochondria in presynaptic calcium handling at a ribbon synapse. Neuron *25*, 229–237.

Zhang, S.H., Liu, D.X., Wang, L., Li, Y.H., Wang, Y.H., Zhang, H., Su, Z.K., Fang, W.G., Qin, X.X., Shang, D.S., et al. (2019). A CASPR1-ATP1B3 protein interaction modulates plasma membrane localization of Na^+/K^+-ATPase in brain microvascular endothelial cells. J. Biol. Chem. *294*, 6375–6386.

Zhao, W.D., Liu, D.X., Wei, J.Y., Miao, Z.W., Zhang, K., Su, Z.K., Zhang, X.W., Li, Q., Fang, W.G., Qin, X.X., et al. (2018a). Caspr1 is a host receptor for meningitis-causing Escherichia coli. Nat. Commun. *9*, 2296.

Zhao, W.D., Liu, D.X., and Chen, Y.H. (2018b). Escherichia coli hijack Caspr1 receptor to invade cerebral vascular and neuronal hosts. Microb. Cell *5*, 418–420.

Zucker, R.S. (1993). Calcium and transmitter release. J. Physiol. *87*, 25–36.

iScience, Volume *23*

Supplemental Information

Disturbed Presynaptic Ca^{2+} Signaling in Photoreceptors in the EAE Mouse Model of Multiple Sclerosis

Amrita Mukherjee, Rashmi Katiyar, Ekta Dembla, Mayur Dembla, Praveen Kumar, Anouar Belkacemi, Martin Jung, Andreas Beck, Veit Flockerzi, Karin Schwarz, and Frank Schmitz

Figure S1. Cav1.4 is less enriched at the active zone of photoreceptors in EAE mice. Related to Figure 1.

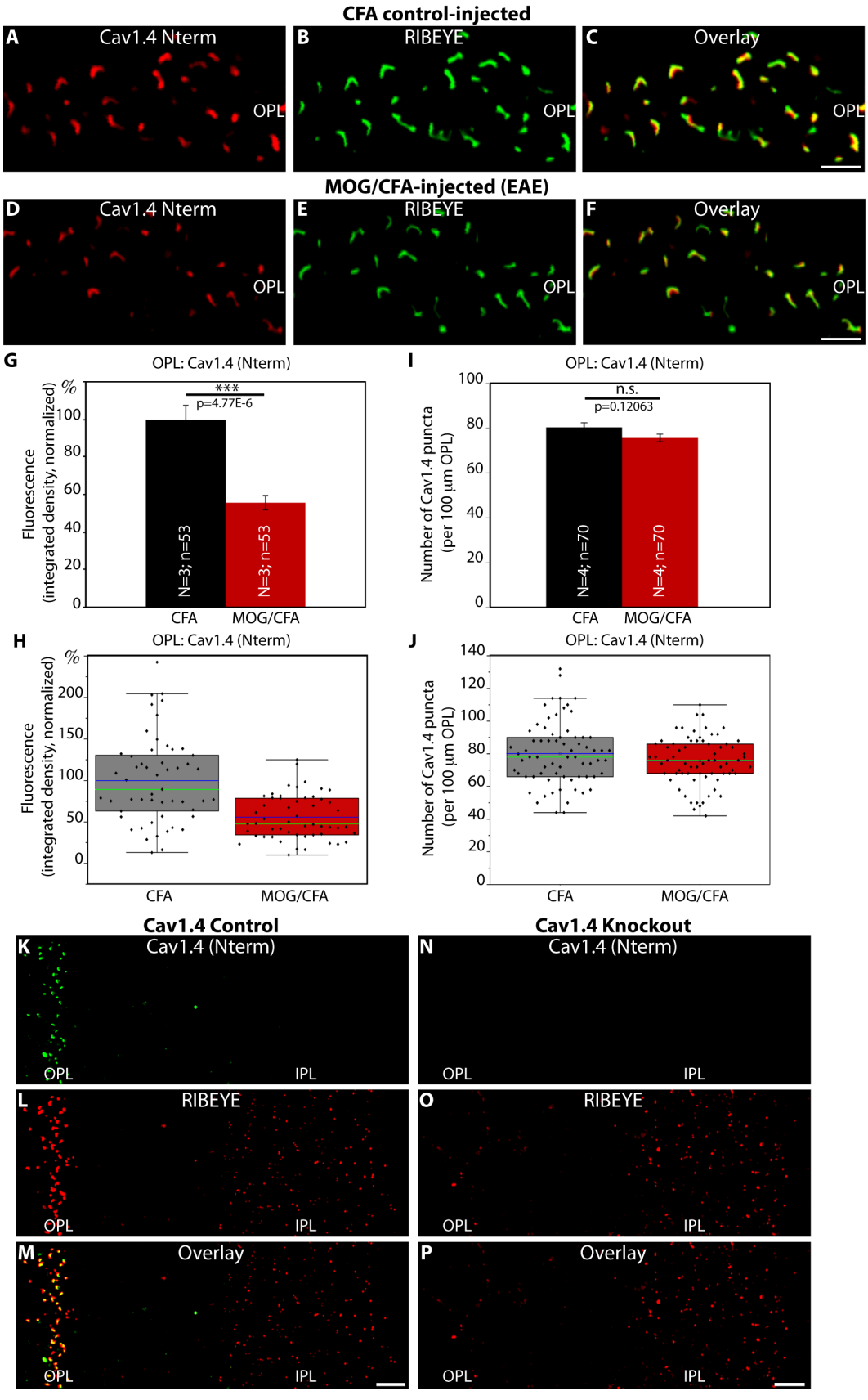

Figure S1. (A-F) Retina sections (0.5 μm in thickness) from CFA- and MOG/CFA-injected mice processed 9 days after injection. Confocal analyses of rod photoreceptor synapses in the OPL immunolabelled with rabbit polyclonal antibody against Cav1.4 (Cav1.4 Nterm) and mouse monoclonal antibody (2D9) against RIBEYE. The intensity of the Cav1.4 immunosignals is quantified as integrated density in (G, H). The number of Cav1.4 puncta is quantified in (I, J). Values are means ± S.E.M. (G, I). In the box-and-whiskers plots of the data in (H, J) mean values are labelled by blue horizontal bars; median values by green horizontal bars. Boxes represent 25 th -75 th percentiles of values and whiskers are equal to 1.5 times of the IQR. Statistical significance was determined with Mann-Whitney U test in (G, H) and with two-sample unpaired Student's t-test in (I, J). (K-P) Validation of the antibody anti-Cav1.4 Nterm. Semi-thin resin sections were immunolabelled with the indicated antibodies and analyzed by confocal microscopy. Anti-Cav1.4 Nterm was tested on control retina (K-M) and Cav1.4 knockout retina (N-P). Abbreviations: OPL, outer plexiform layer; IPL, inner plexiform layer; S.E.M., standard error of the mean; N=number of mice; n= number of images analyzed from retinal sections. Scale bars: 2 μm (C, F); 5 μm (M, P).

Figure S2. Cav1.4 is less enriched at the active zone of photoreceptors in EAE mice. Related to Figure 1.

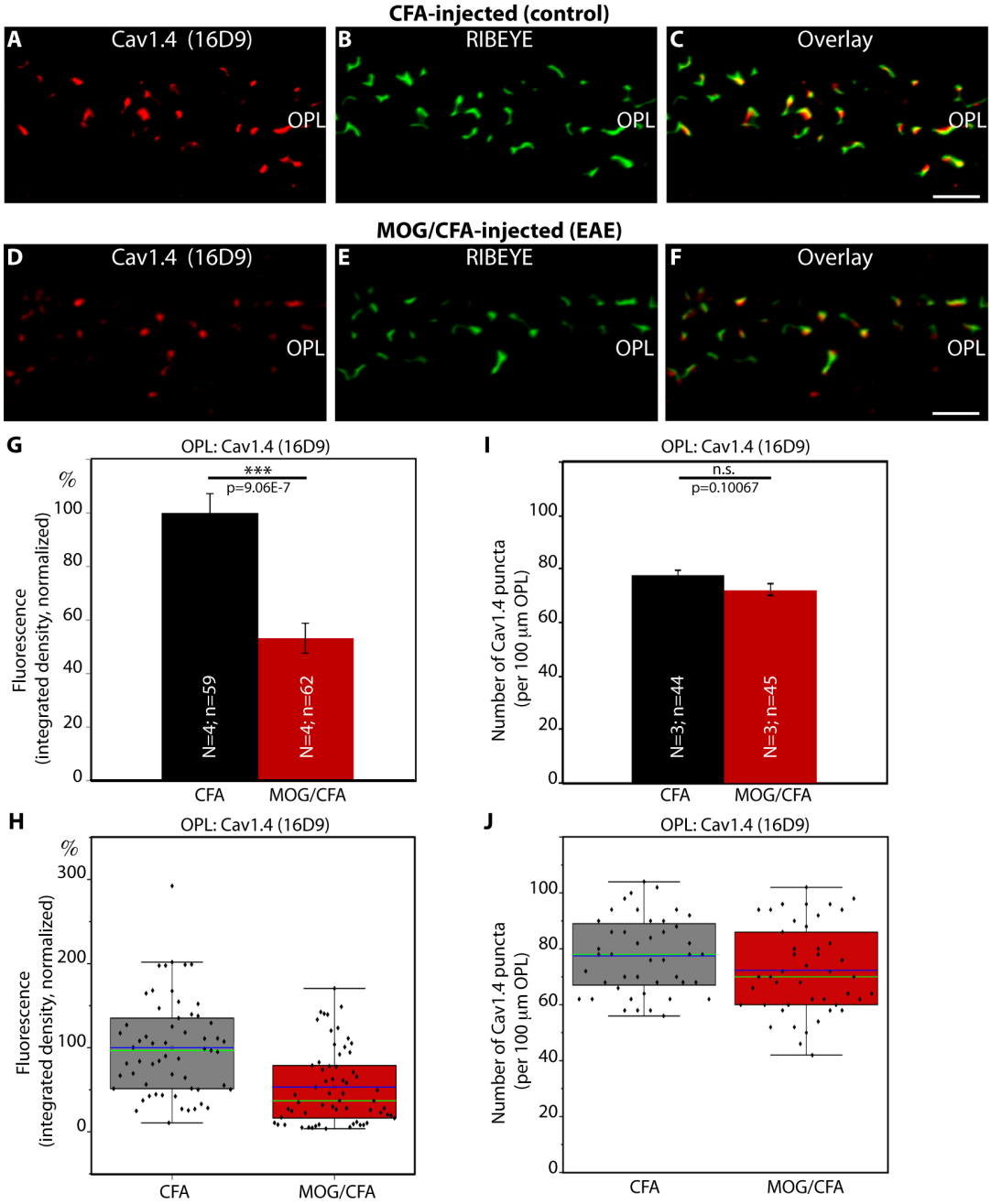

(A-F) Retina sections (0.5 µm in thickness) from CFA- and MOG/CFA-injected mice processed 9 days after injection. Confocal analyses of rod photoreceptor synapses in the OPL immunolabelled with mouse monoclonal antibody against Cav1.4 (16D9) and rabbit polyclonal antibody (U2656, Schmitz et al., 2000) against RIBEYE. The intensity of the Cav1.4 immunosignals is quantified as integrated density in (G, H). The number of Cav1.4 puncta is quantified in (I, J). Values are means ± S.E.M. (G, I). In the box-and-whiskers plots of the data in (H, J), mean values are indicated by blue horizontal bars; median values by green horizontal bars. Boxes represent 25th -75th percentiles of values and whiskers are equal to 1.5 times of the IQR. Statistical significance was determined with Mann-Whitney U test in (G, H) and with two-sample unpaired Student's t-test in (I, J). Abbreviations: OPL, outer plexiform layer; S.E.M., standard error of the mean; N=number of mice; n= number of images analyzed from retinal sections. Scale bars: 2 µm.

Figure S3. Cav1.4 is restricted to the PSD95-labelled photoreceptor terminals in the OPL. Related to Figure 1.

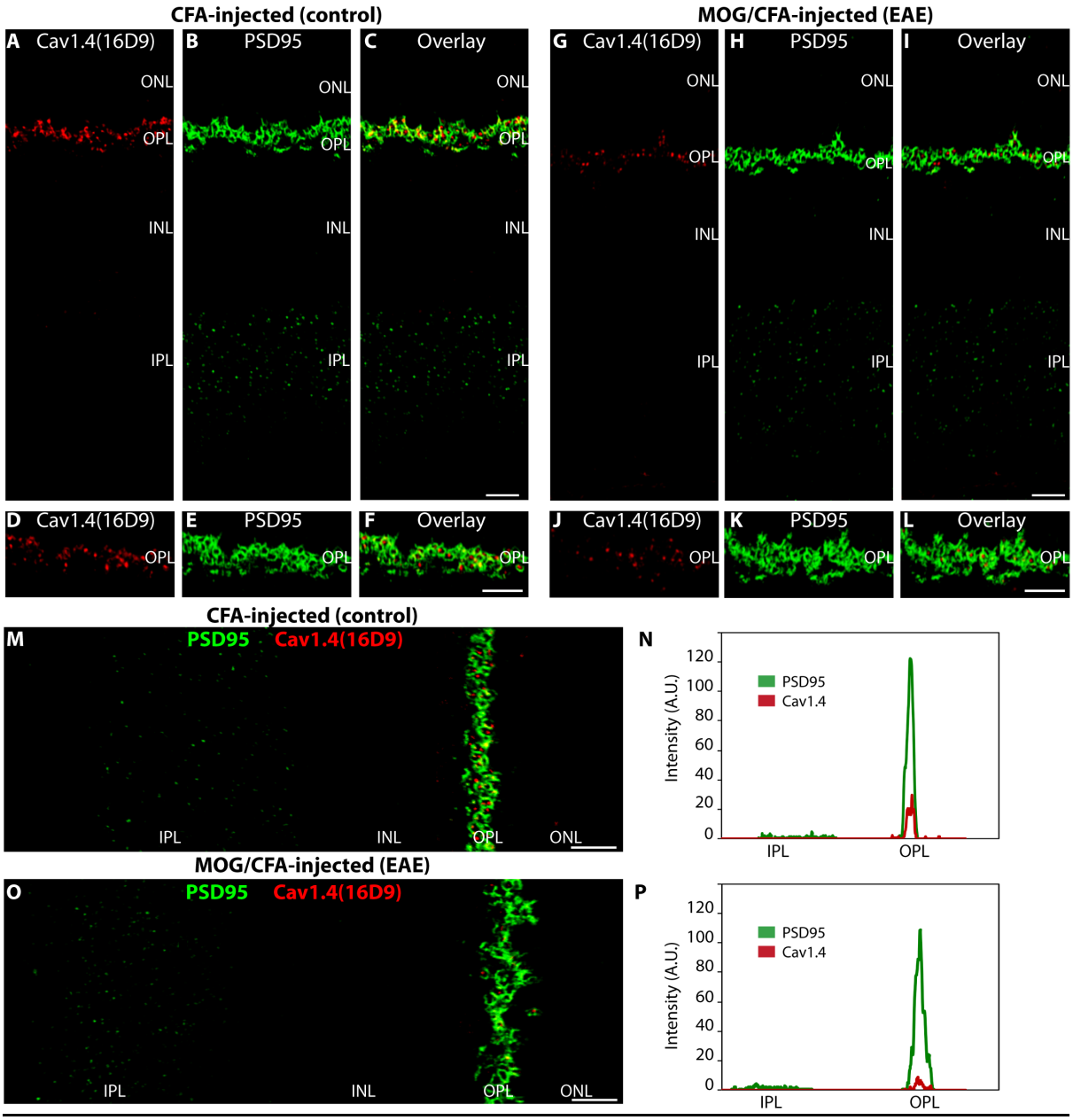

(A-L) Confocal analyses of retinal sections (0.5 µm in thickness) from CFA- and MOG/CFA-injected mice immunolabelled with mouse monoclonal antibody against Cav1.4 (16D9) and rabbit polyclonal antibody against PSD95 processed 9 days after injection. (A-C; G-I) provide low magnification overviews; (D-F; J-L) provide high magnification views of the immunolabelled OPL. In M-P, the sections were subjected to line scans to further analyze the relation of the location of the immunosignals. In the OPL, all Cav1.4 immunosignals were contained within the PSD95-immunolabelled presynaptic terminals (N-P). Abbreviations: ONL, outer nuclear layer; OPL, outer plexiform layer; INL, inner nuclear layer; IPL, inner plexiform layer. Scale bars: 5 µm (C, F, I, L).

Figure S4. Cavβ2 is less enriched at the active zone of photoreceptors in EAE mice. Related to Figure 3.

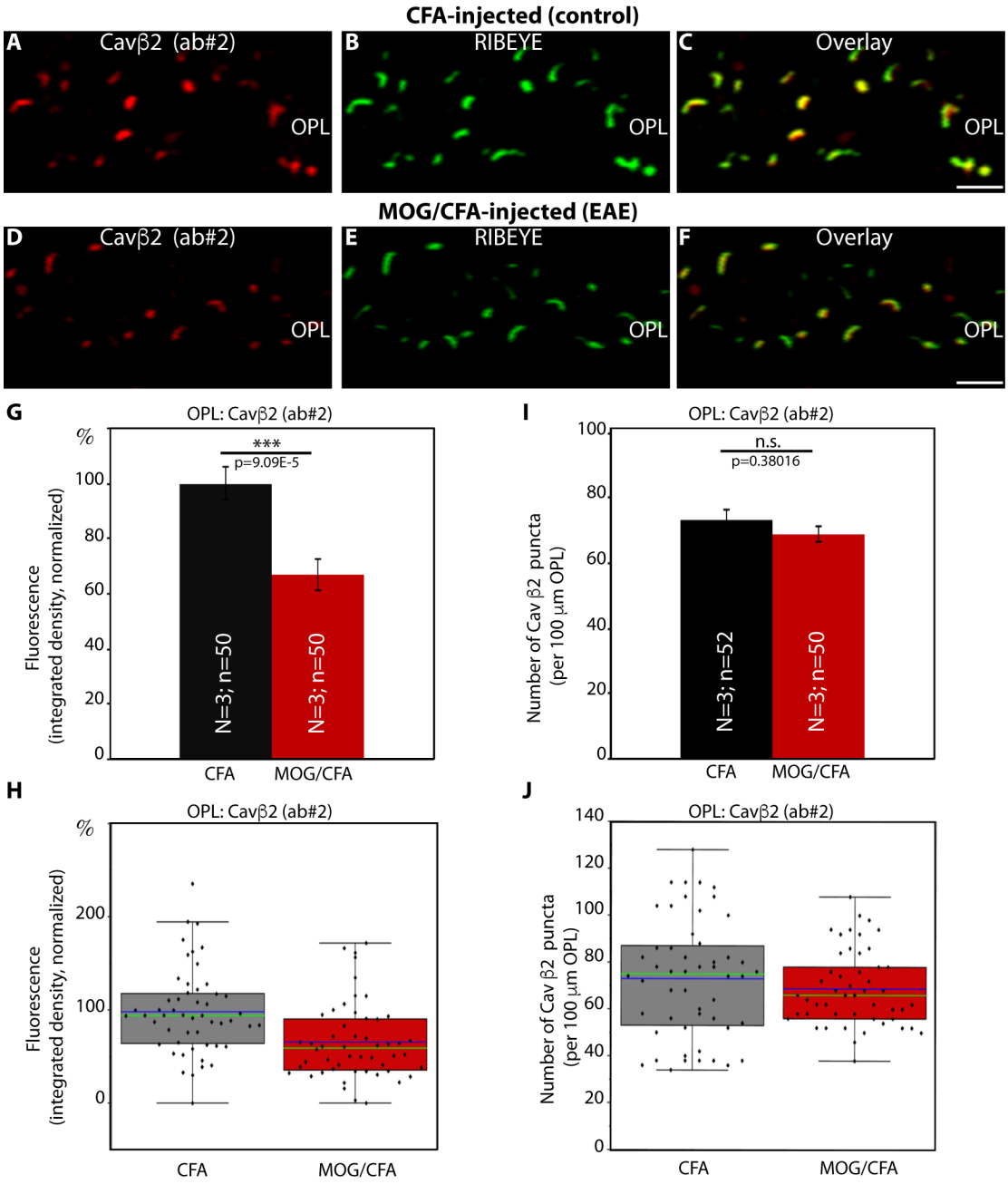

(A-F) Retina sections (0.5 µm in thickness) from CFA- and MOG/CFA-injected mice processed 9 days after injection. Confocal analyses of rod photoreceptor synapses in the OPL immunolabelled with rabbit polyclonal antibody against Cavβ2 (ab#2) and mouse monoclonal antibody (2D9) against RIBEYE. The intensity of the Cavβ2 immunosignals is quantified as integrated density in (G, H). The number of Cavβ2 puncta is quantified in (I, J). Values are means ± S.E.M. (G, I). In the box-and-whiskers plots of the data in (H, J) mean values are labelled by blue horizontal bars; median values by green horizontal bars. Boxes represent 25th -75th percentiles of values and whiskers are equal to 1.5 times of the IQR. Statistical significance was determined with Mann-Whitney U test. Abbreviations: OPL, outer plexiform layer; S.E.M., standard error of the mean; N=number of mice; n= number of images analyzed from retinal sections. Scale bars: 2 µm.

Figure S5. Validation of mouse monoclonal RIM2 antibody 4C6. Related to Figure 5.

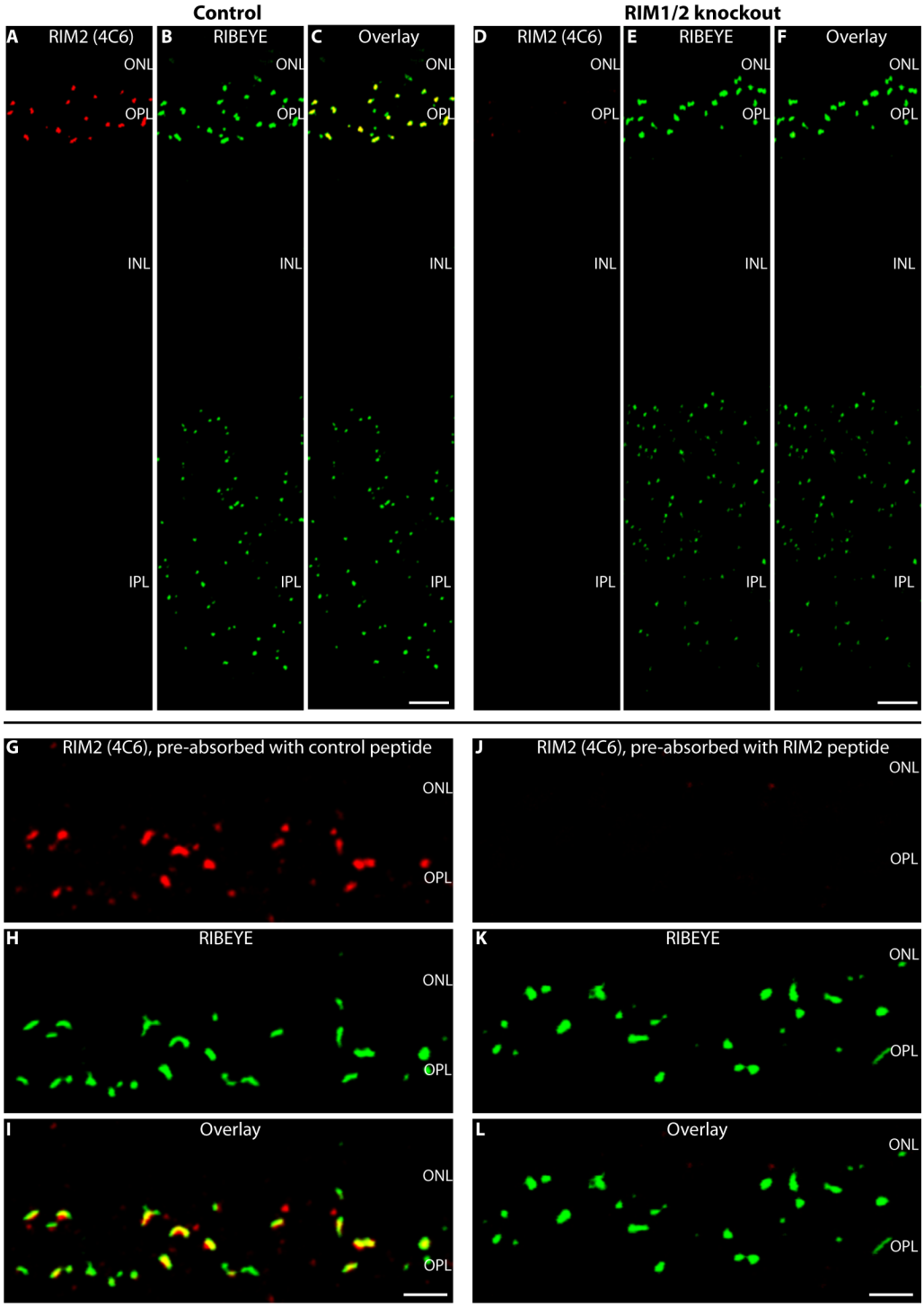

(A-F) Characterization of the RIM2 mouse monoclonal antibody 4C6 on wildtype control retina (A-C) and photoreceptor-specific RIM1/2 knockout retina (D-F). Semi-thin (0.5 µm-thin) resin sections of the retina were double-immunolabelled with mouse monoclonal RIM2 antibody 4C6 and rabbit polyclonal antibody against RIBEYE (U2656, Schmitz et al., 2000). In the wildtype control, we found a strong 4C6 immunolabelling in the OPL (A), similarly as previously described with another RIM2 monoclonal antibody (4F7; Dembla et al., 2020). The RIM2 immunosignal in the OPL is completely absent in the photoreceptor-specific RIM1/2 knockout (D). The RIBEYE immunosignals were

qualitatively unaffected in wildtype and knockout tissue (B, C, E, F). (G-L) Pre-absorption controls of RIM2 signals performed on wildtype retina sections. The 4C6 antibody was either pre-absorbed with an unrelated control peptide (G-I) or the RIM2 peptide against which the antibody was raised (J-L). Blocking the 4C6 antibody with RIM2-specific peptide completely abolished immunosignals in the OPL (J) while pre-absorption with an unrelated control peptide had no effect on immunosignals (G). RIBEYE immunosignals were unaffected by blocking with either peptide (H, I; K, L). Abbreviations: ONL, outer nuclear layer; OPL, outer plexiform layer; INL, inner nuclear layer; IPL, inner plexiform layer. Scale bars: 5μm (C, F); 2μm (I, L).

Figure S6. RIM2 is less enriched at the active zones of photoreceptor synapses in EAE mice. Related to Figure 5.

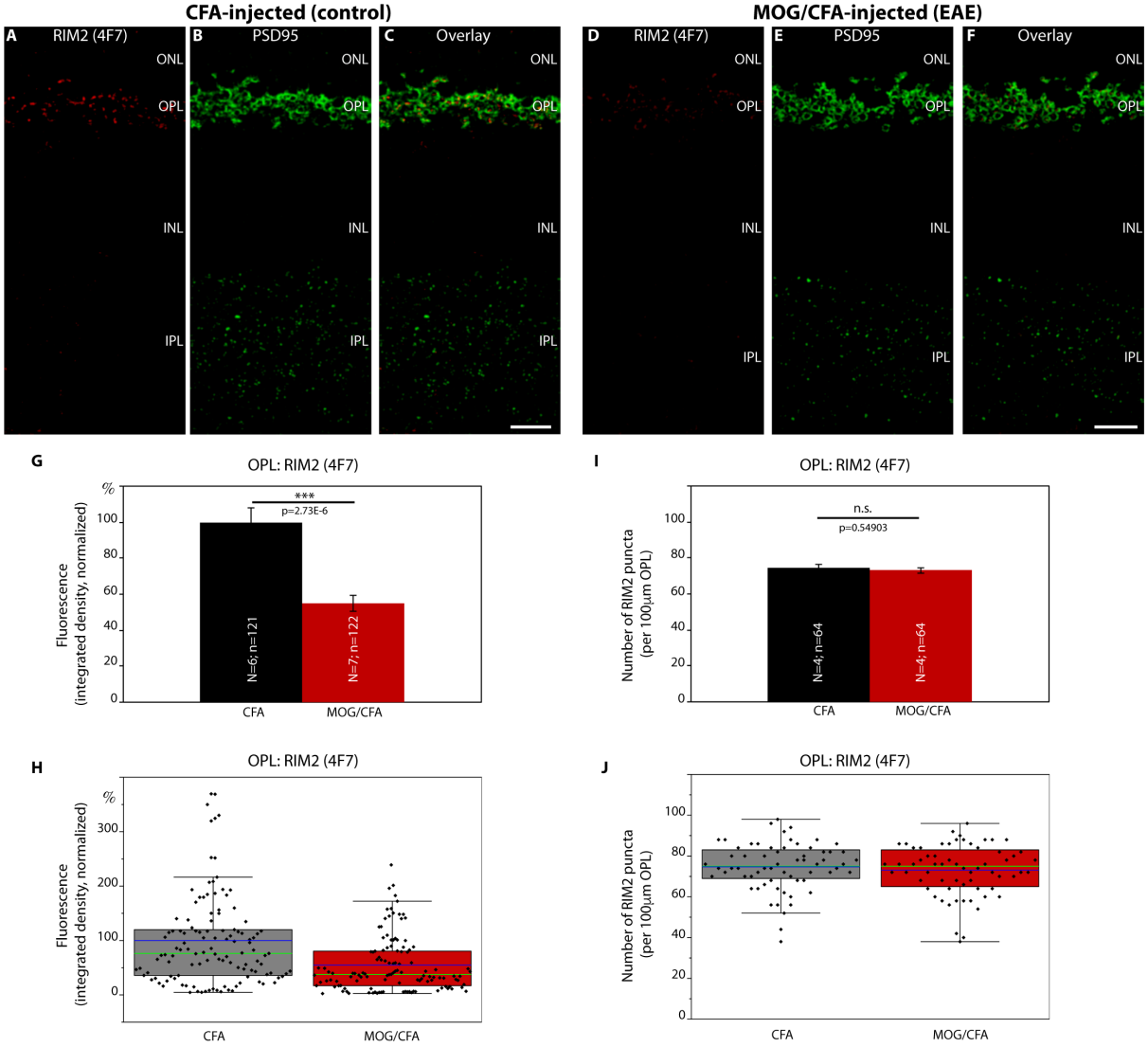

(A-F) Retinal sections (0.5 µm in thickness) from CFA- and MOG/CFA-injected mice processed 9 days after injection. Confocal analyses of rod photoreceptor synapses in the OPL immunolabelled with mouse monoclonal antibody against RIM2 (4F7) and rabbit polyclonal antibody against RIBEYE (U2656, Schmitz et al., 2000). The intensity of the RIM2 immunosignals were quantified as integrated density in (G, H). The number of RIM2 puncta are quantified in (I, J). Values are means ± S.E.M. (G, I). In the box-and-whiskers plots of the data in (H, J), mean values are indicated by blue horizontal bars; median values by green horizontal bars. Boxes represent 25th-75th percentiles of values and whiskers are equal to 1.5 times of the IQR. Statistical significance was determined with Mann-Whitney U-test. Abbreviations: ONL, outer nuclear layer; OPL, outer plexiform layer; INL, inner nuclear layer; IPL, inner plexiform layer; S.E.M., standard error of the mean; N=number of mice; n= number of images analyzed from the retinal sections. Scale bars: 5 µm.

Figure S7. Fura2 imaging of photoreceptor synapses in retinal slices. Related to Figure 6.

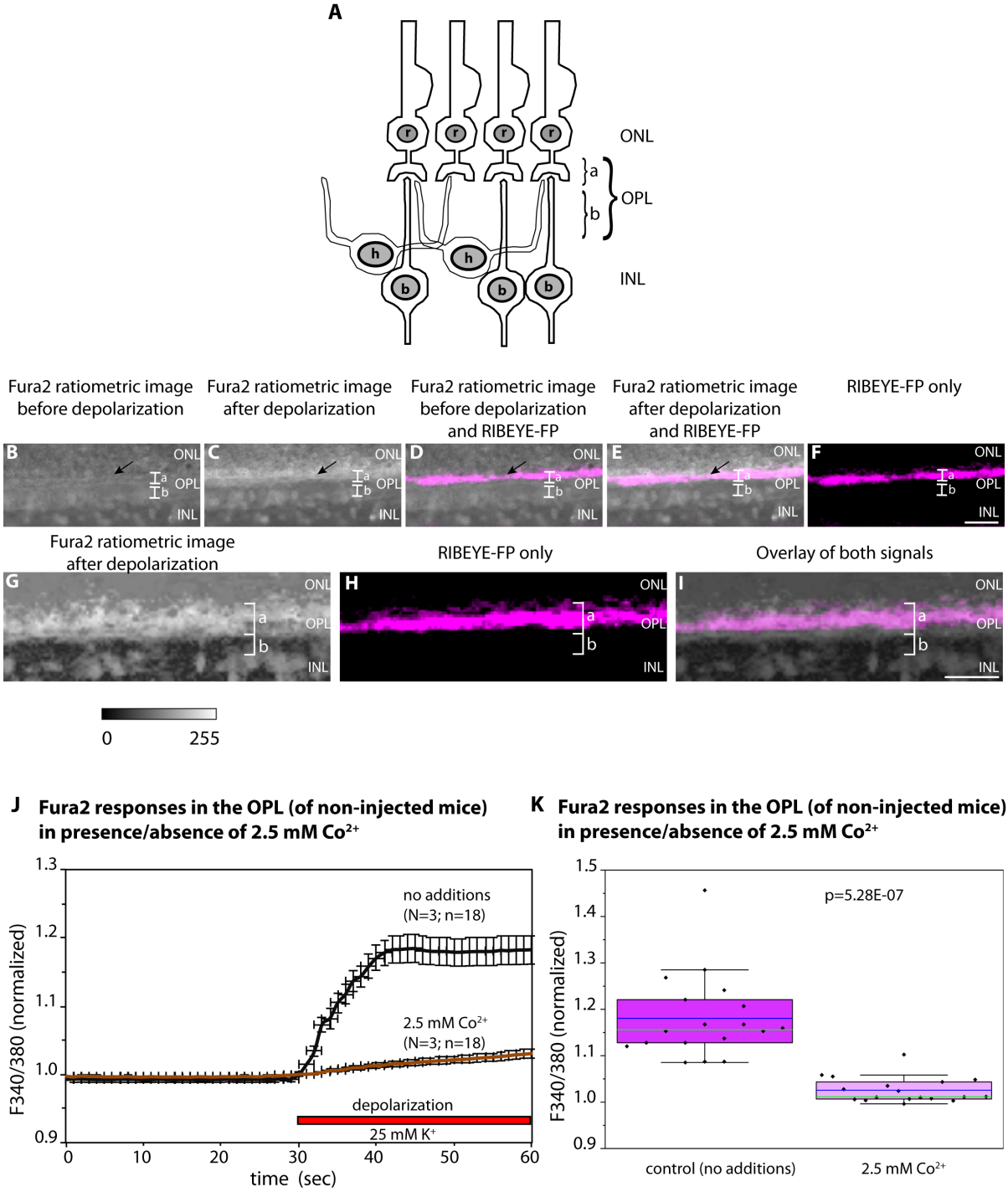

(A) Schematic drawing of the outer plexiform layer (OPL). In the OPL, rod photoreceptor (r) terminals contact the dendritic processes of bipolar (b) and horizontal (h) cells. In the outer portion of the OPL, close to the ONL, the synapses are located (sub-layer a) whereas a second sub-layer of the OPL (sub-layer b) contains the neuropil of dendritic and axonal processes of bipolar and horizontal cells as well as processes from Müller glia cells (not shown). These sublayers (sub-layers a, b) are also indicated in B-I. (B, C), ratiometric F340 / F380 micrograph from a Fura2-loaded retinal slice of a RIBEYE-FP mouse (Okawa et al., 2019) showing the OPL before (B) and after (C) depolarization in 200 µm-thick retinal slices. The strongest high K^+ depolarization-induced Fura2 responses were

observed in the synaptic sub-layer of the OPL (sub-layer a, arrow). (D, E, F) Similarly, these depolarization-induced Fura2 peaks in the OPL largely co-localized with the endogenous fluorescence of synaptic ribbons of the RIBEYE-FP mice in which the synaptic ribbons are tagged with a fluorescent protein thus indicating the localization of the presynaptic photoreceptor terminal *in-situ*. Please note that individual ribbons cannot be resolved in the retinal slices due to the thickness of the slices (200μm). A similar image as shown in (B-F) is demonstrated in (G-I) at a higher magnification. The heatmap indicates the relative intensity of the signals (the brighter the color, the stronger the signal. J) High K^+ depolarization-induced Fura2 responses at the ROI made in the OPL of mice retinal slices could be blocked by the addition of Co^{2+} that blocks Ca^{2+} entry through Cav-channels demonstrating that the observed Fura-2 signals were indeed dependent upon Ca^{2+}-influx through voltage-gated Cav-channels. Fura2 values of control- and Co^{2+}-treated slices in the depolarization phase (50-60sec) were significantly different from each other (p=5.28E-07; Mann-Whitney U test). In the box-and-whiskers plots of the individual data in (K), mean values are indicated by blue horizontal bars; median values by green horizontal bars. Boxes represent 25^{th}-75^{th} percentiles of values and whiskers are equal to 1.5 times of the IQR. Abbreviations: ONL, outer nuclear layer; OPL, outer plexiform layer; INL, inner nuclear layer. Scale bars: 100 μm.

Figure S8. Reduced expression of CASPR1 and Na^+K^+-ATPase in photoreceptor synapses in the OPL of EAE mice. Related to Figure 8.

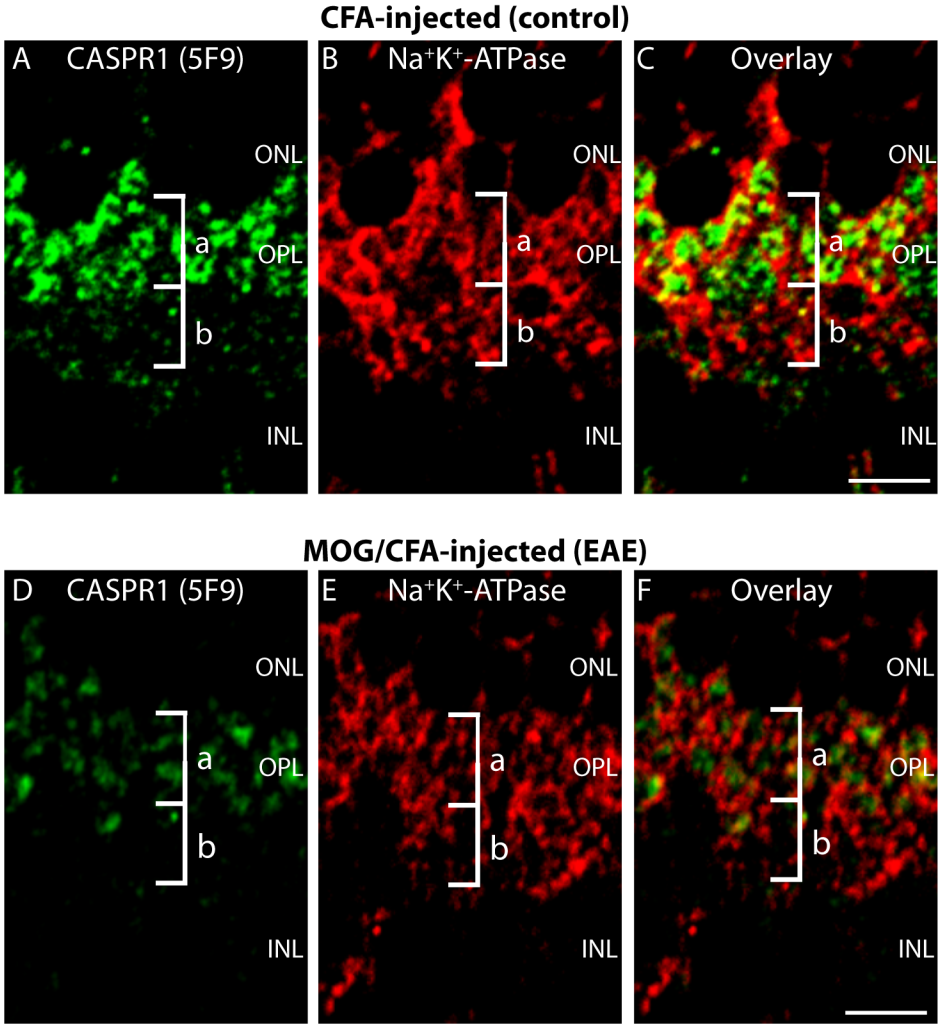

(A-F) Retina sections (0.5 µm in thickness) from CFA- and MOG/CFA-injected mice processed 9 days after injection. Confocal analyses of rod photoreceptor synapses in the OPL immunolabelled with mouse monoclonal antibody against CASPR1 (5F9) and mouse monoclonal antibody against Na^+K^+ATPase using the Fab method. Both Na^+K^+ATPase- and CASPR1 immunosignals were found to be decreased in the OPL of MOG/CFA-injected mice (D-F) in comparison to CFA-injected control mice (A-C). For quantification of the Na^+K^+ATPase immunosignal intensity, see Fig. 8. CASPR1 signal intensity in the OPL of MOG/CFA and CFA-injected mice was already previously quantified (Dembla et al., 2018). Abbreviations: ONL, outer nuclear layer; OPL, outer plexiform layer; INL, inner nuclear layer. Brackets indicate the synaptic sub-layer of the OPL (sub-layer a) and the extra-synaptic, neuropil layer of the OPL (sub-layer b). Scale bars: 5 µm.

Figure S9. Expression of pan-PMCA in the retina of EAE and control mice. Related to Figure 9.

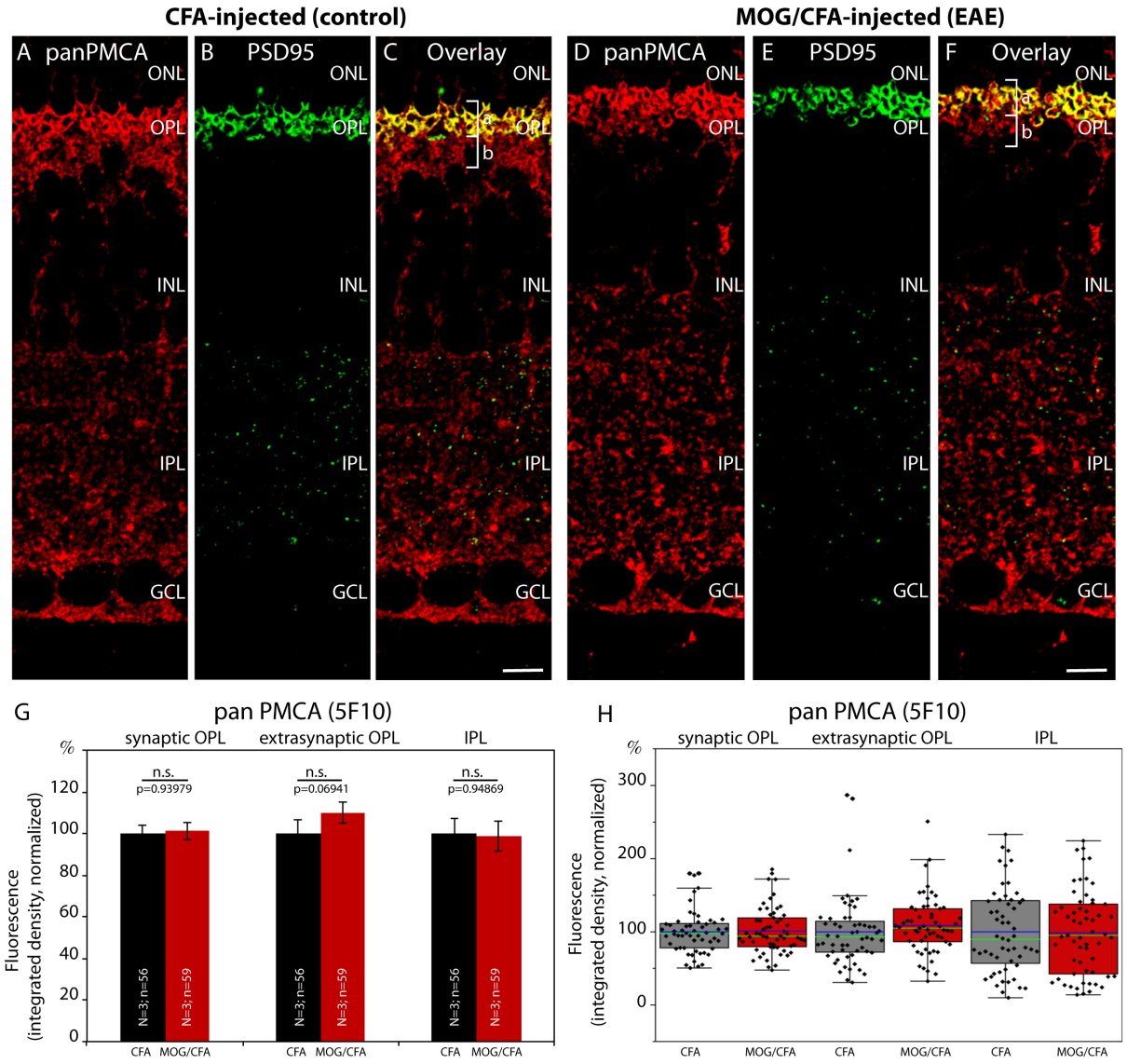

(A-F) Retinal sections (0.5 μm in thickness) from CFA- and MOG/CFA-injected mice processed 9 days after injection. Confocal analyses of rod photoreceptor synapses in the OPL immunolabelled with mouse monoclonal antibody against panPMCA (5F10) and rabbit polyclonal antibody against PSD95. The intensity of the panPMCA (5F10) immunosignals were quantified as integrated density in (G, H). Values are means ± S.E.M. (G). In the box-and-whiskers plots of the data in (H), mean values are indicated by blue horizontal bars; median values by green horizontal bars. Boxes represent 25th-75th percentiles of values and whiskers are equal to 1.5 times of the IQR. Statistical significance was determined with Mann-Whitney U test. Abbreviations: ONL, outer nuclear layer; OPL, outer plexiform layer; INL, inner nuclear layer; IPL, inner plexiform layer; GCL, ganglion cell layer; bracket a, synaptic sub-layer of the OPL; bracket b, extra-synaptic, neuropil sub-layer of the OPL; S.E.M., standard error of the mean; N=number of mice; n= number of images analyzed from the retinal sections. Scale bars: 5 μm.

Figure S10. Decreased expression of PMCA2 in photoreceptor synapses of EAE mice. Related to Figure 10.

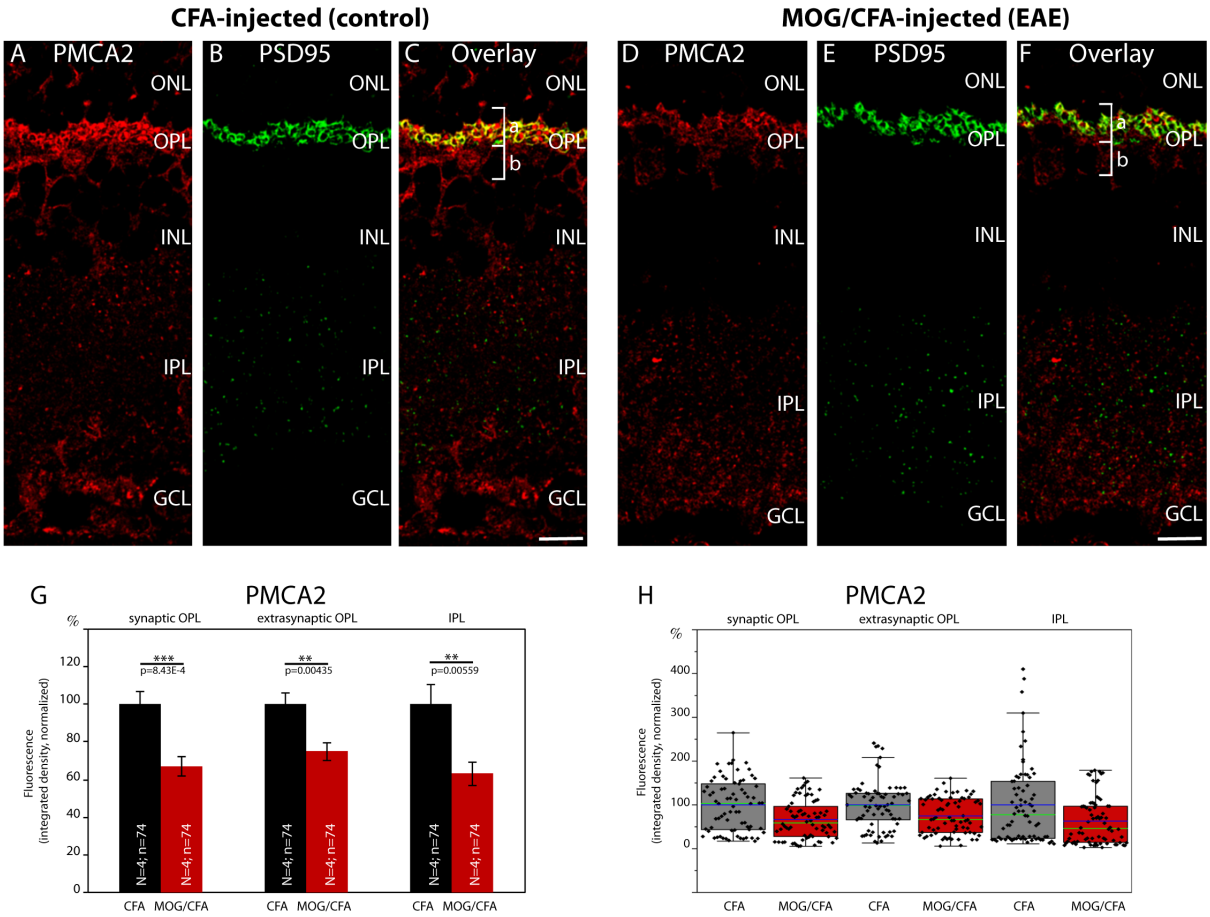

(A-F) Retinal sections (0.5 μm in thickness) from CFA- and MOG/CFA-injected mice processed 9 days after injection. Confocal analyses of rod photoreceptor synapses in the OPL immunolabelled with rabbit polyclonal antibody against PMCA2 and rabbit polyclonal antibody against PSD95 using the Fab method**.** The intensity of the PMCA2 immunosignals were quantified as integrated density in (G, H). Values are means ± S.E.M. (G). In the box-and-whiskers plots of the data in (H), mean values are indicated by blue horizontal bars; median values by green horizontal bars. Boxes represent 25th-75th percentiles of values and whiskers are equal to 1.5 times of the IQR. Statistical significance was determined with Mann-Whitney U test. Abbreviations: ONL, outer nuclear layer; OPL, outer plexiform layer; INL, inner nuclear layer; IPL, inner plexiform layer; GCL, ganglion cell layer; bracket a, synaptic sub-layer of the OPL; bracket b, extra-synaptic, neuropil sub-layer of the OPL; S.E.M., standard error of the mean; N=number of mice; n= number of images analyzed from the retinal sections. Scale bars: 5 μm.

Figure S11. Quantification of Western blot bands of the indicated proteins. Related to Figure 11.

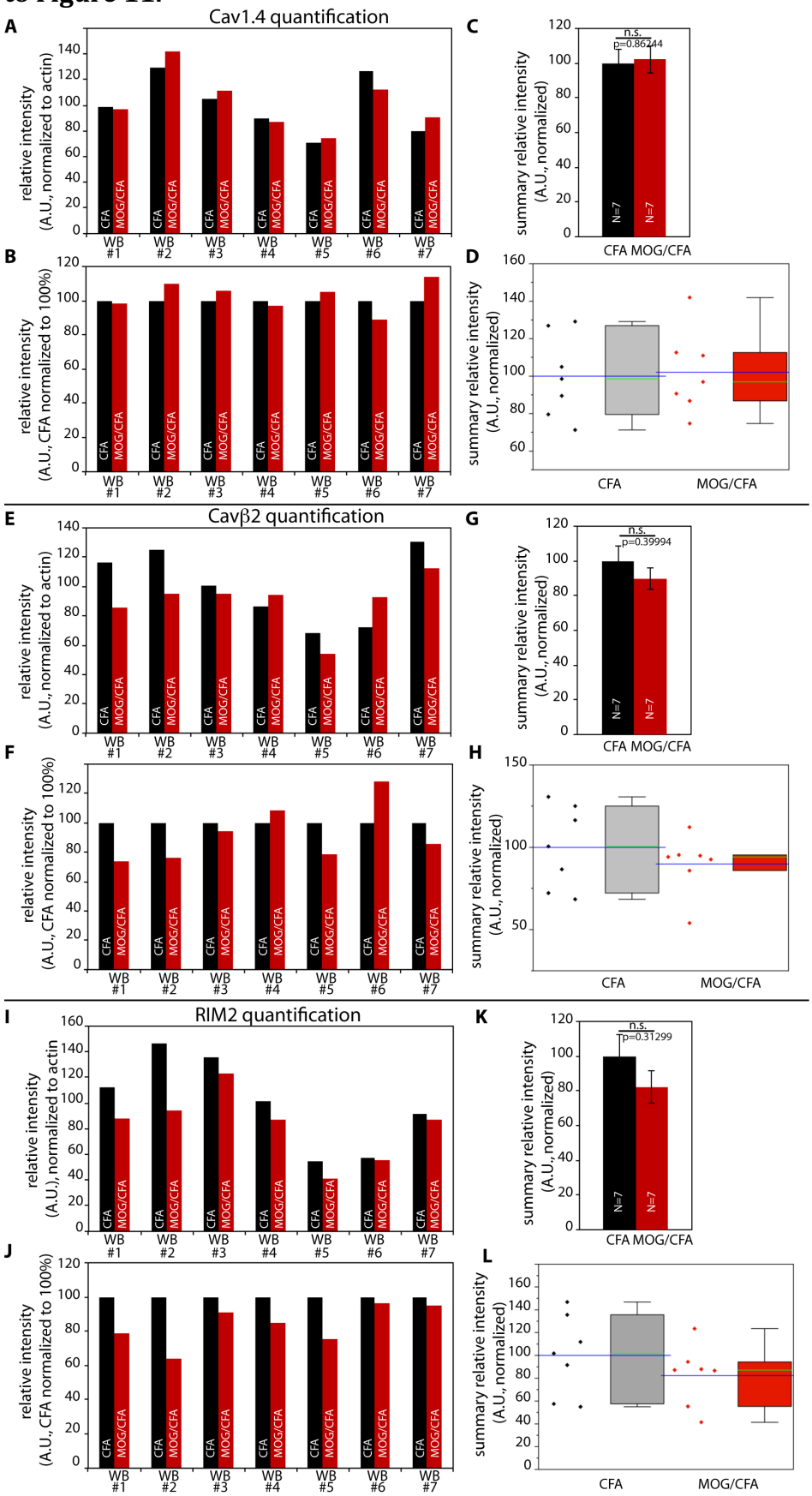

Figure S11. The protein bands indicated by boxes in the representative WB experiments shown in Fig. 11 were quantified as described in Materials and Methods. The intensity of each of the protein bands (Cav1.4, Cavβ2, RIM2, see Fig 11) was normalized to the actin signal of the same lane to compensate for potential loading differences between individual lanes. The results of all seven individual blots performed for quantification are shown in A, B, E, F, I and J. In B, F, J, individual CFA values were set to 100% to better evaluate the relative changes in MOG/CFA samples in comparison to CFA values. (C, G, K) Bar graphs show the means ± S.E.M. from the values shown in (A, E, I). The box-and-whiskers plots in (D, H, L) represent the distribution of the individual data from (A, E, I). Mean values are indicated by blue horizontal bars; median values by green horizontal bars (D, H, L). Boxes represent 25^{th}-75^{th} percentiles of values and whiskers are equal to 1.5 times of the IQR. Statistical significance was determined with two-sample unpaired Student's t-test. Abbreviations: A.U., arbitrary units; S.E.M., standard error of the mean.

Figure S12. Quantification of Western blot bands of the indicated proteins. Related to Figure 11.

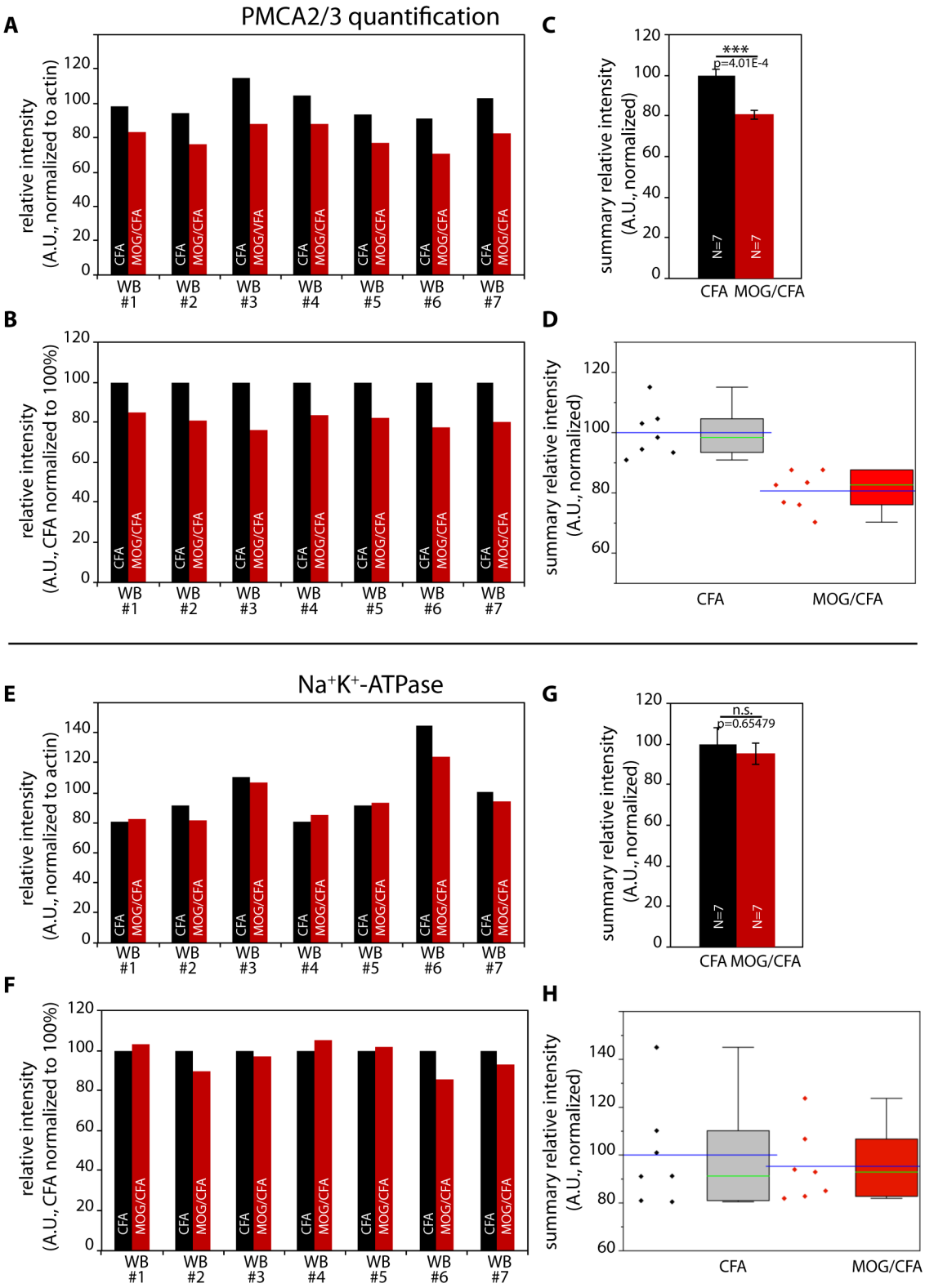

The protein bands indicated by boxes in the representative WB experiments shown in Fig. 11 were quantified as described in Materials and Methods. The intensity of each of the protein bands (PMCA2/3; Na^+K^+-ATPase, see Fig. 10) was normalized to the actin signal of the same lane to compensate for potential loading differences between

individual lanes. The results of all seven individual blots performed for quantification are shown in A, B, E, F. In B, F, individual CFA values were set to 100% to better evaluate the relative changes in MOG/CFA samples in comparison to CFA values. (C, G) Bar graphs represent the means ± S.E.M from the values shown in (A, E). The box-and-whiskers plots in (D, H) represent the distribution of the individual data shown in (A, E). Mean values are indicated by blue horizontal bars; median values by green horizontal bars. Boxes represent 25^{th}-75^{th} percentiles of values and whiskers are equal to 1.5 times of the IQR. Statistical significance was determined with two-sample unpaired Student's t-test. Abbreviations: A.U., arbitrary units; S.E.M., standard error of the mean.

Transparent Methods

Animals

Experiments were carried out using 10-12 weeks old female C57BL/6J mice (body weight between 20g-25g). Mice were subjected to standard light/dark cycles and were provided with water and standard food *ad libitum*. All animal procedures were reviewed and approved by the local animal authorities and performed according to the German Animal Protection Law. Cav1.4 knockout tissue was kindly provided by Prof. Dr. M. Biel (University of Munich) (Specht et al., 2009; Michalakis et al., 2014). RIBEYE-FP transgenic mice with fluorescent synaptic ribbons were previously generated and used as described (Okawa et al., 2019).

Antibodies

Primary antibodies:

Antibody	Reference	Dilution
Anti-RIBEYE(B), rabbit polyclonal (U2656)	Schmitz et al., 2000	1:1,500 (IF)
Anti-RIBEYE(B), mouse monoclonal (2D9)	Dembla et al., 2018	1:1,000 (IF)
Anti-Cav1.4 Cterm, rabbit polyclonal	Dembla et al., 2020	1:800 (IF)
Anti-Cav1.4 Nterm, rabbit polyclonal, raised against aa1-aa121 of mouse Cav1.4	this study	1:800 (IF); 1:1,000(WB)
Anti-Cav1.4, mouse monoclonal (16D9), raised against aa1-aa121 of mouse Cav1.4	Dembla et al., 2020	1:20 (IF)
Anti-Cavβ2, rabbit polyclonal (#1), raised against aa507-aa525 of mouse Cavβ2	Link et al., 2009; Meissner et al., 2011	1:100 (IF)
Anti-Cavβ2, rabbit polyclonal (#2), raised against aa593-aa611 of mouse Cavβ2	Link et al., 2009; Katiyar et al., 2015	1:800 (IF); 1:1,000(WB)
Anti-RIM2, mouse monoclonal (4C6) (IgG2A), raised against aa544-aa564 of RIM2	this study	1:20 (IF)
Anti-RIM2, mouse monoclonal (4F7), raised against aa544-aa564 of RIM2	Dembla et al., 2020	1:20 (IF)
Anti-RIM2, rabbit polyclonal	Synaptic Systems (140-303); Grabner et al., 2015	1:500 (WB)
Anti-Na^+/K^+-ATPase α–subunit, mouse monoclonal antibody (clone H-3)	Santa Cruz (sc-48345); Shi et al., 2019	1:100 (IF); 1:500 (WB)
Anti-CASPR1, mouse monoclonal antibody (5F9)	Dembla et al., 2018	1:50 (IF)
Anti-PSD95, rabbit polyclonal antibody (L667)	Irie et al., 1997	1:800 (IF)
Anti-PMCA1, rabbit polyclonal	ThermoFisher (PA1-914), Hegedüs et al., 2017	1:100 (IF)
Anti-panPMCA, mouse monoclonal (5F10)	Invitrogen (MA3-914) Križaj et al., 2002	1:500 (IF)
Anti-PMCA2, rabbit polyclonal	ThermoFisher (PA1-915) Jeong et al., 2016	1:100 (IF)

Anti-PMCA2/3, mouse monoclonal (clone C-3), raised against aa 83-194 of human PMCA2	Santa Cruz (sc-398013) Schmidt et al., 2017	1:100 (IF) 1:200 (WB)
Anti-Actin, mouse monoclonal (clone C4)	Millipore (MAB1501) Eich et al., 2017	1:2,000(WB)

Secondary antibodies:

Antibody	Source	Dilution
Chicken anti-mouse Alexa488	Invitrogen Molecular Probes, A-21200	1:1,000 (IF)
Donkey anti-rabbit Alexa568	Invitrogen, Molecular Probes, A-10042	1:1,000 (IF)
Chicken anti-rabbit Alexa488	Invitrogen, Molecular Probes, A-21441	1:1,000 (IF)
Donkey anti-mouse Alexa568	Invitrogen, Molecular Probes, A-10037	1:1,000 (IF)
Goat anti-rabbit Alexa647	Invitrogen, Molecular Probes, A-21245	1:1,000 (IF)
Goat anti-rabbit peroxidase-conjugated (POX)	Sigma, A-3673	1:3,000 (WB)
Goat anti-mouse POX	Sigma, A-6154	1:3,000(WB)
Rabbit anti-mouse IgG (H&L) Fab fragment	Rockland Antibodies, 810-4102	1:50(IF)
Goat anti-rabbit IgG (H&L) Fab fragment	Rockland Antibodies, 811-1102	1:50(IF)

Solutions

Resting solution (RS): 132 mM NaCl, 3 mM KCl, 1 mM $MgCl_2x6H_2O$, 2 mM $CaCl_2$, 10 mM HEPES, pH 7.4, 10 mM sodium pyruvate, 10 mM glucose (osmolality 305-315 mOsmol/kg).

Low Ca^{2+} solution (LCS): 132 mM NaCl, 3 mM KCl, 1 mM $MgCl_2x6H_2O$, 0.5 mM $CaCl_2$, 10 mM HEPES, pH 7.4, 10 mM sodium pyruvate, 10 mM glucose (osmolality 305-315 mOsmol/kg).

Depolarization solution: 85 mM NaCl, 50 mM KCl, 1 mM $MgCl_2x6H_2O$, 2 mM $CaCl_2$, 10 mM HEPES, pH 7.4, 10 mM sodium pyruvate, 10 mM glucose (osmolality 305-315 mOsmol/kg).

Methods

Induction of EAE

For induction of experimental autoimmune encephalomyelitis (EAE), female C57BL/6J mice older than 10 weeks (body weight between 20g-25g) were selected (Dembla et al., 2018). Mice were injected subcutaneously into the axilla and groin with encephalitogenic MOG_{35-55} peptide of mouse myelin oligodendrocyte glycoprotein (MEVGWYRSPFSRVVHLYRNGK) contained in a ready-to-go suspension from Hooke laboratories (MOG_{35-55}/CFA Emulsion PTX, Hooke Laboratories, Lawrence. MA, USA; #EK-2110) or with self-made suspensions (Dembla et al., 2018)). To increase blood-brain barrier permeability, 200 ng of pertussis toxin (PTX) from *B. pertussis* in a volume of 100 µl sterile glycerol buffer was injected intraperitoneally on the same day (day 0, 1-2hr after MOG_{35-55} peptide injection) and also on the subsequent day (day1, 16-20 hr after first PTX injection). Controls were injected with CFA only, i.e. without MOG_{35-55} peptide (Hooke Laboratories, Lawrence. MA, USA; CFA control kit # CK-2110). All other treatments for the control injections, e.g, pertussis toxin injection were done identically as described for

MOG/CFA injection. For the Fura2 analyses, all mice were injected with commercial, pre-made suspensions (Hooke Laboratory, see above). Subsequent analyses were done blindly, i.e. the experimenter was not aware whether a mouse was MOG/CFA-injected or CFA (control)-injected.

Immunolabelling of resin sections of the retina

Retina samples were collected within 5 min post-mortem and processed for immunolabelling (Wahl et al., 2013, 2016; Dembla et al., 2014, 2018): First, the tissue was flash-frozen in liquid nitrogen-cooled isopentane. The subsequent lyophilization of the tissue was performed at a vacuum of $\approx 10^{-7}$ mbar. The vacuum was generated with a TCP270 turbomolecular pump (Arthur-Pfeiffer-Vacuumtechnik, Wetzlar/Aßlar, Germany) controlled by a PKG020 Pirani-gold cathode gauge control unit and an oil diffusion pump as pre-pumping unit (type DUO 004B; Arthur-Pfeiffer-Vacuumtechnik, Wetzlar/Aßlar, Germany). During this process, the tissue was continuously cooled by liquid nitrogen. Samples were lyophilized in liquid nitrogen for ≈24hrs. Afterwards, samples were equilibrated to room temperature, infiltrated with Epon resin and degassed for 24 hrs to ensure complete penetration with Epon. Curing of the resin-embedded samples was done at 60°C for ≈24 hrs. Immunolabelling was performed on 0.5 µm-thin resin sections for confocal microscopy (Wahl et al., 2013, 2016; Dembla et al., 2014, 2018). Prior to immunolabelling resin was removed. For this purpose, tissue sections were incubated in the following solutions: sodium methanolate (30% solution in methanol; Merck/Sigma-Aldrich) (10 min); 1:1 mixture of xylol / methanol (10 min); acetone (2x10 min), H_2O (10 min) and PBS (10 min). After resin removal, sections were incubated with specified primary antibodies at the indicated dilutions (4°C overnight). For double-immunolabelling analyses, incubation with the two primary antibodies was performed simultaneously. After several washes with PBS to remove unbound primary antibodies, bound primary antibodies were detected by incubation with corresponding secondary antibodies conjugated to the indicated fluorophores (1:1,000 dilution; 1 hr at room temperature). Immunolabelled sections were embedded in N-propyl gallate antifade, as described (Wahl et al., 2013, 2016; Dembla et al., 2014, 2018). Negative controls were done by omitting primary antibodies, by using irrelevant primary antibodies and by using incubations of knockout sections, as indicated in the respective experiments. Pre-absorption experiments were performed by adding the specified peptides (final concentration of 1 mg / mL) to the antibodies in their final working concentrations. The tubes with the antibody mixtures were incubated overnight at 4°C with an overhead rotator and used for immunolabelling experiments on the next day.

In order to use two primary antibodies generated in the same species (e.g. rabbit) for immunolabelling on the same section, a Fab fragment method was used (Eich et al., 2017; Dembla et al., 2018, 2020): Fab fragments raised against the species (e.g. anti-rabbit or anti-mouse) in which the primary antibody was generated were used for blocking of unblocked Fc regions. Fab fragments were applied on the sections at a dilution of 1:50 in PBS for 3-4h at room temperature (Dembla et al., 2018). After washing with PBS to remove unbound antibody, the second primary antibody was incubated overnight (4°C). Binding of this antibody was detected the next day with a second secondary antibody that was conjugated to a different fluorophore. Anti-mouse Fab fragments were applied in the double immunolabelling with the mouse monoclonal antibodies against Na^+K^+-ATPase (H3) and Caspr1 (5F9), Fig. S8. Anti-rabbit Fab fragments were used in the double immunolabelling of the rabbit polyclonals PMCA1 and PMCA2 with PSD95, Fig. 9 and Fig.

S10. Possible cross-talks of antibodies were ruled out by performing the experiment omitting one of the two primary antibodies.

Confocal microscopy and quantitative analyses of immunosignals

Confocal microscopy of immunolabelled sections was performed largely as previously described (Wahl et al., 2016; Eich et al., 2017; Dembla et al., 2018): For confocal microscopy, an A1R confocal microscope (Nikon) equipped with the NIS Elements software (NIS Elements AR 3.2, 64 bit) was used. Images were acquired with a 60X/1.40 N.A. oil objective using the 488 nm, 561 nm and 647 nm laser excitation lines. For quantitative analyses, confocal images of experimental and control retinas were acquired under identical conditions by using the ''re-use'' settings option of the NIS elements software every time to keep the same acquisition conditions for CFA-injected and MOG/CFA-injected samples, as previously described (Wahl et al., 2016; Eich et al., 2017; Dembla et al., 2018). Quantitative analyses were performed in a blinded manner with the experimenter not knowing the identity of the samples. Fluorescence intensity of the immunolabelled structures in the outer plexiform layer (OPL) was measured as integrated density with NIH ImageJ (Schneider et al., 2012; Schindelin et al., 2012). The region of interest (ROI) was determined by the RIBEYE / PSD95 immunosignals that served as reference to define the location of photoreceptor synapses in the OPL (Schmitz et al., 2000). Respective rectangular ROIs were placed directly bounding the RIBEYE/ PSD95 immunosignals using the ROI manager of NIH ImageJ. Identical ROIs were used for retinal sections from CFA- and MOG/CFA-injected mice. For manually counting the number of immunolabelled puncta, the multipoint tool of NIH ImageJ was used. The number of puncta was related to the actual length of the scan areas that was determined using the measurement option of NIS Elements AR 3.2, 64-bit. The average number of immunolabelled puncta was extrapolated for 100 μm length of OPL. For fluorescence intensities, averages of the values were calculated and plotted as relative values (in %) normalized to CFA values. Box-and-whiskers plots were generated with Origin Pro 2018 software. A normal distribution of the data was tested by the Shapiro-Wilk normality test. When data were normally distributed, statistical significance was determined with 2-tailed unpaired Student's t-test; non-normally distributed data were analyzed with Mann-Whitney U-test. Differences were considered to be statistically different with $p<0.05$. Statistical analyses were performed with Origin Pro 2018 software. The line scans for the immunosignals of Cav1.4 (16D9) and PSD95 in Fig. S3 were made using the Plot Profile option in NIH ImageJ and Microsoft Excel.

Super-Resolution Structured-Illumination-Microscopy (SR-SIM) and quantitative analyses of immunosignals

An ELYRA PS1 setup (Carl Zeiss Microscopy GmbH) was used for SR-SIM. Images were acquired with a 63X/1.4 NA oil (DIC) objective using the 561 nm laser line and collected through an Andor iXon EM-CCD camera (Wahl et al., 2013, 2016; Dembla et al., 2014; Dembla et al., 2020). Data acquisition was performed in a blinded manner with the experimenter not knowing the identity of the samples. For 3D SR-SIM (Schermelleh et al., 2010), 1.5 μm-thin immunolabelled resin sections were used and processed (Dembla et al., 2020). Z-stack images were acquired with an interval of 125nm between the individual z-planes using the ZEN 2010 software (black edition). The entire thickness of the retinal section was scanned, and images were then processed for 3D SR-SIM. Sections were oversampled to avoid signal loss during 3D reconstruction. Z-stack images of a single cropped Cav1.4 punctum were iteratively scanned to ensure the complete

coverage of the immunosignal before proceeding to create the 3D view. Maximum 2D projection images were generated from the 3D images of single, cropped Cav1.4 puncta for further analysis. The determination of the contour length of the presynaptic Cav1.4 clusters obtained from the maximum 2D projections of the 3D-images is exemplified in Fig. 4A. The contour length (in μm) was determined with the open polynomial line option tool of the ZEN 2012 software. Average values were calculated and plotted in Microsoft Excel. Box-and-whiskers plots were generated with Origin Pro 2018 software. Statistical analyses of the SR-SIM data were performed as described above for the quantitative analyses of confocal images.

Preparation of mouse retinal slices for Fura2 recordings

Retinal slices for Fura2-recordings were prepared with a Werblin-type tissue slicer (Wahl et al, 2016) from CFA- or MOG/CFA-injected mice obtained 7-, 8- or 9 days after injection, as indicated. After having removed pigment epithelium and vitreous body, the retina was cut at four opposing sides and was flat-mounted onto a nitrocellulose membrane (Millipore, #HABG01300) covered with a drop of the LCS buffer (with the ganglion cell layer facing the membrane). The membrane-attached retina was transferred onto a silica sieve funnel attached to a 20 mL syringe. Manual suctioning of the filter-attached retina placed at the funnel was performed for ≈20 times to promote adherence of the retina to the membrane. Afterwards, the membrane (with the attached retina) was fixed on a glass slide (retina on top) with vaseline and rewetted with a drop of LCS. The slide was transferred to the cutting stage of a Werblin-type tissue slicer to cut 200 to 300 μm thick slices. For attachment of the retinal slices, parallel streaks of vaseline were made on 25 mm-diameter cover slips. The gaps between the vaseline streaks were filled with 200-300 μL of LCS buffer. Finally, the slices were picked, rotated by 90^0 and fixed between the vaseline streaks so that all cross-sectioned retinal layers were visible. The slices were kept for about 10 min, prior to use in a humidified acrylic glass chamber aerated with 5% CO_2/ 95% O_2 at room temperature.

Loading of retinal slices with Fura2-AM and ratiometric Ca^{2+}-measurements

Fura2-recording was performed largely as previously described (Katiyar et al., 2015): For loading of the slices with Fura2, resting solution (RS) was used containing 10 μM membrane-permeable Fura2-AM (diluted from a 1 mM stock in DMSO). For better dispersion of Fura2-AM, pluronic acid (Pluronic F-127; Invitrogen, Molecular Probes, P3000MP; Yates et al., 1992) was added (0.2% final concentration, made from a 20% w/v solution in DMSO). The retinal slices were then incubated with 50 to 100 μl Fura2-AM solution in a humidified acrylic glass chamber aerated with 5% CO_2/95% O_2 for 45 to 60 min at room temperature.

The coverslip with the attached Fura2-loaded retinal slice was placed in a self-made circular open bottom chamber in a volume of 1.5 mL RS. The entire setup was mounted onto the stage of the Nikon Eclipse FN1 microscope, equipped with a high-resolution 10x water objective (N.A. 1.2) and an additional 2x magnifying lens in front of the camera. Responses were recorded from the outer plexiform layer (OPL) containing the photoreceptor synapses (as the region of interest, ROI) using the ROI manager of the NIS elements software**.** The OPL was readily identified by epifluorescence (380 nm excitation), phase contrast and F340 / F380 epifluorescence signals and the ROI was made according to that. After incubation with Fura2-AM, retinal slices were washed twice with resting solution (RS). Next, fluorescence recording was started with the slices being incubated in 1.5 mL RS to monitor the resting Fura2 signals in the photoreceptor

synapses. Ratiometric images were acquired by means of a Sutter DG4 light source for fast wavelength switching, equipped with the respective filter systems (Ex 340/12 // 380/12; dichroic 400LP; Em 510/80) for Fura2 Ca^{2+}-imaging. Image acquisition was controlled with the NIS Elements AR 4.30.02 software. Images were acquired every 1 second. All conditions were kept identical for the sets of retinal slices. The F340 nm / F380 nm ratio recorded under these conditions were considered as read out for the intracellular Ca^{2+}-concentrations at the resting state (i.e. without depolarization stimulus). For inducing depolarization-evoked responses, 50 mM K^+-containing solution was added to a same volume of RS to obtain a depolarization solution that contained ~25 mM K^+ (26.5 mM K^+). The high K^+ depolarization-induced Ca^{2+}-responses in the OPL were recorded at an image acquisition frequency of 1Hz, as described above. 8-10 retinal slices were typically recorded from an individual mouse. Data acquisition was performed in a blinded manner with the experimenter not knowing the identity of the samples.

Quantitative analyses of Fura2 Ca^{2+} - signals at resting and depolarization conditions

Ratiometric Fura2 values recorded from the OPL during resting conditions and depolarization were exported as Excel files. Mean values and standard errors of the mean of Fura2 signals under resting conditions (i.e. incubation with RS only) were calculated and plotted with Excel. Baseline values were tested for normal distribution using Shapiro-Wilk test performed with Origin software (2018b). Accordingly, two-tailed unpaired Student's t-test (for normally distributed data) or Mann-Whitney U-test (for non-normally distributed data) was performed for testing statistical significance. Differences were considered to be statistically different with $p<0.05$. Data distributions were illustrated by box-and-whiskers plots with median (50%) and mean values, boxes extending from the 25^{th} to the 75^{th} percentile and whiskers extending down to 1.5 times of the interquartile range (IQR) on both sides. The calculations and analyses of Fura2 signals were done for each of the indicated days after peptide injection separately (i.e. day 7, day 8 or day 9 after injection).

For the analyses of depolarization-evoked Fura2 signals, all individual depolarization-evoked responses/traces were normalized to the values obtained at the time point at which the depolarization solution was added (i.e. at the 60 seconds time point). Normalized mean curves were plotted in Microsoft Excel. Data were imported into the Igor Pro 6.22A software to determine the peak amplitudes. Subsequent curve fitting of the traces with Igor Pro revealed that the traces follow a single exponential fit. Averages of the individual extracted amplitudes from all slices of the CFA- and MOG/CFA-injected mice from days 7 to 9 after injection were calculated and plotted in Microsoft Excel. Statistical analyses of data were performed as described above.

In order to semi-quantitatively relate the measured mean ratiometric Fura2 values to calcium concentrations, calcium calibration was done on retinal slices that were loaded with Fura2 AM (as described above). The slices were first equilibrated to 0 nM Ca^{2+} in the presence of 0.4% Pluronic acid and 50 µM Ionomycin (Sigma, I3909). Subsequently, by using commercial Ca^{2+} buffer solutions with defined calcium concentrations (Fisher Scientific, F6774) experimental K_D of Fura2 was determined and mean Fura2 F340 / F380 ratiometric values (basal resting values and peak amplitudes of the average traces determined by Igor Pro curve-fitting) were transformed into Ca^{2+} concentrations by using the Grynkiewicz equation (Grynkiewicz et al., 1985).

Incubation of retinal slices with ouabain before subsequent Fura2 recording

For the ouabain experiments, mouse retinal slices were first loaded with Fura2 AM for 45 min as described above. The slices were subsequently washed 2-3 times with RS. Next, 3-4 coverslips were incubated with 50-100 µL of 500 µM ouabain in RS for 15-20 min before the beginning of the Fura2 recording. The concentration of ouabain applied in our study is similar to concentrations that have been also used in other studies on murine tissues (e.g. Winkler, 1983; Vale-Gonzalez et al. 2007; Yuan et al., 2014; Akimova et al., 2015). During incubation of the experimental slices with ouabain, control slices were incubated with RS. All other procedures were kept identical. Fura2 recording was performed as described above at an acquisition frequency of 1 Hz. 12-16 slices were recorded from each mouse. Statistical analyses were performed with Origin2019b.

Fura2 control experiment in retinal slices with Co^{2+}

In order to probe whether the high K^+ depolarization-evoked Ca^{2+} Fura2 responses originate from Ca^{2+} entry via voltage-gated calcium channels (Cav-channels) control experiments were done by pre-treating slices with 2.5 mM Co^{2+} that blocks Ca^{2+} entry through Cav-channels (Evans et al., 1978; Schwartz, 1986; Grabner et al., 2015). Fura2 imaging of retinal slices were started in 1.5 ml of RS to which 2.5 mM Co^{2+} had been added (for a duration of 30 sec) followed by depolarization with 1.5 ml of depolarization solution that also contained 2.5 mM Co^{2+}. The solutions for the untreated control slices had no Co^{2+}. Recording was performed with NIS Elements software, as described above. After recording, the average Fura2 (F340 / F380) traces of the cobalt treated and untreated slices were normalized to a common baseline set at the 30^{th} sec value and the depolarization evoked Ca^{2+} influx in both the cases were plotted and compared in MS-Excel. Analyses for statistical significance were done with Origin Pro 2020.

Western blot analyses

Retinas from CFA and MOG/CFA mice were obtained within 5 min post-mortem, transferred into a tube with 50 µl of ice-cold PBS and sonicated using two pulses of 1 second at 10% power and 8 x 10% cycle (Bandelin Sonoplus). 200 µL of 37^0C Laemmli buffer was added to the cell lysate and incubated at 37^0C for 30 min for the Western blots with anti-PMCA2/3, anti-Na^+K^+ATPase α-subunit and Cav1.4 N-term. For the Western blots with anti-RIM2 and anti-Cavβ2, the protein lysates were heated in Laemmli sample buffer at 95^0C for 10 min. 40 µg of retinal lysate (quantified by the Amido Black method as described by Dieckmann-Schuppert and Schnittler, 1997) was loaded on a 7 % SDS PAGE gel and run at 80 V for 45 min, followed by 100 V for 4 hr on ice. Western blot transfer was done in the cold room at 40 V for 10 hr. The next day, the blots were blocked in 5% skim milk / 0.1% Tween20 in PBS (blocking buffer) before the incubation with the primary antibody solution (in blocking buffer, overnight, at 4^oC). The following day, after several washes with PBS to remove unbound primary antibody, lanes were incubated with the respective POX-conjugated anti-mouse and anti-rabbit secondary antibodies for 1-2 hr at a dilution of 1:3,000 and developed with enhanced chemiluminescence and a BioRad Geldoc system.

Quantification of Western blot bands were done using the "Analyze Gels" option of NIH ImageJ. The band intensities for the various proteins normalized with the respective actin loading controls of each MOG/CFA and CFA pair were plotted in Microsoft Excel. The band intensities for each pair of mice was also plotted with the CFA values set to 100% in MS Excel to better compare also changes between the individual Western blots. Box plots of the data and statistical analyses of the data (test of normality followed by the significance

test depending on normality) were performed in Origin 2019b. Unpaired t-test for equal variances was performed in all the cases as the data were normally distributed and the MOG/ CFA and CFA groups demonstrated equal variances.

References

Akimova, O.A., Tverskoi, A.M., Smolyaninova, L.V., Mongin, A.A., Lopina, O.D., La, J., Dulin, N.O., and Orlov, S.N. (2015). Critical role of α1-Na^+, K^+-ATPase subunit in insensitivity of rodent cells to cytotoxic action of ouabain. Apoptosis 20, 1200-1210.

Dembla, M., Wahl, S., Katiyar, R., and Schmitz, F. (2014). ArfGAP3 is a component of the photoreceptor synaptic ribbon complex and forms a NAD(H)-regulated, redox-sensitive complex with RIBEYE that is important for endocytosis. J. Neurosci. 34, 5245-5260.

Dembla, M., Kesharwani, A., Natarajan, S., Fecher-Trost, C., Fairless, R., Williams, S.K., Flockerzi, V., Diem, R., Schwarz, K., and Schmitz, F. (2018). Early auto-immune targeting of photoreceptor ribbon synapses in mouse models of multiple sclerosis. EMBO Mol. Med. 10(11), e8926.

Dembla, E., Dembla, M., Maxeiner, S., and Schmitz, F. (2020). Synaptic ribbons foster active zone stability and illumination-dependent active zone enrichment of RIM2 and Cav1.4 in photoreceptor synapses. Sci. Rep. 10, 5957; https://doi.org/10.1038/s41598-020-62734-0.

Dieckmann-Schuppert, A., and Schnittler, H.-J. (1997). A simple assay for quantification of protein in tissue sections, cell cultures, and cell homogenates, and of protein immobilized on solid surfaces. Cell Tiss. Res. 288, 119-126.

Eich, M.L., Dembla, E., Wahl, S., Schwarz, K., and Schmitz, F. (2017). The calcineurin-binding, activity-dependent splice variant dynamin1xb is highly enriched in synapses in various regions of the central nervous system. Front. Mol. Neurosci. 10, 230; https://doi.org/10.3389/fnmol.2017.00230.

Evans, J.A., Hood, D.C., and Holtzman E. (1978). Differential effects of cobalt ions on rod and cone synaptic activity in the isolated frog retina. Vision Res. 18, 145-151.

Grabner, C.P., Gandini, M.A., Rehak, R., Le, Y., Zamponi, G.W., and Schmitz, F. (2015). RIM1/2-mediated facilitation of Cav1.4 channel opening is required for Ca^{2+}-stimulated release in mouse photoreceptors. J. Neurosci. 35, 13133-13147.

Grynkiewicz, G., Poenie, M., and Tsien, R.Y. (1985). A new generation of Ca^{2+} indicators with greatly improved fluorescence properties. J Biol Chem. 260, 3440-3450.

Hegedüs, L., Padanyi, R., Molnar, J., Paszty, K., Varga, K., Kenessey, I., Sarkozy, E., Wolf, M., Grusch, M., Hegyi, Z., Homolya, L., Aigner, C., Garay, T., Hegedüs, B., Timar, J., Kallay, E., and Enyedi, A. (2017). Histone deacetylase inhibitor treatment increases the expression of the plasma membrane Ca^{2+} pump PMCA4b and inhibits the migration of melanoma cells independent of ERK. Front. Oncol. 7, 95.

Irie, M., Hata, Y., Takeushi, M., Ichtchenko, K., Toyoda, A., Hirao, K., Takai, Y., Rosahl, T.W., and Südhof, T.C. (1997). Binding of neuroligins to PSD-95. Science 277, 1511-1515.

Jeong, J., VanHouten, J.N., Dann, P., Kim, W., Sullivan, C., Yu, H., Liotta, L., Espina, V., Stern, D.F., Friedman, P.A., and Wysolmerski, J.J. (2016). PMCA2 regulates HER2 protein kinase localization and signalling and promotes HER2-mediated breast cancer. Proc. Natl. Acad. Sci. USA 112, E3141-E3149.

Katiyar, R., Weissgerber, P., Roth, E., Dörr, J., Sothilingam, V., Garcia Garrido, M., Beck, S.C., Seeliger, M., Beck, A., Schmitz, F., and Flockerzi, V. (2015). Influence of the β2-subunit of L-type voltage-gated Cav channels on the structural and functional development of photoreceptor ribbon synapses. Invest. Ophthalmol. Vis. Sci. 56, 2312-2324.

Križaj, D., Demarco, S.J., Johnson, J., Strehler, E.E., and Copenhagen, D.R. (2002). Cell-specific expression of plasma membrane calcium ATPase isoforms in retinal neurons. J. Comp. Neurol. 451, 1-21.

Link, S., Meissner, M., Held, B., Beck, A., Weissgerber, P., Freichel, M., and Flockerzi, V. (2009). J. Biol. Chem 284, 30129-30137.

Michalakis, S., Shaltiel, L., Sothilingam, V., Koch, S., Schludi, V., Krause, S., Zeitz, C., Audo, I., Lancelot, M.E., Hamel, C., Meunier, I., Preising, M.N., Friedburg, C., Lorenz, B., Zabouri, N., Haverkamp, S., Garcia Garrido, M., Tanimoto, N., Seeliger, M.W., Biel, M., and Wahl-Schott, C.A. (2014). Mosaic synaptopathy and functional defects in Cav1.4 heterozygous mice and human carriers of CSNB2. Hum. Mol. Genet. 23, 1538-1550.

Meissner, M., Weissgerber, P., Londono, J.E., Prenen, J., Link, S., Ruppenthal, S., Molkentin, J.D., Lipp, P., Nilius, B., Freichel, M., and Flockerzi, V. (2011). Moderate calcium channel dysfunction in adult mice with inducible cardiomyocyte-specific excision of the cacnb2 gene. J. Biol. Chem. 286, 15875-15882.

Okawa, H., Yu, W.Q., Matti, U., Schwarz, K., Odermatt, B., Zhong, H., Tsukamoto, Y., Lagnado, L., Rieke, F., Schmitz, F., and Wong, R.O. (2019). Dynamic assembly of ribbon synapses and circuit maintenance in a vertebrate sensory system. Nat. Commun. 10, 2167.

Schermelleh, L., Heintzmann, R., and Leonhardt, H. (2010). A guide to super-resolution fluorescence microscopy. J. Cell Biol. 190, 165-175.

Schindelin, C.A., Arganda-Carreras, I., Frise, E., Kaynig, V., Longair, M., Pietzsch, T., Preibisch, S., Rueden, C., Saalfeld, S., Schmid, B., Tinevez, J.Y., White, D.J., Hartenstein, V., Eliceiri, K., Tomancak, P., and Cardona, A. (2012). Fiji: an open source platform for biological-image analysis. Nature Meth. 9, 676-682.

Schmidt, N., Kollewe, A., Constantin, C.E., Henrich, S., Ritzau-Jost, A., Bildl, W., Saalbach, A., Hallermann, S., Kulik, A., Fakler, B., and Schulte, U. (2017). Neuroplastin and basigin are essential auxiliary subunits of plasma membrane Ca^{2+}-ATPases and key regulators of Ca^{2+} clearance. Neuron 96, 827-838.

Schmitz, F., Königstorfer, A., and Südhof, T.C. (2000). RIBEYE, a component of synaptic ribbons: a protein's journey through evolution provides insight into synaptic ribbon function. Neuron 28, 857-872.

Schneider, C.A., Rasband, W.S., and Eliceiri, K.W. (2012). NIH image to ImageJ: 25 years of image analysis. Nature Meth. 9, 671-675.

Schwartz, E.A. (1986). Synaptic transmission in amphibian retinae during conditions unfavourable for calcium entry into presynaptic terminals. J. Physiol. 376, 411-428.

Shi, M., Cao, L., Cao, X., Zhu, M., Zhang, X., Wu, Z., Xiong, S., Xie, Z., Yang, Y., Chen, J., Wong, P.T.H., and Bian, J.S. (2019). DR-region of Na^+/K^+ ATPase is a target to treat excitotoxicity and strok. Cell Death Dis. 10, 6. https://doi.org/10.1038/s41419-018-1230-5.

Specht, D., Wu, S.B., Turner, P., Dearden, P., Koentgen, F., Wolfrum, U., Maw, M., Brandstätter, J.H., and tom Dieck, S. (2009). Effects of presynaptic mutations on a postsynaptic Cacna1s calcium channel localized with mGluR6 at mouse photoreceptor ribbon synapses. Invest. Ophthalmol. Vis. Sci. 50, 505-515.

Vale-Gonzalez, C., Pazos, M.J., Alfonso, A., Vieytes, M.R., and Botana, L.M. (2007). Study of the neuronal effects of ouabain and palytoxin and their binding to Na^+, K^+-ATPases using an optical biosensor. Toxicon 50, 541-552.

Wahl, S., Katiyar, R., and Schmitz, F. (2013). A local, periactive zone endocytic machinery of photoreceptor synapses in close vicinity to synaptic ribbons. J. Neurosci. 33, 10278-10300.

Wahl, S., Magupalli, V.G., Dembla, M., Katiyar, R., Schwarz, K., Köblitz, L., Alpadi, K., Krause, E., Rettig, J., Sung, C.H., Goldberg, A.F.X., and Schmitz, F. (2016). The disease protein Tulp1 is essential for periactive zone endocytosis in photoreceptor ribbon synapses. J. Neurosci. 36, 2473-2493.

Winkler, B.S. (1983). Relative inhibitory effects of ATP depletion, ouabain and calcium on retinal photoreceptors. Exp. Eye Res. 36, 581-594.

Yates, S.L., Fluhler, E.N., and Lippiello, P.M. (1992). Advances in the use of the fluorescent probe fura-2 for the estimation of intrasynaptosomal calcium. J. Neurosci. Res. 32, 255-260.

Yuan, Y., Shi, F., Yin, Y., Tong, M., Lang, H., Polley, D.B., Liberman, M.C., and Edge, A.S.B. (2014). Ouabain-induced cochlear nerve degeneration: synaptic loss and plasticity in a mouse model of auditory neuropathy. J. Assoc. Res. Otolaryngol. 15, 31-43.